Laser Photofragment Spectroscopy of Diatomic Molecular Ions

by

Timothy Gibbon, B.Sc.

Thesis submitted to the University of Nottingham for the degree of
Doctor of Philosophy, October 1998

Abstract

High resolution (< 0.005 cm^{-1}) electronic spectra of the diatomic molecular ions $^{70}GeH^+$ and $^{74}GeH^+$ have been recorded using a fast ion beam irradiated by a cw tunable dye laser. Over 150 transitions between the ground $X^1\Sigma^+$ state and near-threshold levels of electronic states correlating to the lowest dissociation asymptotes $Ge^+(^2P_{\frac{3}{2}}) + H(^2S)$ and $Ge^+(^2P_{\frac{1}{2}}) + H(^2S)$ were observed in the range 16500 cm^{-1} to 18500 cm^{-1}.

The majority of the lines arise from a $^1\Pi$-$^1\Sigma$ transition, where the predissociated excited state levels lie between the fine structure dissociation limits (Feshbach Resonances). The lifetimes of the rovibrational levels are found to increase, then decrease, with increasing rotational quantum number. Evidence for triplet (multichannel) mixing is revealed through the observation of additional lines and proton nuclear hyperfine splittings.

Experimental results are compared with predictions of the vibrational and rotational energy levels obtained from a numerical solution of the Schrödinger equation. Least squares fitting yields molecular constants for the $^1\Sigma$ and the $^1\Pi$ states.

A new apparatus used to create jet-cold molecular ions in a fast ion beam is detailed. Preliminary results have been obtained for the $b^4\Sigma_g^- \leftarrow a^4\Pi_u$ transition of O_2^+ which allow a rotational temperature for the source to be calculated.

Contents

Acknowledgements

Firstly, I'd like to thank my supervisor, Prof. Peter Sarre, for his boundless enthusiam, assistance and eternal optimism.

Thanks to my colleagues for their time and assistance and for making Nottingham the place to be, Dr Janet Miles, Dr Tom Kerr, Dr Andrew Batey, Mr Mark Hurst, Mr Phil Couch, Dr Tim Kendall and Barbara Duigan.

In particular, a big thankyou to Dr Rob Hibbins, Dr June McCombie and Paul Boichat for all their help and support and also for reading early drafts of this document. I also wish to thank Dr Iain McNab, in particular for stimulating my interest in laser photofragment spectroscopy as an undergraduate.

Thankyou to my laboratory co-workers, Dr Alfred Geers, Dr Yang Chen and Dr Jia-xiang Han for their help in recording spectra, patience and making A44 a nice place to 'live'. I would also like to thank the invaluable workshop staff and in particular Ralph Parsons, Dave Lichfield and Neil Barnes.

I wish to thank all of my (extended) family, especially Mum, Dad, Chris and Angela for all that they have done for me.

Finally I would like to thank my friends, who have kept me sane, brightened my life (and supplied beer) for the last n years: Martin Manning, Leonard Beanchi, Mayney, Lou, Jules, Rich and Doreen Mayne.

Chapter 1 Introduction

1.1 Molecular ions

Gas phase molecular ions are of considerable interest and importance in many areas of chemistry and physics. They have been identified in many diverse areas ranging from the interstellar medium, comets, the earth's atmosphere, through to flames and plasmas. In some instances, studies of molecular ions in extra-terrestrial sources have pre-empted laboratory based experiments or calculations and vice-versa. Through an understanding of diatomic molecular ions (their geometries and inter-atomic potentials) an insight can be gained into atom-ion interactions, yielding a greater understanding of the important processes occurring in these media [1].

Laboratory-based spectroscopic studies of molecular ions are intrinsically more difficult than for the corresponding neutral molecules due to short lifetimes which result from ion-molecule reactions. Additional losses result from ions combining with electrons or diffusing to the walls of a container. It is hence difficult to form and maintain high densities of molecular ions for study within the time scales of most standard spectroscopic techniques. The use of laser-based experiments has meant the availability of high photon densities to compensate for the low ion densities, allowing spectra for a wide range of molecular ions to be recorded.

Several reviews of the spectroscopy of molecular ions exist, including Herzberg's review of early work [2], Saykally and Woods' [3] account of high resolution techniques, Moseley's paper describing Ion Photofragment spectroscopy [4] and Maier's brief review of some current techniques (with respect to electronic transitions) [5].

The fundamental aim of the studies outlined in this thesis is to probe diatomic molecular ions, using a laser photofragment spectroscopy technique to increase the knowledge of the structure and dynamics in such systems.

1.1.1 Emission Spectroscopy

Early laboratory spectra of molecular ions were generally recorded in emission, where ions are produced in highly excited states (for example by an electric discharge). Radiative relaxation from this state occurs and the emitted radiation is dispersed and collected to obtain spectra.

One high resolution spectrum recorded using this technique is that of the $B^2\Sigma^+ - X^2\Sigma$ transition of $HeNe^+$ [6]. Dabrowski and Herzberg mixed high purity He and Ne in the ratio 10:1 inside a hollow cathode discharge, dispersed the resulting emission and recorded the spectrum using photographic plates.

Similarly, a rotationally resolved emission spectrum for the $^1\Pi$-$^1\Sigma^+$ transition of CH^+ was recorded at high resolution by Carrington and Ramsay [7] using a hollow cathode discharge lamp. The error in recording the positions of individual lines is considered to be ≈ 0.003 cm^{-1}.

A recent example of a dispersed emission spectrum is the study of $NeRg_2^+$ (Rg=Ar,Kr and Xe), $ArRg_2^+$ (Rg=Kr,Xe) and $KrXe_2^+$ recorded by Tsuji et al. [8] using a rare gas flowing afterglow tube. The apparatus [9] involves the passage of a rare gas through a microwave discharge into a stainless steel reaction cell. A large (7000 ℓs^{-1}) vacuum pump draws the gas continuously away from the discharge region. The rare gas then passes over a gas inlet, where a relatively small amount of the sample gas flows into the chamber. Charge exchange between the rare gas ions and the neutral precursor gas occurs and emission spectra are recorded using a monochromator and photomultiplier (slightly downstream of the sample inlet). One problem of using such an apparatus is that the carrier species for any spectrum is unknown, and that emission bands for several species overlap with both each other and with the lines due to transitions in the rare gas atoms.

One commonly used method for recording either absorption or emission spectra is that of Laser Induced Fluorescence (LIF) where an upper electronic state is populated by driving transitions from a lower electronic state using a tunable laser. Two methods are commonly used to study the spectrum of the molecule:

- The frequency of the laser is varied and the total fluorescence measured as a function of laser frequency. The structure of the upper electronic state is probed by observing absorptions in the total fluorescence (also called a Laser Excitation Spectrum).
- The laser is fixed upon a single transition and the resultant fluorescence dispersed using a monochromator, thus probing the level structure of the lower electronic state from the emission lines.

LIF studies are commonly used in conjunction with a jet cooled source which reduces the population of high lying vibrational and rotational states and hence the number of transitions' leading to spectral simplification. An example of a molecular ion recorded using LIF with jet cooling is the molecular complex $C_6F_6^+$.X (where X is He, Ne, N_2 or Ar) [10].

A novel technique used to study LIF spectra of HBr^+ was that of Xie and Zare [11]. The $A^2\Sigma^+$-$X^2\Pi$ transition of HBr^+ was recorded using 2+1 resonance-enhanced multi-photon ionisation (REMPI) to prepare HBr^+ in the X state from the HBr precursor. This was followed by LIF, using a second (probe) laser to populate levels of the upper $A^2\Sigma$ state. It proved possible to select the lower fine structure level of HBr^+ by selecting different HBr Rydberg states in the REMPI process.

Laser induced fluorescence has been used in conjunction with fast ion beams to record high resolution spectra of molecular ions. Recently, a spectrum of the $B^4\Sigma_u^-$ - $X^4\Sigma_g^-$ transition of C_2^+ was recorded [12]. Transitions to the upper state were Doppler tuned into resonance (by varying the drift region potential) with the 501.7 nm line from an argon ion laser. The advantage of using fast ion beams in conjunction with laser induced fluorescence is that the line widths are considerably reduced in comparison to those found using standard Doppler-limited techniques. Similarly, this very sensitive technique has been used to record hyperfine structure in the (1,2) band of the $B^2\Sigma_u^+ - X^2\Sigma_g^+$ transition in $^{14}N_2^+$ and $^{15}N_2^+$ [13]. Fast ion beam laser induced fluorescence has been applied recently to the $B^2\Sigma^+ - X^2\Sigma^+$ transition of SiO^+ [14], where ions were produced by ionisation of heated SiO powder, extracted from the source and Doppler tuned into resonance with transitions from a Ti:sapphire ring dye laser.

Further techniques involving the LIF of fast ion beams use the principle of the in-flight Lamb-dip method [15]. An ion beam and laser beam are made collinear, but the laser frequency and ion beam velocity (acceleration voltage) are selected so that any transitions are off resonance. The ion beam then passes through a flight region where voltages are applied to the ion beam to tune a transition into resonance with the laser. Due to the velocity distribution in the ion beam, only ions with a selected velocity will be in resonance and a 'hole' will be 'burned' into the beam. Using radio-frequency (rf) magnetic dipole transitions, the 'hole' is transferred from one lower state level to another level, *without altering the translational velocity.* The ions from which pumping occurred will fluoresce from the excited state, but only a few will return to their original state. In the second (downstream probe) flight region, the same process occurs and the spontaneous emission is detected by a photomultiplier. If the voltages in the two regions are the same, the laser beam will interact with the same velocity group of ions in both and a decrease in the detected fluorescence will be found. This 'Lamb-dip' will been seen when the pump region is in resonance with an optical transition. In practice, the frequency of the rf voltage is fixed while the voltage applied to the pump region is scanned. This technique has been used to study the (0,1) band of the $B^2\Sigma_u^+$ - $X^2\Sigma_g^+$ transition for N_2^+ at extremely high resolution.

Emission spectra can also be recorded using Stimulated Emission Pumping (SEP) [16]. A fixed frequency laser induces a transition to an upper electronic state (pump), whereupon the frequency of a second laser is scanned in order to stimulate emission from that state back to the ground electronic state (dump). Resonances are detected by monitoring the decrease in spontaneous emission. This technique has been applied to the $A^2\Pi_{u,\frac{3}{2}} - X^2\Pi_{g,\frac{3}{2}}$ transition in the diacetylene ion $H_2C_2^+$ [17].

1.1.2 Infrared and Microwave studies

Oka and co-workers were the first group to report a direct infrared absorption spectrum of a molecular ion. They passed coherent infrared radiation through a multiple reflection, liquid nitrogen cooled, discharge cell and recorded a vibration-rotation spectrum of H_3^+; the simplest triatomic molecular ion. The laser radiation source was constructed from the output of a dye and argon laser mixed in a $LiNbO_3$ crystal. The ratio of ions to neutral species in such a cell is approximately $1{:}10^6$, and so an inherent disadvantage of such a technique is that the molecular ion absorption spectra can become obscured beneath (even weak) neutral species absorptions. Three modulation techniques have been developed to overcome these disadvantages and to enable the direct infrared absorption spectra of molecular ions to be recorded:

- **Velocity modulation:** Charged species in a gas mixture consisting of neutrals and ions experience a Coulombic force as a result of the potential gradient of the discharge. The ions therefore have a net velocity in one direction superimposed onto their random thermal motion and will 'observe' the laser at a Doppler shifted frequency. If the polarity is reversed, the ions will travel in the opposite direction, and the Doppler shift will be reversed. By alternating the polarity, absorptions of the charged species are seen to be in phase. Lock-in detection methods can then be used to detect the absorptions due only to ions. This technique was developed by Saykally [18] and is particularly suitable for use with semiconductor diode lasers: absorption spectra for the fundamental band of SiH^+ [19], the (2,0) band of the $A^2\Pi_u - X^2\Sigma_g^+$ transition of N_2^+ [20, 21] and rotationally quasibound levels in v = 0,1 and 2 of the $^1\Sigma^+$ state of HeH^+ [22] have recently been recorded using velocity modulated spectroscopy.

- **Discharge modulation:** The precursor gas is contained inside a large conducting cathode and a discharge current is rapidly switched on and off. As the cathode allows current of one polarity to pass through, the current flows in one direction only. Ions are therefore only present during one phase of the alternating current. The method of lock-in detection is again used to detect absorptions. This technique has been applied to the ν_3 band of the astrophysically important HCO^+ molecule

[23]. A recent variation on discharge modulation has seen a technique in which an electron ionisation source was modulated [24]. The modulated electrons cross an expansion slit, where supersonic gas is ionised. This experiment allowed the first observation of the ν_3 (1←0) transition of N_4^+ in the gas phase and shows it to be a linear molecule.

- **Magnetic modulation:** In this case, high frequency longitudinal AC field in conjunction with a DC offset magnetic field is applied to a hollow cathode discharge tube using a solenoid. A strong magnetic field gives the ions a helical trajectory reducing collisions with the wall and hence ion concentrations are increased. Such apparatus has been used to study the ν_2 band of HCO^+ [25]

Microwave spectroscopy generally involves transitions between rotational states in the ground vibrational state. It is an extremely high resolution technique which allows a very precise determination of many terms in the Hamiltonian. Laboratory studies of microwave spectra for molecular ions were first performed in a glow discharge spectrometer on CO^+ by Dixon and Woods [26].

Microwave spectroscopy has also recently been used in conjunction with Fourier Transform techniques to study the rotational spectra of a number of polyatomic ions using a Pulsed Discharge Nozzle (PDN) coupled with a Fourier-transform microwave spectrometer. Shortly after leaving the nozzle the ions are subject to a Lorentz force due to a static magnetic field passing through a coil. This focusses ions into a region in the centre of the microwave cavity, where spectra can be recorded. Spectra of $HOCO^+$, $HOCS^+$, D_3^+-Ar and D_2H^+-Ar have been recorded in this manner [27].

1.1.3 Laser Magnetic Resonance

This technique employs a variable magnetic field to bring molecular energy levels into resonance with a fixed laser frequency. A Fabry-Perot resonator is transversely pumped by a CW CO_2 laser and an intra-cavity beamsplitter is used to select parallel or perpendicular laser polarisation (with respect to the magnetic field). A discharge occurs in the sample region of the cavity located the between pole faces of a large (typically 0 - 2 T) magnet. The intra-cavity laser power is measured as a function of the magnetic field and a small sinusoidal field is superimposed on the d.c. field so that lock-in detection can be utilised. This technique is particularly suitable for open-shell molecules, where the energy levels tune significantly when a magnetic field is applied. The first transitions to be observed using this technique were in the lowest vibrational level of the $^2\Pi_{\frac{3}{2}}$ state of HBr^+[28]. It has also been applied to the $a^1\Delta$ state of OH^+ in order to study the J = 3-2 transition in the ground vibrational state [29]. A general review of laser magnetic resonance can be found in [30].

1.1.4 Direct absorption techniques

A recent absorption study has recorded the first spectrum for TiF^+ using a sensitive high resolution absorption technique [31]. Solid phase parent TiF_4 was heated with a thermal resistor to create TiF_4 vapour in a cell. Helium gas was flowed through a central inlet, carrying the precursor gas, which was ionised using a AC glow discharge source. The oscillatory discharge allows accurate detection using the velocity modulation technique [18] which eliminates signals from neutral molecules. A ring dye laser operating in the 16,800 - 18,600 cm^{-1} region was used in conjunction with a two photodiodes to record the absorption spectrum through the cell.

Cavity ring down spectroscopy is a very sensitive technique [32], used to measure absorption spectra. It has recently [33] been combined with a molecular ion source to study the (6,0) band of the $A^2\Pi_u - X^2\Sigma_g^+$ transition of N_2^+. The technique involves a hollow cathode discharge cell consisting of two highly silvered mirrors (99.99 % reflectivity) at either end. A pulsed laser is focussed into the chamber and the ring-down time (which is the lifetime of the decay curve for residual laser power leaving the cavity) is shorter with the laser on resonance, and longer when it is off resonance. A photomultiplier is used to detect the residual laser power emanating from the cell and electronic timing gates convert this to an absorption signal. Due to the high reflectivity of the mirrors and long path length, the laser pulse passes through the chamber many times thus allowing very weak absorptions to be recorded.

1.2 Photodissociation of molecular ions

Due to the use of high power lasers to fragment ions and the possibility of almost unit detection of fragments, photodissociation is a particularly favourable technique for ion studies. Photofragment detection not only yields information about the spectroscopy of the electronic states, but also the dissociation mechanism. The process of photodissociation is entirely analogous to that of atom-ion collisional scattering and shares much of the same terminology.

To fully understand a collision between an atom and an ion in which both fragments have non-zero spin, all the different couplings between the potential curves must be considered. Direct studies of collisional processes average over such couplings, whereas ion photofragment spectroscopy techniques can prepare the molecule in one dissociative state. Measurements can be made of the kinetic energy of the fragment, (and the angular distribution of the photofragments) and lifetime of such a state.

Since the advent of high power lasers, it has proved possible to probe the

region between the 'molecular' and 'atomic' limits (the 're-coupling region') using laser photofragment spectroscopy and it thus offers significant advantages over scattering experiments, where initial reactant energies are poorly defined and control over the impact parameters is limited. The spectroscopy of molecular ions close to the equilibrium bond length is easily probed using absorption and emission techniques, and is generally thought to be well understood. The atomic limit is also well defined. Between these 'chemical' and 'physical' limits (in the 're-coupling region'), the spectroscopy is more difficult to define and generally less well developed.

Through studying molecular ions at rotational resolution, weak interactions (such as spin-orbit splittings, hyperfine interactions and lambda doubling) can be observed, giving a detailed characterization of the electronic wavefunction.

1.3 Ion Beam Techniques

The first fast ion beam experiment was performed by von Busch and Dunn [34] who crossed photons from an arc lamp with a beam of H_2^+ ions in order to measure the total cross section for the photo-production of H^+, and the population distribution of the vibrational states. Photofragment spectroscopy techniques flourished with the introduction of lasers into the field. Ozenne et al [35] pioneered a technique where an ion beam was crossed with a ruby pulsed laser in order to measure the energy releases of H^+ from H_2^+. Shortly after this study, van Asselt et al., [36] probed the kinetic energy distributions of the photofragments using a laser beam inside an argon ion laser cavity. The photofragmentation of H_2^+ was probed as a function of laser wavelength and the relative population distributions in the ground $1s\sigma_g$ state determined.

Wing et al. [37] first applied 'Doppler tuning' to fast ion beams, by coaxially irradiating a fast ion beam of HD^+ with a CO_2 laser. Scanning was achieved by varying the potential across a section of the flight region, thus varying the velocity of the ions and hence a single frequency source was able to 'scan' rovibrational transitions of the molecule. The first four vibrational levels of the ground state of HD^+ were observed, between 1,600 and 1,900 cm^{-1}, by passing the irradiated ion beam through a target gas and detecting the resulting current. As transitions between rovibrational states change the population of states, the survival time for the ions in the gas target is changed and therefore the current arriving at the detector will be dependant on the transition. The laser beam was chopped to improve the sensitivity of the technique through lock-in detection methods.

The next logical step was to investigate the absorption spectra using predissociated upper states. To obtain photofragments, laser radiation was used to drive a transition to a quasibound upper state, whereupon dissociation occurred. The fragment ion current could then be obtained as a function of the wavelength of laser radiation and an absorption spectrum of transitions between bound and quasibound electronic states recorded. This was first achieved by Moseley et al., who studied the O^+ fragments arising from the predissociation of an upper state of O_2^+ [38] using the technique of Threshold Photofragment Spectroscopy (TPFS). A fast ion beam was crossed by the output from a pulsed tunable dye laser operating between 578 and 586 nm and the relative photofragment current recorded as a function of the laser frequency. A peak in the photoproduct O^+ current was observed. This was later correctly identified as the $b^4\Sigma_g^- - a^4\Pi_u$ transition by Carrington, Roberts and Sarre [39]. Carrington and co-workers devised an experiemnt which involved accelerating O_2^+ ions into a tandem mass spectrometer to high voltages, whereupon parent and daughter species could be selected using magnetic sectors and an electron multiplier used to detect the O^+ fragment ions. Transitions of O_2^+ were 'Doppler tuned' into resonance with the 496 nm line of an argon ion laser by applying of a small subsidiary voltage to the flight region between the two magnetic sectors. This assignment was confirmed shortly afterwards when a detailed recording of the 17,060-17,300 cm^{-1} region was instigated using a fast ion beam in conjunction with a tunable dye laser [40].

These early studies formed the basis of laser photofragment spectroscopy studies as they are now known. Reviews of fast ion beam spectroscopy techniques include [4, 41, 42].

Carrington and co-workers went on to develop this technique which offered several advantages including: absolute selection of the spectral carrier, the possibility of selecting the fragment of interest, the high resolution probing of energy level structure, investigation of quasibound levels, the measurement of excess translational energy of the fragment ion and orientation of the dipole transition moment from the spatial distribution of the fragment ions. This technique has since been used in studies of CH^+ [43, 44], HeH^+ [45] and HD^+ [46, 47]

Laser photofragment spectroscopy techniques have proved particularly adept at investigating the 're-coupling region' between 'molecular' and 'atomic' limits. Several different dissociation mechanisms have been identified in laser photofragment spectra. For example, the $^1\Pi$-$^1\Sigma^+$transition of the astrophysically important molecule CH^+ [48, 49, 50] was found to be dominated by transitions involving shape resonances. Predissociation experiments are the ideal investigative tool to probe the astrophysically important radiative as-

sociation reaction due to the half-collision aspects of the reaction:

$$C^+(^2P_{\frac{1}{2}}) + H(^2S) \rightarrow CH^+(^1\Pi) \tag{1.1}$$

The rate of Equation 1.1 is expected to be enhanced due to the shape resonances which exist for the high molecular rotation in the $^1\Pi$ state. This cannot, however, account for the unexpectedly large abundance of CH^+ found in interstellar clouds [51].

SiH^+ [52] has a photodissociation spectrum which is best described in terms of Feshbach resonances (where a bound electronic state is coupled to the continuum of state[s] correlating to a lower dissociation asymptote than the bound state). Similarly, Carrington and Softley have shown that $HeNe^+$ [53] dissociates along an asymptote lower than that to which the upper electronic state correlates.

Over the last twenty years, many molecular ions have been studied using fast ion beams and both fixed frequency rare gas ion lasers with Doppler tuning and tunable dye lasers, interesting examples include PH^+ [54], SH^+ [55], NH^+ [56], OH^+ [57, 58], NO^+ [59], N_2^{2+} [60] and HF^+ [61]

A novel technique has recently been used by Hechtfischer et al. to record the near-threshold photodissociation spectra of CH^+ [62]. A CH^+ beam is created using a Van-der-Graaf accelerator to electron strip CH^-. The CH^+ molecules are injected into an ion storage 'ring' of 55.4 m circumference. Inside the 'ring', photodissociation is induced using a pulse laser in the frequency range 300-330 nm which is made collinear with the ion beam in a straight section of the 'ring'. Shortly after the interaction region the fragment ions are separated from the parent beam and their arrival is detected on a micro-channel plate. Due to the long storage time of ions inside the molecular beam (up to 30 s), it proved possible to examine different rovibronic transitions as the CH^+ cooled. Transitions from the lowest vibrational state of CH^+ to near-threshold states were probed using UV laser radiation. The majority of transitions in the region between 32,000 and 33,000 cm^{-1} are thought to be $^1\Pi$-$^1\Sigma^+$ transitions [63] and are associated with storage times of between 15 and 30 seconds. The $b^3\Sigma^-$-$a^3\Pi$ transitions (between 31,500-35,000cm^{-1}) are associated with storage times of between 0.4 and 1 s.

Another interesting possibility for future fast ion beam studies involves an 'electrostatic bottle', developed by Zajfman and co-workers [64]. This apparatus is based around the idea of trapping a moving ion beam between two sets of cylindrical electrodes in much the same way as an optical resonator

traps photons between two mirrors. A conventional fast ion beam is created in an external ion source, accelerated up to energies of approximately 4 keV and mass selected. The ion beam is collimated, focussed and directed into the trap. After passing through the (initially earthed) entrance electrodes, the beam reaches the exit electrodes, where it is stopped, focussed and reflected back by voltages of up to 10 kV. The entrance electrodes then have a similar field applied as the exit electrodes and the ion beam is trapped between the two sets of electrodes. This apparatus offers several advantages over conventional ion storage techniques due to the long storage times available (up to a few seconds); cold molecular ions (due to radiative cooling in the trap) could be easily be studied, long path lengths are possible and hence sensitive absorption techniques such as CRDS can be used. Initial experiments [65], have shown that the photodissociation of HD^+ and D_2^+ is possible using a YAG laser aligned perpendicular to the direction of the beam. Neutral fragments could be detected using a multichannel plate.

Chapter 2 Experimental

2.1 Introduction

The chapter outlines the technique and apparatus used to record absorption spectra of molecular ions through detection of photoproduct daughter ions arising from a predissociated excited electronic state. Ions are excited by tunable laser radiation from a lower state to a metastable state which lies above the dissociation limit and has a lifetime which falls within the experimental window. Photofragment spectroscopy can not only be considered as a method for recording the 'absorption spectrum' of a molecule, but also as a probe of the dissociation processes occurring within that molecule, e.g. state selective lifetime measurements and the competition between different pathways to dissociation can be studied. The experiment can also be considered in terms of atom-ion scattering as a half-collision, with 'resonances' occurring when a bound state is coupled to a continuum state. (The term resonance arises from scattering terminology and is defined as the change in the character of the continuum state due to the influence of a bound state.) Laser photofragment spectroscopy therefore studies the region of intermediate separation between bound molecular states and separated atomic states. This region is often poorly probed through traditional absorption and emission techniques.

For the spectroscopic experiments, a fast ion beam of molecular ions interacts collinearly with a frequency tunable laser beam and transitions are observed by monitoring the production of fragment ions as a function of excitation wavelength (see Figure 2.1).

For energy release experiments, a beam of molecular ions is coaxially irradiated by laser radiation of a fixed wavelength corresponding to a spectroscopic transition. An energy release spectrum for the fragments is taken by measuring the ion current as a function of momentum (see Figure 2.2).

2.2 Features of fast ion beam experiments

Fast ion beam laser photofragment techniques offer several advantages over and have features unique to the field of molecular spectroscopy. This section illustrates key points.

2.2.1 Mass selection

An isolated parent ion species from a precursor gas can be studied through the use of an electromagnetic sector, which selects ions by their mass to

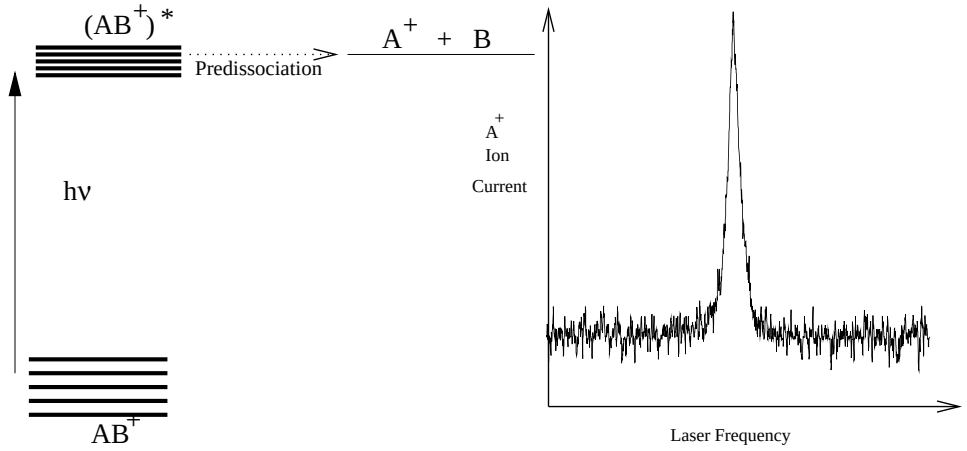

Figure 2.1 Principles of Laser Photofragment Spectroscopy

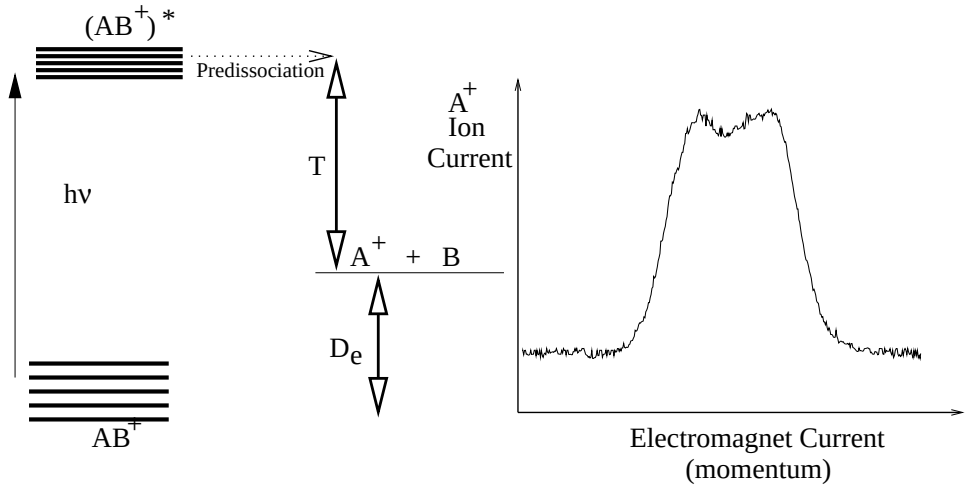

Figure 2.2 Principles of Energy Release Experiments, where T is the kinetic energy released upon dissociation and D_e the dissociation energy of the ground state.

charge ratio. This allows an immediate identification of a carrier with the recorded spectrum. An isotopically pure carrier can be selected and several isotopes of the same molecular species can be studied, simplifying the assignment process.

2.2.2 Doppler Effects

Ion beams are accelerated to high voltages (speeds $\approx 10^5$ ms^{-1}) in laser photofragment experiments in order to utilise kinematic compression. This reduces the Doppler broadening of spectral lines, giving high resolution spectra (< 0.01 cm^{-1} resolution) when used in conjunction with low linewidth laser radiation. The high speed of the molecular ion beam (which travels in

the same direction as the laser radiation) causes a Doppler shift.

Doppler Shift

If ions are travelling at high velocities in the same direction as the laser radiation, a positive Doppler shift occurs (i.e. the molecular transition frequency is lower than the observed laboratory transition frequency.) In general, the transition frequency ν_t for a particle travelling at velocity, v is given by:

$$\nu_{\mathrm{t}} = \nu_{\mathrm{o}} \left(\frac{1 - \frac{\mathrm{v}}{\mathrm{c}}}{1 + \frac{\mathrm{v}}{\mathrm{c}}} \right)^{\frac{1}{2}} \tag{2.1}$$

where ν_o is the observed frequency and c is the speed of light in a vacuum. For a molecule such as GeH^+, at an acceleration voltage of 1,425 V, this corresponds to a positive shift of approximately 3.5 cm^{-1} at 17,500 cm^{-1}.

Kinematic Compression

The ion beam is not perfectly mono-energetic due to the different positions of the molecules inside the source block upon ionisation, their different motions and the geometry of the source region. This results in ions leaving the source with a finite energy spread ΔE. However, improved resolution is obtained by accelerating the molecules from the ionisation region using high voltages, resulting in *velocity bunching* or *kinematic compression* (see Figure 2.3.) Ions which are accelerated from the ion source with high velocities (high voltages) have a reduced velocity spread (and hence Doppler width) for a given energy spread in the ion source.

2.2.3 Lifetimes and Line shapes

In order for photofragment ions to arrive at the electron multiplier, the excited state must dissociate in the time taken for the molecule to traverse the flight region. This places an upper limit on the possible lifetimes observable in an ion beam apparatus. The lower limit is governed by the laser line width; states with small lifetimes (seen as very broad lines) are inefficiently pumped due to the narrow line width of the dye laser, making detection difficult.
The line shape in the absence of Doppler broadening is a Lorentzian, where Γ, the Full Width at Half Maximum (FWHM) is related to the lifetime (τ) through the Heisenberg Uncertainty Principle:

$$\Gamma(\mathrm{cm}^{-1}) \approx \frac{5.3 \times 10^{-12}}{\tau(s)} \tag{2.2}$$

The lifetime of the upper state can therefore readily be measured by photofragmentation techniques and the mechanism for dissociation inferred. Broaden-

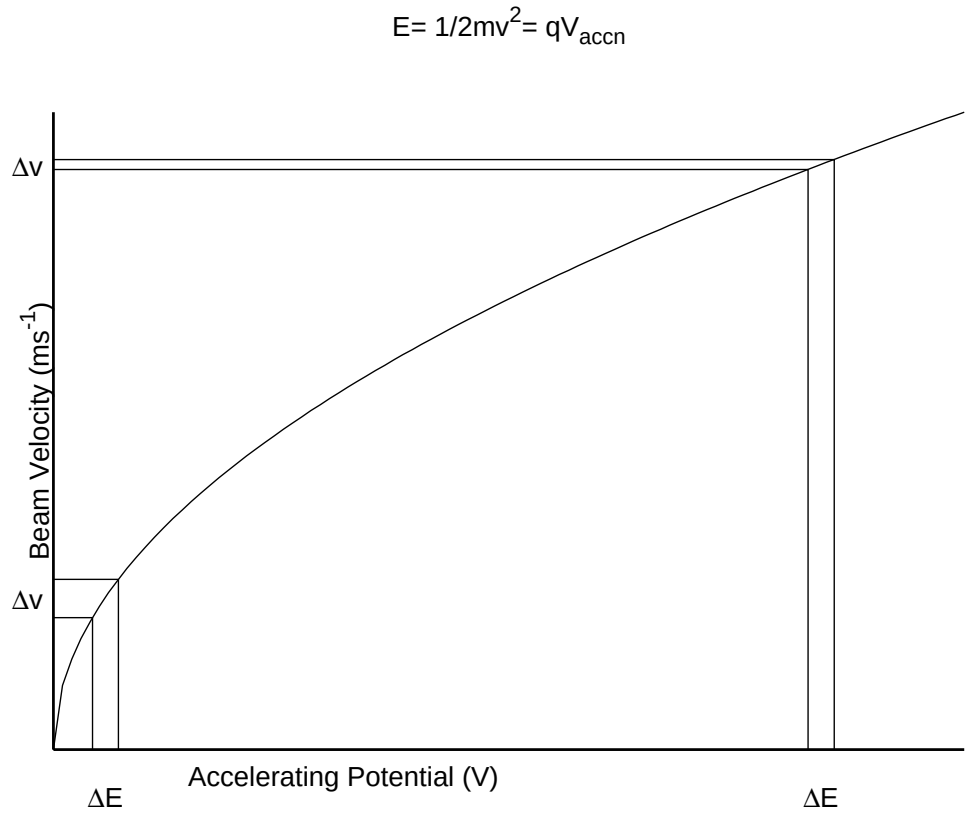

Figure 2.3 Figure showing kinematic compression in a fast ion beam. Note the narrowing of the velocity spread at high acceleration potentials.

ing occurs due to the geometry and potentials of the source. This shape can be approximated to a Gaussian and so the overall profile is approximated to a convolution of a Gaussian line shape with a Lorentzian. This line shape is known as a Voigt profile [66] and all recorded spectroscopic lines were fitted to a Voigt profile using the PEAKFIT or GNUPLOT programs.

2.2.4 Source Conditions

The electron impact ionisation of the precursor gas can create molecular ions in excited electronic, vibrational and rotational states, especially for fragment ions e.g. GeH^+ from GeH_4. Due to the short flight time of the ions through the apparatus ($\approx 10^{-6}$ seconds) and a low pressure in the flight region (10^{-8} torr), there are few opportunities for collisional relaxation thereby allowing excited states of a molecular ion to be probed.

2.2.5 Laser/Ion Beam Overlap

Four sets of electrostatic lenses (mounted at the ion source, after the first electromagnetic sector and before and after the second electromagnet) ensure

optimal overlap between the ion beam and the high power laser radiation (of up to 1 W). The ion current is measured at the lens stacks with Total Ion Monitor (TIM) plates to allow monitoring of any beam fluctuations and magnetic sector drift.

2.3 Apparatus

2.3.1 Overview

A precursor gas is bombarded with an electron beam to create molecular ions, which are accelerated out of the source by an electric field applied to the source region. Mass selection of the 'parent' species occurs at a magnetic sector. The ions are focused into a beam and irradiated coaxially by a tunable dye laser, causing dissociation. The fragment (or 'daughter') ion is selected with a second magnetic sector, and detected at an electron multiplier. Lock-in detection is used to reduce noise due to unimolecular and collisional dissociation in the beam.

2.3.2 Ion source

Gas enters the source chamber through either one or two gas lines regulated by a leak valve and passes into a confined region (source block) through two Teflon feedthroughs where it is bombarded with ca. 70 eV electrons from a thoriated tungsten filament. The electrons are detected at a trap, which allows regulation of the current of electrons using a feedback loop. Trap currents of 500 μA for a filament current of 4 A are typical. Two small permanent magnets cause the electrons to spiral, increasing their flight path length and subsequently increasing the ionisation yield. The source block is kept at a high voltage (up to +5 kV) with respect to an earthed extraction slit outside the source. Positive ions are accelerated from the source region, whereupon ion optics align and focus the beam. The experimental apparatus is shown in Figure 2.4.

2.3.3 Flight Region

A 90°, 6 cm electromagnet selects parent species by their mass to charge ratio from ions generated by the source. Ion optics focus and translationally adjust the beam as it passes into the flight region. The mechanically chopped (3 kHz) laser radiation enters the vacuum system through a window at Brewster's angle and overlaps the ion beam for 50 cm. The ion beam is refocused with a lens stack before entering the second electromagnet.

2.3.4 Vacuum System

Two Edwards diffusion pumps, (a 6″ and 4″ throat diameter) evacuate the source and flight regions, respectively. Typical operating pressures are 5×10^{-6} torr in the source region and 6×10^{-8} torr in the flight region. The

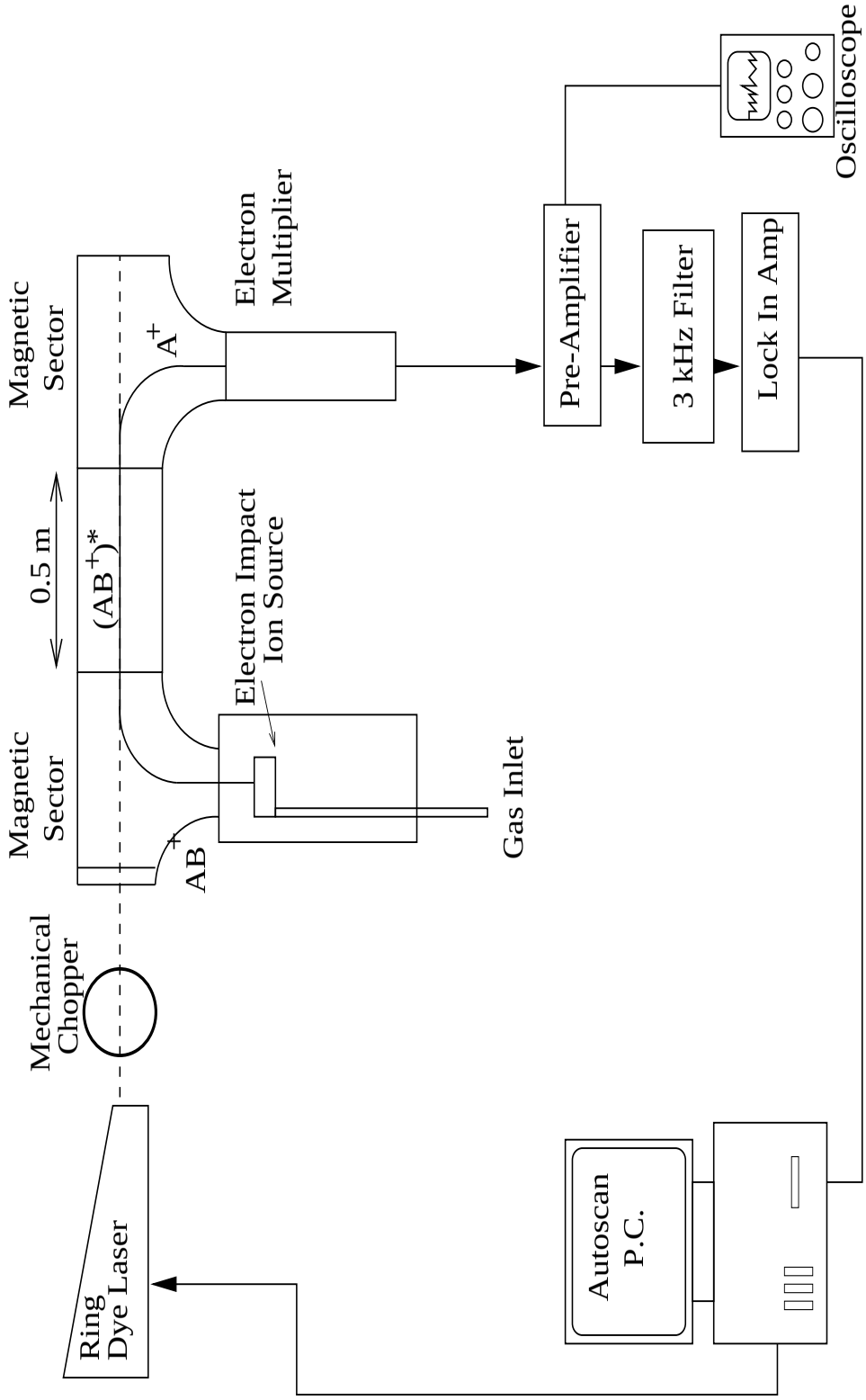

Figure 2.4 Ion beam apparatus (not to scale).

diffusion pumps are backed by an EM12 rotary pump to a pressure of 0.02 torr. Ion gauges are used to determine the pressures in the flight and source regions and a Pirani gauge used to monitor the pressure in the backing lines between the diffusion and rotary pumps.

2.3.5 Detection Electronics

The daughter ions are directed onto the first dynode of an electron multiplier (gain $\approx 10^6$) by the second electromagnet. The current from the multiplier is fed into a current preamplifier (Brookdeal 5002 or in-house built devices) and the DC voltage output monitored with an oscilloscope. The AC voltage component is fed into a lock-in amplifier (incorporating a 3 kHz filter) with a reference signal from the chopper. This discriminates against daughter ions arising from collisional or unimolecular dissociations. The 0-10 V output from the lock-in amplifier is fed into the input of the Coherent Autoscan interface system. Lock-in time constants of between 300 ms and 10 s are typical, depending on laser power, ion beam strength and the intensity of transitions.

2.4 Laser System

2.4.1 Overview

Pump laser radiation is provided by a Coherent Innova 100-20 argon ion laser prducing an output of at least 6 W. This laser pumps a ring dye laser to provide 1 W of continuous wave (cw) tunable laser radiation. The radiation from the ring dye laser is mechanically chopped and steered into the vacuum system.

2.4.2 Ring Dye Laser

A Coherent 699-29 ring dye laser is used, offering significant advantages over the standing wave models. In a standing wave dye laser, nodes and anti-nodes are set up in the jet, causing the output of the dye laser to drop when used in single frequency mode in conjunction with high pump laser power. As the ring dye laser uses a travelling wave laser system, pump power and hence power output can be significantly increased [67]. The schematic for this laser is shown in Figure 2.5. The 514.5 nm transition of the Ar^+ pump laser is focused onto a 40 PSI jet of dye solution. This causes lasing in a ring cavity, consisting of two high finesse etalons, a Bi-Refringent Filter (BRF), an optical diode and a Brewster tipping plate. The BRF reduces the laser line width to 1 cm^{-1}, enabling coarse frequency tuning. The action of the etalons causes the linewidth of the laser to decrease to approximately 3 MHz, and the frequency of this mode can be continuously scanned with a galvo driven tipping Brewster plate. Sections of length 10 GHz are scanned continuously by tilting the Brewster plate, the laser tuning elements are then reset

and the next 10 GHz is scanned. Frequency jitter is compensated for using a reference cavity and a negative feedback mechanism controlling a piezo-electrically driven mirror ('tweeter') and the tipping Brewster plate. The wavemeter is incorporated into the laser and is accurate to ± 0.005 cm^{-1}, eliminating the need for the continuous recording of an iodine spectrum and the use of external etalons. The laser radiation from the ring dye laser is chopped by a mechanical chopper and aligned to the ion beam apparatus using a series of high reflectivity surface-coated mirrors and a 1m focal length lens.

A personal computer running the Coherent AUTOSCAN program controls the various tuning elements *via* an interface and a control box. The computer scans the laser, reads the wavemeter and collects the data from the lock-in amplifier simultaneously.

Laser Dyes

Four different laser dyes were used as given in Table 2.1. The dye solution was made by dissolving the dye in spectroscopic grade methanol (99.5% purity), then adding this solution (approx. 50ml) to 0.75 ℓ of ethylene glycol (used due to its high viscosity). This gives the dye jet a stable flat shape when pumped through the specially engineered nozzle, reducing noise and mode hops of the laser. Maximum power for the ring laser is achieved when the absorption of pump radiation by the dye is 80 %. Increasing the concentration moves the lasing range to shorter wavelengths and vice-versa [68].

Dye Name	**Scan Range(cm^{-1})**	**Max. Power (mW)**
Sulphorhodamine B	16,300-16,500	300
Rhodamine B	16,200-16,600	400
Rhodamine 6G	16,500-17,850	1000
Rhodamine 110	18,050-18600	1000

Table 2.1 Regions scanned for GeH^+ and dyes used.

2.5 Energy Releases

At dissociation, the energy difference between the bound molecular state and the dissociation limit along which the molecule fragments is released as translational energy of the atomic fragments. With the laser fixed on a rovibronic absorption line, the second electromagnet can be scanned and a spectrum of the fragment ion's momentum is built up. A centre-of-mass energy release can then be deduced from the momentum profile of the fragment ion neglecting any internal atomic excitation. Measurement of the excess energy of a fragment ion measures the energy of the molecule above the dissociation limit at which it fragments. The profile of the daughter ion's momenta in the lab frame gives an indication of the trajectory of the ion,

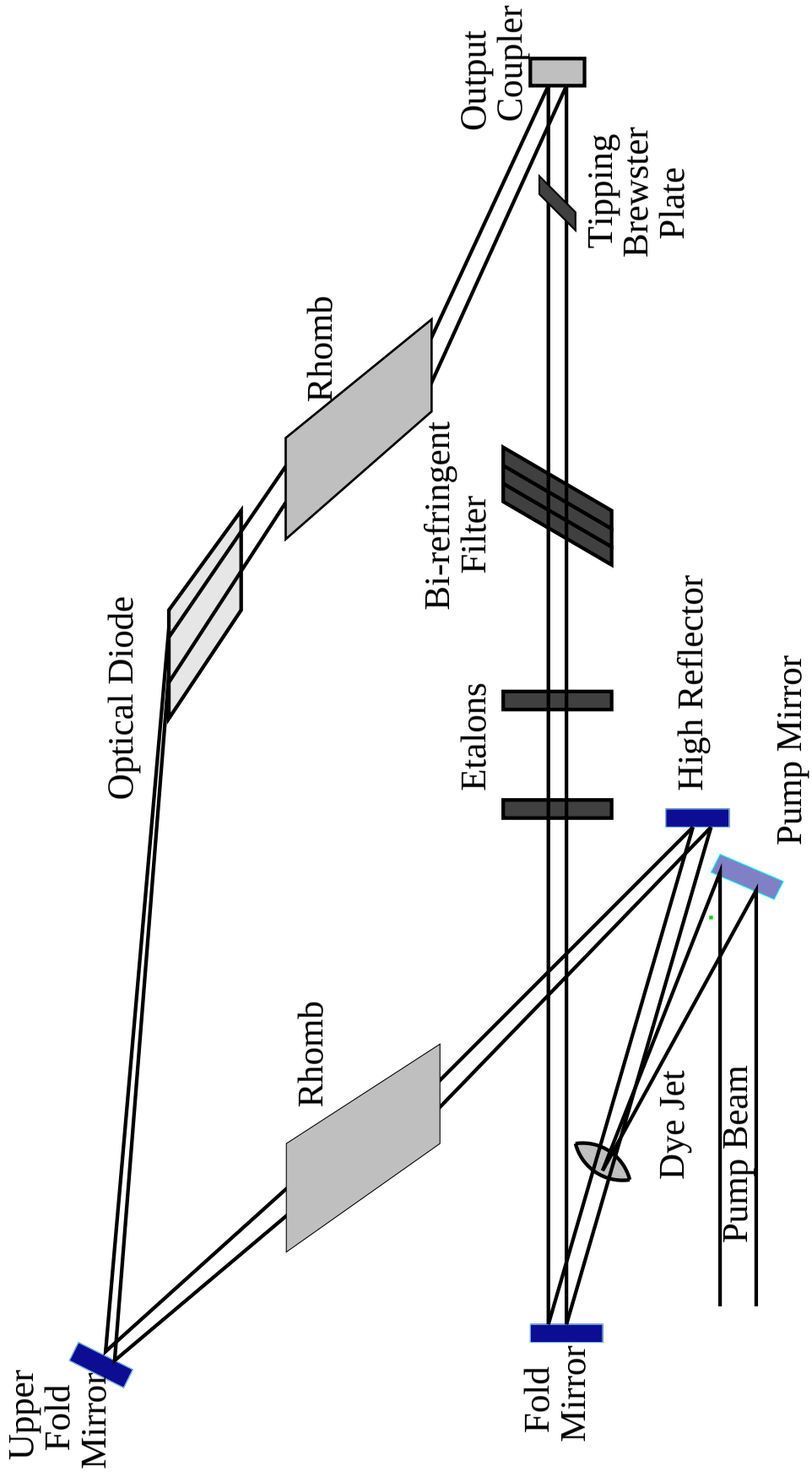

Figure 2.5 Dye laser schematic. Focus points in the cavity are not illustrated.

determining whether the transition moment is perpendicular or parallel to the laser polarisation.

In these types of experiments, the tunable dye laser is tuned to an assigned spectroscopic transition and the first electromagnet set to transmit the parent ion. The second electromagnet is scanned over the region of the daughter ion's mass and the ion current arriving at the multiplier is recorded as a function of the second magnet current. The scan voltage controlling the second electromagnet's current is recorded simultaneously with the daughter ion current to ensure accurate calibration of magnet current and simple conversion to energy releases.

2.5.1 Conversion of momentum to energy Release

A calibration proved necessary to quantify the momentum releases, due to the laser control system (AUTOSCAN) operating in fixed frequency mode. In practice, this fixes the laser frequency but the data allocation software still records the input channels as a function of wavelength. To obtain an accurate calibration of the momentum abscissa, the control (ramp) voltage of the magnetic sector was recorded simultaneously with the momentum release, and the starting and finishing points of the ramp voltage taken for each release. To calibrate the ramp wave in terms of momentum, a mass spectrum of GeH^+ was recorded using the same scan control unit.

2.5.2 Centre of Mass Energy Release

Photofragment ions undergo a small change in velocity due to the release of excess energy from the fragmentation process. The width of the momentum profile is a complex function of the momentum (and hence energy) release distribution, the electromagnet's geometry and the fragment's angular distribution. However, the average centre of mass energy release can be approximated to [69]:

$$T(eV) = \frac{m_2}{16m_3} \times \left(\frac{\Delta E}{E}\right)^2 \times V_{accn} \tag{2.3}$$

Where, $m_1^+ \rightarrow m_2^+ + m_3$, ($m_2$ is the mass of the daughter ion detected, m_3 is the mass of the other fragment), ΔE is the energy release recorded in the lab (calculated from the FWHM of the momentum release), E is the energy of the daughter ions and V_{accn} is the acceleration voltage.

The profiles of energy releases yield valuable information about the upper state of a particular transition. Fragment ions can be thought of as ejected parallel or perpendicular to the laser polarisation, depending on whether $\Delta J = 0$ (a Q transition) or $\Delta J = \pm 1$ (P and R transitions) were induced. Fragment ions arising from a Q transition are oriented along the ion beam

axis more strongly than fragments arising from a P or R transition (orientated along the laser polarisation axis). In a fast ion beam laboratory experiment which records energy (or momentum) releases using an electron multiplier, Q lines are observed as a doublet (or in the case of lower resolution, a small dip in the centre of the profile), whereas P or R lines exhibit a singlet profile [4].

2.5.3 Resolution of the Electromagnetic Sector

The momentum resolution of the electromagnet can be defined as $\frac{P}{\delta \mathrm{P}}$, where P is the momentum of the parent beam and δP is a combination of the intrinsic experimental momentum resolution and the momentum release due to photodissociation. The intrinsic experimental resolution (apparatus function) is inversely proportional to the width of the slits mounted on either side of the electromagnetic sector.

A measure of resolution was made by recording a momentum release, then recording a mass spectrum. To achieve sufficient resolution (i.e. when the momentum release width falls below the width of the intrinsic mass spectrum), narrow (24 and 50 μm) slits were mounted on either side of the electromagnetic sector. This decreased the ion current arriving at the electron multiplier by an order of magnitude, hence decreasing the number of transitions for which a momentum release can be recorded.

Chapter 3 Theory of the spectroscopy of diatomic molecules

3.1 Introduction

In this Chapter, theoretical aspects of laser photofragment spectroscopy of diatomic molecules are presented in order to explain the analysis of the recorded spectra.

3.2 Spectroscopic theory

3.2.1 Coupling of Angular Momentum

An electron in a diatomic molecule has a variety of angular momenta, associated with different electronic states and energy levels. For diatomic molecules, it is quite common to express the angular momenta in terms of projections along the internuclear axis, as these are better quantum numbers than the value of the angular momentum itself. The different types of angular momenta which are important to this study and their projections onto the internuclear axis are given in Table 3.1.

Angular Momentum	Quantum Number	Projection along Molecular axis
Total	J	$\Omega = \Lambda + \Sigma$
Electronic Orbital	L	Λ
Electronic Spin	S	Σ
Nuclear rotation	R	-
Total less spin	N= R + L	Λ

Table 3.1 Angular momenta in diatomic molecules

As angular momentum is not a scalar quantity, it is necessary to consider the addition of various angular momenta in terms of vector addition. The coupling of the momenta with the nuclear rotational angular momentum $\underline{R}$, gives rise to the different Hund's cases:

- **Hund's case (a).** Electronic motion is strongly coupled to the internuclear axis, yielding a well defined total electronic angular momentum Ω which couples with the nuclear rotational angular momentum to give the resultant J. L is strongly coupled to the internuclear axis and S is

coupled to L by Spin-Orbit coupling so S is therefore coupled to the internuclear axis (see Figure 3.1).

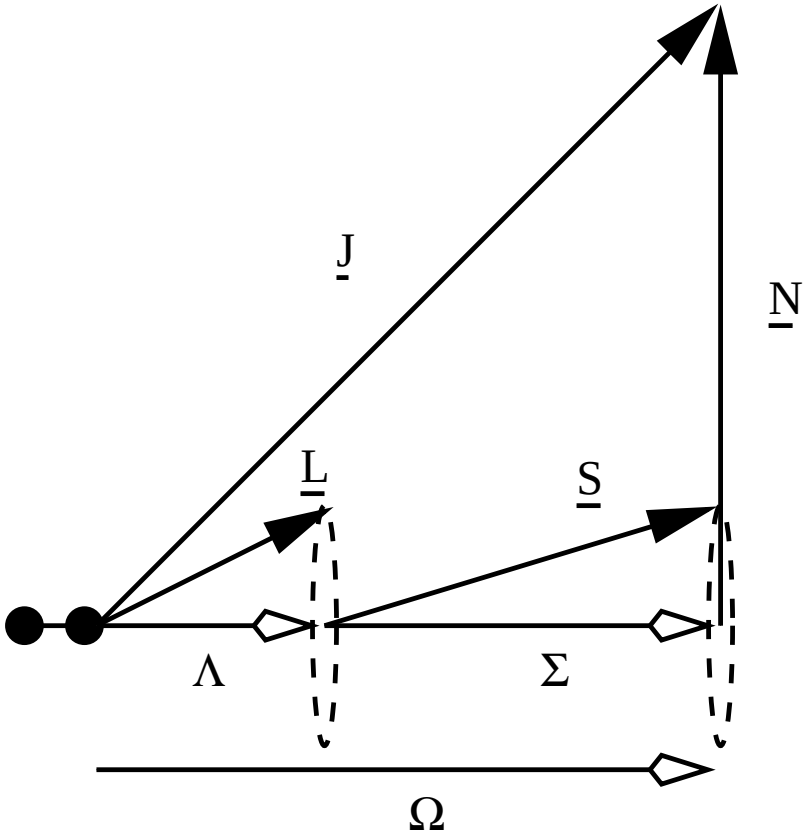

Figure 3.1 Coupling of angular momenta for Hund's case (a)

- **Hund's case (b).** Electronic spin angular momentum, S, is not coupled to the internuclear axis, thus Σ is not defined. Therefore, Ω cannot be defined, so the electronic orbital angular momentum, L, couples with the nuclear rotation R, to give a resultant N, which couples with S to give the total angular momentum J (see Figure 3.2). Hund's case (b) usually occurs in light molecules when the spin-orbit coupling is small or when $\Lambda = 0$.

- **Hund's case (c).** The spin-orbit coupling is strong and the interaction between L and S exceeds that between L and the internuclear axis. The electron spin and orbital angular momentum couple, yielding the resultant J_a which then couples along the internuclear axis to form Ω. The nuclear rotation R couples with Ω to yield the total angular momentum J. See Figure 3.3. The quantum numbers L, S, Λ and Σ are no longer good quantum numbers. A description of Hund's case (c) theory can be found in the work of Veseth [70] and examples are given in [71].

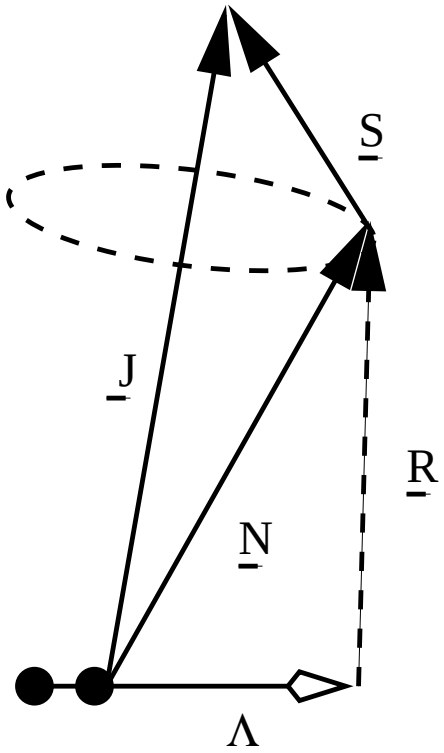

Figure 3.2 Coupling of angular momenta in Hund's case (b)

- **Hund's case (d).** Coupling between the electron and the nuclei is extremely weak. The electron orbital angular momentum couples to the nuclear rotational angular momentum, forming a resultant N, which couples with the electron spin angular momentum to give J. This case generally applies to Rydberg states of molecules, where the electron is far removed from the nuclei.

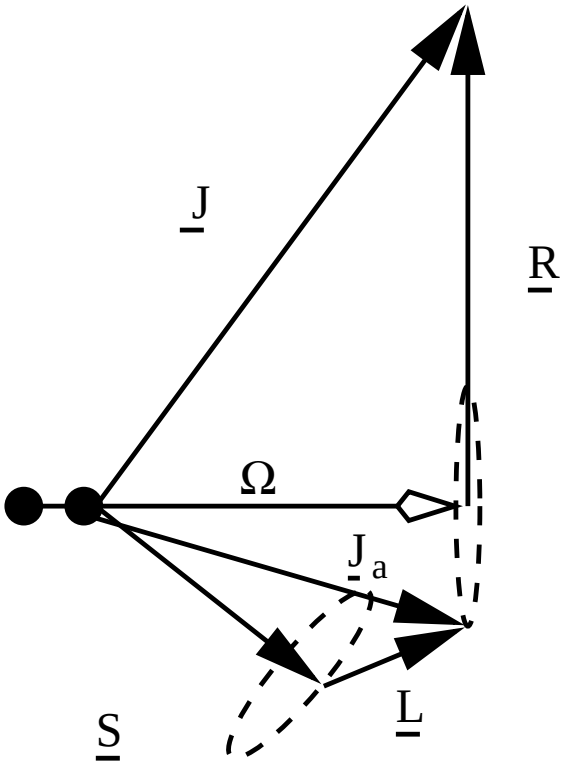

Figure 3.3 Coupling of angular momenta for Hund's case (c)

Due to the large spin-orbit coupling in GeH^+ , which arises from the large coupling in the atomic Ge^+ of 1,767 cm^{-1}, the molecule should strictly be treated using Hund's case (c). However, for the purposes of this work, it can be treated adequately within a Hund's case (a) formalism, as is the case for the isovalent CH^+ and SiH^+.

3.2.2 Lambda doubling

For all states with $\Lambda > 0$, there is a degeneracy associated with the two possible values $\pm|\Lambda|$. This arises due to the interaction between the rotational and electronic motion and is particularly significant for Π electronic states.

Consider the case of a $^1\Pi$ state. The $^1\Pi^+$ state can interact with a nearby $^1\Sigma^+$ state, leading to a shift in the energies for both the $^1\Sigma^+$ and $^1\Pi^+$ electronic states. The degeneracy of the $^1\Pi^+$ and $^1\Pi^-$ levels is then removed. It can be considered that this splitting arises due to the inability of the electrons to follow the nuclear motion as the rotation increases, leading to a mixture between the $^1\Pi$ state with electronic states of different Λ. The two electronic states, $^1\Pi^+$ and $^1\Pi^-$ have different symmetries and are labelled accordingly [72] :

$$+(-1)^J \text{ [e levels]}$$
$$-(-1)^J \text{ [f levels]}$$

For example, consider the origin of the lambda doubling in GeH^+ pictorially. Figure 3.4 shows interactions between the possible orientations of the p orbital of the germanium ion and the hydrogen s orbital [48]. The germanium and hydrogen nuclei lie along the z axis. If the electrons were able to follow the motion of the nuclei exactly with no 'slip', the two π orbitals would be degenerate. However, with increasing molecular rotation, the electrons tend to 'lag' behind the nuclei. The p_y orbital (e-component) takes on a partly σ, whereas the p_z orbital has π character. The distinction between these characteristics becomes impossible with increasing rotation, thus the degeneracy of the $^1\Pi$ state is lifted. The p_x orbital (f-component) remains unaffected with increased molecular rotation as it lies out of the plane of rotation.

The selection rules for electric dipole transitions obey the selection rule $\Delta J = 0, \pm 1$ which in terms of e and f levels correlates to:

$$\Delta J = 0, \text{ e} \leftrightarrow \text{f} \tag{3.1}$$
$$\Delta J = \pm 1, \text{ e} \leftrightarrow \text{e and f} \leftrightarrow \text{f} \tag{3.2}$$

For GeH^+ the e component of the $^1\Pi$ state is shifted (by rotational-electronic coupling to the $^1\Sigma^+$ state) with respect to the f component and can be expressed as:

$$E_v(e) = E_v(f) + q_v(J(J+1)) - q_d[J(J+1)]^2 + \ldots \tag{3.3}$$

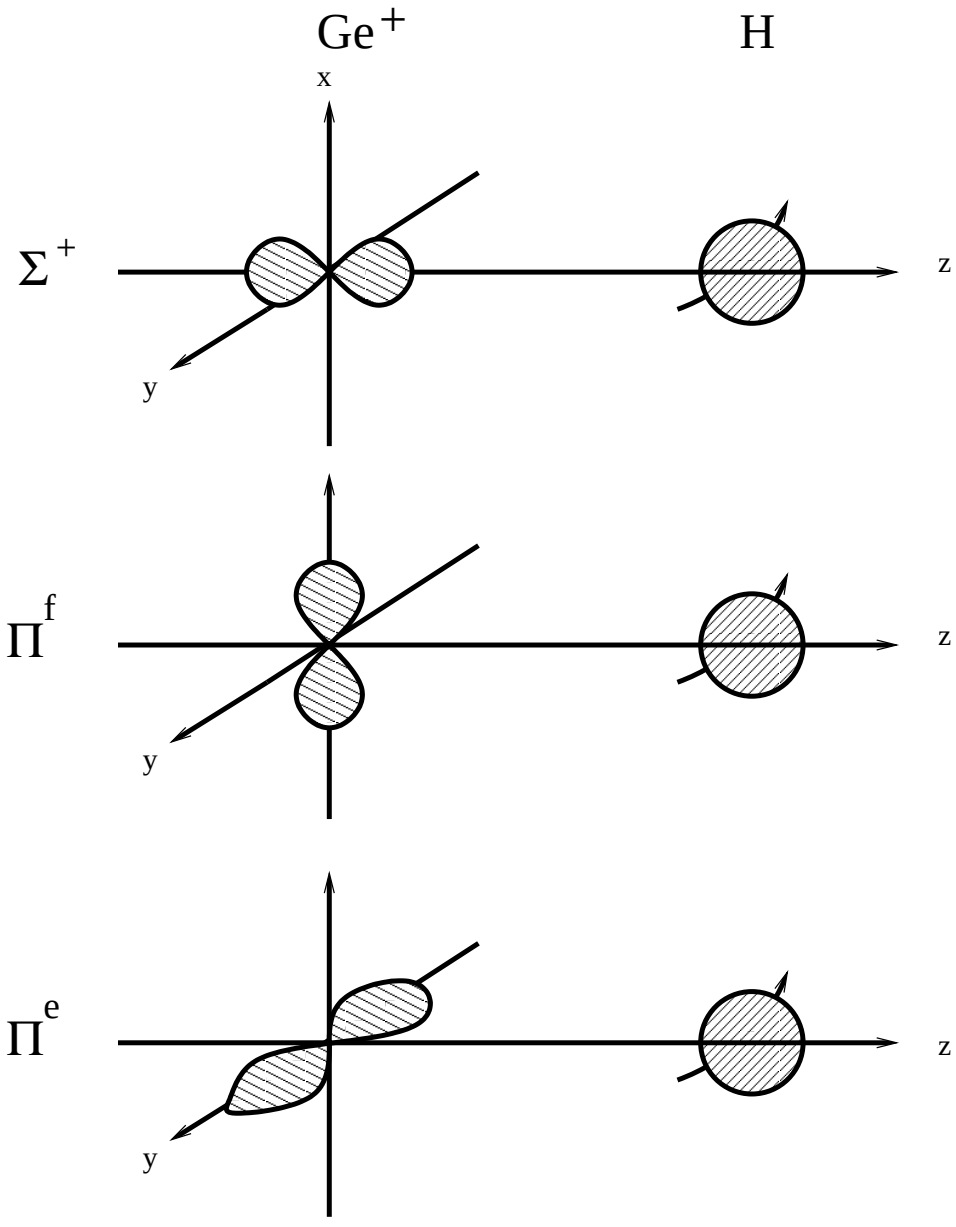

Figure 3.4 Origin of the $^1\Pi - ^1\Sigma$ lambda doubling interaction in GeH^+. Note that the Π^f orbital lies out of the plane of rotation (yz).

3.3 Predissociation

Laser photofragment spectroscopy has a close analogy with atom-ion scattering [73] and thus shares much of the same terminology. Indeed, the fragmentation process can be considered as the second half of a full collision, with exact controls over input energy. The term 'resonance' is often used to describe levels which are quasibound with respect to the continua of the separated atoms. Three mechanisms by which resonances may arise are considered here:

- Levels may lie at energies above the dissociation continuum but become trapped behind a barrier lying at intermediate internuclear separations. The origin of this barrier can be due to an avoided crossing between states of the same symmetry, or alternatively can be caused by a centrifugal term in the effective potential due to the high rotation of the molecule (shape resonance).
- Levels which are bound with respect to a potential surface lie embedded in the continuum of a state (or states) correlating to a lower dissociation asymptote. This case is known as in scattering terminology as a Feshbach resonance.
- A bound and a repulsive curve correlating to a lower dissociation asymptote cross. Radiationless transfer occurs between the rotational and vibrational states to the continuum. The wavefunctions of the two states are mixed to an extent that the wavefunction for the bound state has all the characteristics of a free state. Dissociation of the bound surface occurs in close proximity to the crossing due to the increased mixing in this region.

3.3.1 Born Oppenheimer Approximation

The Born-Oppenheimer Approximation (BOA) is a central approximation in molecular spectroscopy. It is an assumption that the electronic and nuclear motion can be separated i.e. the wavefunctions can be separated into non-interacting parts. There are no interactions between the discrete adiabatic states within the Born-Oppenheimer approximation. This breaks down at large internuclear separations, where the separation between electronic states is the same order of magnitude as the coupling between them.

The total Hamiltonian can be expressed as:

$$\mathbf{H} = \mathbf{H}_{\mathrm{el}} + \mathbf{H}_{\mathrm{rel}} + \mathbf{H}_{\mathrm{rad}} + \mathbf{H}_{\mathrm{rot}} \tag{3.4}$$

where $\mathbf{H}_{\mathrm{el}}$ is the non-relativistic electronic Hamiltonian describing the Coulombic interactions between nuclei and electrons. The eigenvalues are the Born-Oppenheimer potentials and the eigenfunctions are the adiabatic wavefunctions,:

$$\mathbf{H}_{\mathrm{el}} = -\frac{\hbar^2}{2\mathrm{m}} \sum_{\mathrm{n}} \nabla_{\mathrm{n}}^2 + \mathrm{V}(\hat{\mathrm{r}}, \mathrm{R}) \tag{3.5}$$

where m is the mass of an electron (labelled n), V is the electrostatic potential as a function of the electronic co-ordinates $\hat{r}$ and the nuclear co-ordinate R. $\mathbf{H}_{\mathrm{rel}}$ is the relativistic interaction which is approximated to the spin-orbit interaction here (neglecting spin-spin and hyperfine interactions):

$$\mathbf{H}_{\mathrm{rel}} = \mathbf{H}_{\mathrm{so}} = \sum_{\mathrm{n}} \mathrm{A}_{\mathrm{n}} \underline{\mathbf{L}}_{\mathbf{n}} . \underline{\mathbf{S}}_{\mathbf{n}} \tag{3.6}$$

This term is responsible for mixing between the $^1\Pi$ and both the $^3\Sigma$ and $^3\Pi$ states in SiH^+ and GeH^+.

$\mathbf{H}_{\mathrm{rad}}$ and $\mathbf{H}_{\mathrm{rot}}$ are the radial and rotational components of the nuclear kinetic energy operator $\mathbf{T}_{\mathrm{n}}$:

$$\mathbf{T}_{\mathrm{n}} = \mathbf{H}_{\mathrm{rot}} + \mathbf{H}_{\mathrm{rad}} \tag{3.7}$$

$$\mathbf{H}_{\mathrm{rad}} = -\frac{\hbar}{2\mu \mathrm{R}^2} . \frac{\partial}{\partial \mathrm{R}} . \left(\mathrm{R}^2 . \frac{\partial}{\partial \mathrm{R}} \right) \tag{3.8}$$

and

$$\mathbf{H}_{\mathrm{rot}} = -\frac{\hbar}{2\mu \mathrm{R}^2} . \left[\underline{\mathbf{J}} - \underline{\mathbf{L}} - \underline{\mathbf{S}} \right]^2 \tag{3.9}$$

where μ is the reduced mass. $\mathbf{H}_{\mathrm{rot}}$ furthermore can be separated into a diagonal part (corresponding to the rotational energy of the state):

$$\mathrm{E}_{\mathrm{rot}}(\mathrm{R}) = \frac{\hbar^2}{2\mu \mathrm{R}^2} \left[\mathrm{J}(\mathrm{J}+1) - \Omega^2 \right] \tag{3.10}$$

and an off-diagonal part, the second term of which is responsible for rotational electronic (Coriolis) coupling between states of different Λ but identical Σ. This is the origin of the lambda doubling, which is strongly R dependent,:

$$\mathbf{H}'_{\mathrm{rot}}(\mathrm{R}) = \frac{\hbar^2}{2\mu \mathrm{R}^2} \left[(\mathrm{L}_+ \mathrm{S}_- - \mathrm{L}_- \mathrm{S}_+) - (\mathrm{J}_+ \mathrm{L}_- + \mathrm{J}_- \mathrm{L}_+) - (\mathrm{J}_+ \mathrm{S}_- + \mathrm{J}_- \mathrm{S}_+) \right] \tag{3.11}$$

where

$$\mathbf{J}_{\pm} = \mathbf{J}_x \pm i\mathbf{J}_y \tag{3.12}$$

$$\mathbf{L}_{\pm} = \mathbf{L}_x \pm i\mathbf{L}_y \tag{3.13}$$

$$\mathbf{S}_{\pm} = \mathbf{S}_x \pm i\mathbf{S}_y \tag{3.14}$$

The $\mathbf{H}'_{\mathrm{rot}}$ term couples the angular momenta and causes the interaction between different electronic states. Rotational-electronic coupling between electronic states manifests itself as Feshbach resonances.

3.3.2 Predissociation by tunnelling

Barriers caused by avoided crossings between two states of the same symmetry are known to occur in several molecules which are isovalent with GeH^+. For example AlH has a well known barrier which occurs at large internuclear distances. This causes a breaking off in the rotational structure above $v'=1$, $J'=7$ for the $^1\Pi$ state when recorded in emission [74], whereas in absorption, the $v'=1$, $J'=16$ has been observed (for $J' \geq 12$ the lines have a marked increase in width) [74]. Due to the differences between absorption and emission detection techniques, it is more difficult to observe the emission spectra for the broad, low intensity lines lying above $J'=7$.

For GaH, which is isoelectronic with GeH^+, the $^1\Pi$ state (in the absence of any interactions between electronic states) would have an extremely shallow minimum [75]. Due to a higher lying $^1\Pi$ potential an avoided crossing is induced in the lower $^1\Pi$ state. Rotational levels of the $v'=0$ state lie trapped behind the barrier in the lower $^1\Pi$ state. Lifetime broadened lines are found in the absorption spectrum [76], where identification to rotational levels is impossible due to the large linewidths. Identification of the diffuse R and Q band heads in GaH was possible following a study of the corresponding band of GaD, where broad, but individual, rotational lines could clearly be resolved. A barrier due to an avoided crossing in the isovalent species SiH^+, CH^+ and GeH^+ is not expected to be as high due to the ion-induced dipole having a weak attractive effect between the potential surfaces. The dissociation asymptotes of the two lowest $^1\Pi$ states of GaH are separated by 33,000 cm^{-1}, whereas those of GeH^+ are separated by 61,000 cm^{-1}. Therefore the mutual repulsion in GeH^+ between the $^1\Pi$ states will be reduced in comparison with GaH.

A shape resonance is a level in which a molecule can become classically bound, due to a centrifugal barrier preventing dissociation. A centrifugal barrier is caused by orbital motion of the nuclei. Through quantum mechanical tunnelling (the radial wavefunction penetrates the barrier), the molecule can dissociate. A centrifugal energy term is added to the potential of the potential of the non-rotating molecule [$V_{\mathrm{el}}(R)$]:

$$V_{eff}(R) = V_{el}(R) + \frac{\hbar^2}{2\mu R^2}\left[J(J+1) - \Omega^2\right] \tag{3.15}$$

As can be seen from Equation 3.15 , for large values of J, V_{eff} can support a number of bound rotational states which lie above the dissociation limit of V_{el}. Molecules which exhibit such rotational barriers include H_2^+ [77], CH^+ [48, 49, 78, 79] and HeH^+ [45] .

3.3.3 Feshbach resonances

In the case of Feshbach (or Fano) type resonances, substantial mixing occurs between the bound wavefunctions of one electronic state with the wavefunctions for the continuum. This is an example of breakdown of the BOA. The bound rotational levels of one electronic state are embedded in a continuum of a state (or states) correlating to a lower dissociation asymptote. The excess (kinetic) energy on fragmentation arises from the energy gap between the bound level and the lower dissociation asymptote, as occurs in SiH^+ [52].

3.4 Potential energy surface creation and solving the Schrödinger equation using computational methods

3.4.1 Calculation of Potential Surfaces from Spectroscopic Data (RKR)

The Rydberg-Klein-Rees (RKR) method is an inversion procedure used to determine potential energy surfaces from spectroscopic parameters found for a diatomic molecule. The RKR calculations used here were performed using the **RKR1.0** program written by LeRoy [80]. This program allows the vibrational energies and rotational constants to be defined by Dunham or near dissociation expansions (not considered here). It offers the advantage that it can prevent unreasonable behaviour of the inner wall (due to inaccuracies in the experimentally derived functions) through a smoothing procedure.

The Klein integrals around which the RKR method is based are:

$$R_2(v) - R_1(v) = \frac{2}{\beta}\int_{vmin}^{v} \frac{dv'}{[G(v) - G(v')]^{\frac{1}{2}}} \equiv 2f \tag{3.16}$$

$$\frac{1}{R_1(v)} - \frac{1}{R_2(v)} = \frac{1}{2\pi\beta}\int_{vmin}^{v} \frac{B_{v'}dv'}{[G(v) - G(v')]^{\frac{1}{2}}} \equiv 2g \tag{3.17}$$

Where R_1 and R_2 are the inner and outer turning points of the potential at the energy G(v) associated with the vibrational level v. B_v is the inertial rotational constant and β is $\sqrt{\frac{2\mu}{\hbar^2}}$ (μ is the reduced mass). The two expressions for f and g can be rearranged to yield:

$$R_1(v) = \sqrt{f^2 + \frac{f}{g}} - f \tag{3.18}$$

$$R_2(v) = \sqrt{f^2 + \frac{f}{g}} + f \tag{3.19}$$

Integrals for f and g can be evaluated giving the inner and outer turning points of the potential surface, when the vibrational and rotational parameters are known.

The inversion procedure used here is only valid within the WKB approximation (first order semiclassical approach - that energy levels for the vibrating rotor can be quantized). However, this is accurate enough that when the Schrödinger equation is solved for these potentials, the eigenvalues and rotational constants are often seen to agree within the experimental uncertainties.

As mentioned earlier, **RKR1.0** allows smoothing over irregularities in the inner wall. Due to the steepness of the inner wall, uncertainties in the spectroscopic parameters (at high vibrational energies) lead to non-physical behaviour. **RKR1.0** determines non-physical behaviour in the following way: The turning point calculation starts at the potential minimum and calculates at successive energies. After completion of each turning point calculation, the program fits the turning points for that level and the two lying below it, to an equation of the functional form:

$$V_{inner}(R) = A + Be^{-\frac{C}{R}} \tag{3.20}$$

If the parameter C remains positive and varies slowly from one point to the next, then the inner wall needs no correction. However, if the wall passes through a point of inflexion, C changes sign. Thus the behaviour of C is an indicator of the need to smooth over the inner wall.

3.4.2 Calculation of Eigenvalues, Transitions and Frank-Condon Factors (LEVEL 6.0)

A program is used to solve the Schrödinger equation for bound or quasibound levels of any potential surface. **LEVEL6.0** calculates the eigenvalues of the bound and quasibound levels of a smooth one dimensional potential and then calculates centrifugal distortion constants for that potential. **LEVEL6.0** locates and calculates expectation values for all vibration-rotation levels and also the width of the quasibound shape resonances. The program optionally calculates the Einstein A coefficients, incorporating the Hönl-London rotational intensity factors.

The core of the calculation is to determine the eigenvalues $E_{v,J}$ of the one dimensional Schrödinger equation (see Equation 3.21) and the eigenfunctions of the potential $V_J(R)$. This routine is based on the Cooley-Cashion-Zare routine [81], but has the added advantage of being able to determine shape resonances. Numerical integration of Equation 3.21 is performed between two user defined points using the Numerov algorithm. To achieve this, it is necessary to specify initial values of the wavefunction at two points at the end of the range. The final value is normally set to unity, whilst the adjacent mesh point is given by the first order semiclassical or WKB wavefunction.

$$\frac{-\hbar^2}{2\mu}\frac{d^2\Psi_{v,J}(R)}{dR^2} + V_J(R)\Psi_{v,J}(R) = E_{v,J}\Psi_{v,J}(R) \tag{3.21}$$

The Cooley procedure is used to find the eigenvalues, using the following method. For any trial energy, the numerical integration proceeds inwards from the outer turning point and outwards from the inner turning point until the two solutions meet. The discontinuity in their slopes at this point is used to estimate a correction in the energy required to make the solutions converge close to the trial energy. This process is repeated until a user set convergence criterion is met. Quasibound levels are found using Airy function boundary conditions [82] to determine their energies and a semiclassical approximation to calculate the width.

Finally 'synthetic spectra' can readily be generated using the program in two potential mode, where the Schrödinger equation is solved for both potential surfaces and calculations made for transitions between the two states and the rotational line strength according to selection rules provided in the input.

Chapter 4 Spectroscopy of the GeH^+ molecular ion

4.1 Context

4.1.1 Introduction

In contrast to the isovalent species CH^+ and SiH^+ relatively little is known about the spectroscopy of GeH^+. Only one experimental study of GeH^+ has been made, and only one electronic transition ($a^3\Pi - X^1\Sigma^+$) verifies extensive *ab-initio* predictions for many states. New experimental work detailed in this Chapter redresses this imbalance by the recording, assignment and analysis of a transition between the ground and previously unobserved $^1\Pi$ electronic state.

4.1.2 Spectroscopy of GeH^+

Four electronic states of GeH^+ correlate to the first [$Ge^+(^2P) + H(^2S)$] dissociation asymptote (neglecting spin-orbit splitting): $^1\Sigma^+$, $^3\Pi$, $^1\Pi$ and $^3\Sigma$. The potential energy curves calculated for these states are given in Figure 4.1.
The first spectrum of GeH^+ was observed by Tsuji et al. in 1982 [83] in a helium afterglow experiment [9] similar to that used to record the $A^1\Pi - X^1\Sigma^+$ transition of SiH^+ [84]. Ions were created using charge exchange between ionised helium (99%) and GeH_4 (germane) (1%). A spectrum is recorded by observing the emission of flowing gases using a monochromator and photomultiplier. The initial experiment resolved three vibrational bands which were assigned as the [0,1] and [0,0] bands of the $a^3\Pi_0 \rightarrow X^1\Sigma^+$ transition and the [0,0] band of the $^3\Pi_1 \rightarrow {}^1\Sigma^+$ transition. The data was least squares fitted yielding spectroscopic constants for $v'=0$ of the $^3\Pi_{0,1}$ states and $v''=0$, 1 of the $^1\Sigma^+$ state.

Transitions between singlet and triplet states are forbidden by the $\Delta S=0$ selection rule [Hund's case (a)]. However, transitions are allowed if the dark states can 'borrow intensity' from the singlet states through the spin-orbit interaction [85]. The spin-orbit coupling in Ge^+ is relatively large (1761 cm^{-1}) resulting in strong coupling for GeH^+.The explanation that intensity borrowing from one transition to another can account for this behaviour is not strictly correct. It only arises due to the initial exclusion of spin-orbit coupling from the Hamiltonian. A correct understanding for these spectra requires a Hund's case (c) formalism.

Using apparatus of greater sensitivity, GeH^+ was studied by Tsuji et al. to

record additional emission bands [86]. Five new vibrational bands were vibrationally assigned, but a full rotational assignment required still greater sensitivity as was achieved in a third experiment [87]. This yielded rotational constants for v=0, 1 and 2 of the $^1\Sigma^+$ state, v=0 and 1 of the $^3\Pi_0$ state and v=0 of the $^3\Pi_1$ state. Despite the large spin-orbit coupling in GeH^+, no evidence of an interaction between triplet and singlet Π states was found; the emission spectra were regular and unperturbed. Confirmation of the vibrational assignment was achieved through the analysis of the GeD^+ isotope, also recorded in emission.

4.1.3 *Ab-initio* Studies of GeH^+

The first *ab-initio* study of GeH^+ was undertaken by Binning and Curtis who calculated the potential energy curve of the ground $^1\Sigma^+$ state [88]. The first 13 electronic states of GeH^+ were studied shortly afterwards by Das and Balasubramanian [89]. Potentials were constructed and the $^1\Sigma^+$ surface was re-calculated to achieve higher accuracy. The lowest lying potentials are reproduced in Figure 4.1. The predicted electronic states were found to be in good agreement with experimental studies of $^1\Sigma^+$ and $^3\Pi$ states, and matched reasonably to extrapolations of the states of GaH and SiH^+. A shallow (almost entirely repulsive) $^1\Pi$ state was predicted. A large uncertainty in the equilibrium bond length, r_e, was given, attributed to the shallow nature of the well. A long range minimum was predicted for the $^3\Sigma$ state, and the interaction between this state and the $^1\Pi$ and $^3\Pi$ states was predicted to increase at long range.

4.2 Experimental considerations

4.2.1 Laser Spectroscopy Experiments

To record a laser photofragment spectrum, a precursor gas (5×10^{-6} torr) of Germane[1] (GeH_4) was electron impact ionised by a thoriated tungsten filament operating with a trap current of 500 μA, and accelerated from the ion source at 1425 V. The mass spectrum was recorded (Figure 4.2) and assigned. Two isotopes of GeH^+ were chosen for the experiments, $^{70}GeH^+$ and $^{74}GeH^+$. The ions were coaxially irradiated by the focused output of a CR699-29 continuous wave dye laser. Typical magnet currents used to select the parent/daughter species were 2.8 → 3.0 A. Laser photofragment spectra were recorded by detecting the Ge^+ fragment arising from predissociated electronic states. Metastable fragment ions (Ge^+) due to unimolecular and collisional dissociation were observed using the second electromagnetic sector and off-axis electron multiplier with no laser radiation. The appearance of fragment ions due to collisions was verified by increasing the pressure (by capping the flight region diffusion pump) and observing the increase in Ge^+

[1] With thanks to Dr Paul Davies

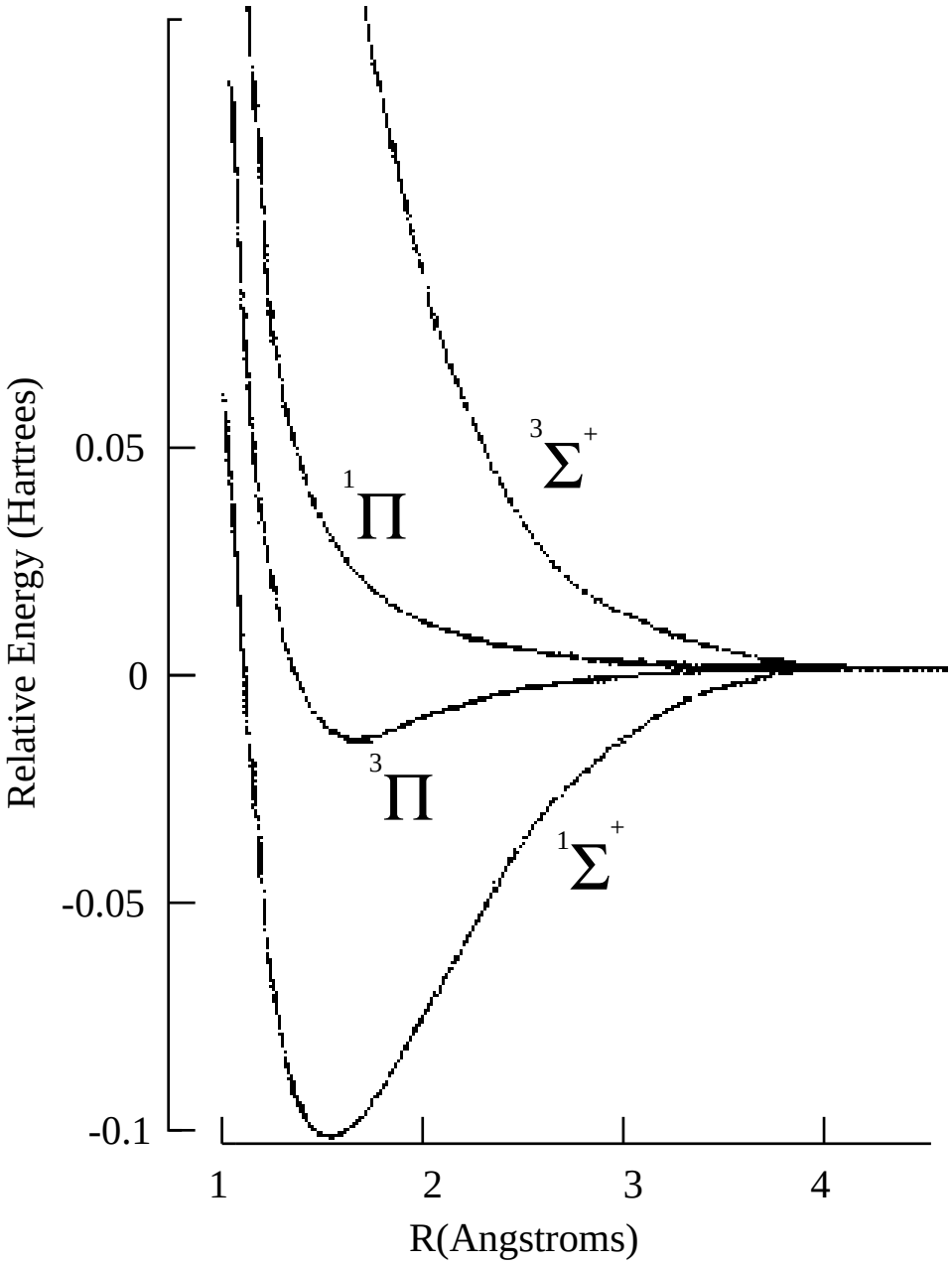

Figure 4.1 *Ab-initio* results for the first four potential energy curves of the germanium hydride cation as calculated by Das and Balasubramanian (Adapted from [89])

ion current.

A 1 m focal length lens was inserted 40 cm before the laser entered the vacuum apparatus to maximize the ion beam/laser overlap. Typical scan parameters were as follows: a 30 MHz sampling rate and a scan speed of

0.5 cm^{-1}/min. Lock-in amplifier settings: time constant 300 ms, typical sensitivity 20 mV (depending on local conditions such as ion beam current, laser power, dye age and region scanned)

As the mass/charge ratio $(m/z) = 71$ is solely attributable to the $^{70}GeH^+$ species, it was preferable to record spectra of this species for simple identification of the carrier molecule. However, the overwhelming majority of corresponding spectroscopic lines were also found for both m/z= 71 and 75. The $^{74}GeH^+$ isotope has a greater abundance (corresponding to greater ion current; see Figure 4.2) and was hence used for continuous scanning between 16,300 $cm^{-1}$and 18,500 cm^{-1}. A selective spectrum of $^{70}GeH^+$ isotope was recorded by scanning regions of interest predicted from the $^{74}GeH^+$ spectrum.

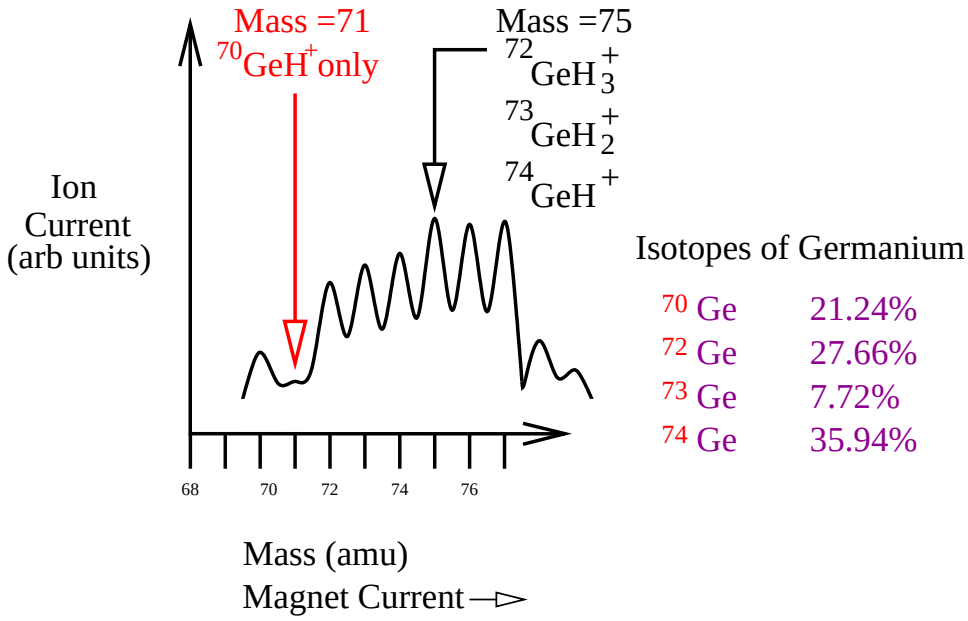

Figure 4.2 Mass spectrum of Germane (GeH_4)

4.2.2 Energy releases

The apparatus for energy release experiments was modified as follows: two slits (width 30 μm and 50 μm) were placed at the entrance and exit lens stacks of the second electromagnet respectively. This achieved sufficient sensitivity to resolve energy releases from the intrinsic experimental profile. The slits were manufactured from razor blades using a spot welder. The energy releases for the $^{74}GeH^+$ species are congested with contributions from many parent/daughter ions:

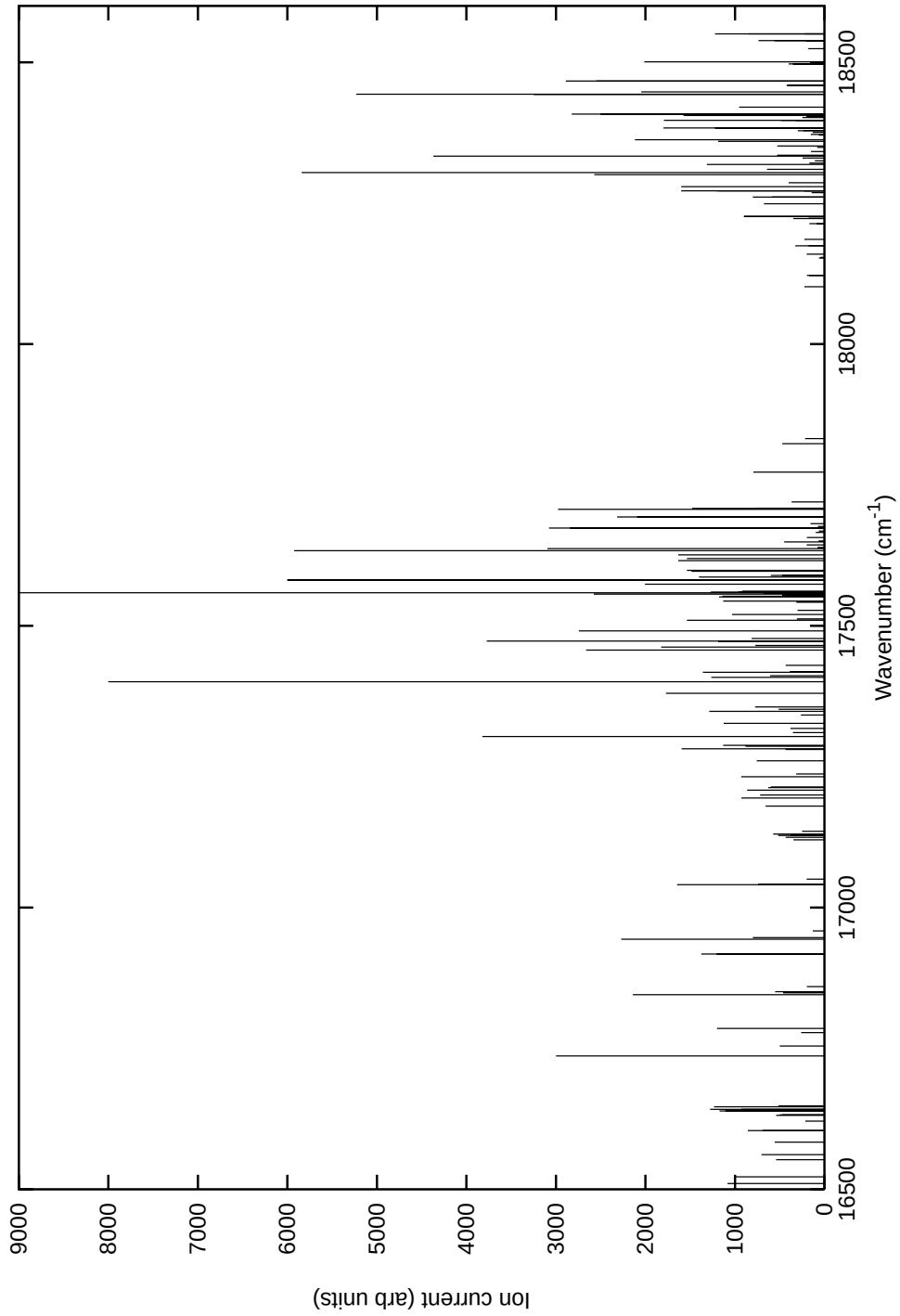

Figure 4.3 Stick Spectrum of all recorded lines of $^{74}GeH^+$. Note clusterings of lines around 16,700, 17,650 and 18,300 cm^{-1}. Laser power varies between 300 mW at 16,500 cm^{-1}, through to 1000 mW at 17,400 cm^{-1}, to 300 mW at 18,600 cm^{-1}.

$$
\begin{array}{lcl}
^{73}GeH_2^+ & \rightarrow & ^{73}Ge^+, \\
^{73}GeH_2^+ & \rightarrow & ^{73}GeH^+, \\
^{72}GeH_3^+ & \rightarrow & ^{72}GeH_2{}^+, \\
^{72}GeH_3^+ & \rightarrow & ^{72}GeH^+ \\
 & \text{and} & \\
^{72}GeH_3^+ & \rightarrow & ^{72}Ge^+.
\end{array}
$$

It proved difficult to isolate the $^{74}Ge^+$ fragment from other releases, hence isotopically pure $^{70}GeH^+$ was used, and the $^{70}Ge^+$ fragment collected. The scan voltage, which controls the current through the electromagnet, and the ion current arriving at the electron multiplier were recorded simultaneously on the AUTOSCAN data acquisition system. The scan voltage was calibrated against the magnet current, and a momentum abscissa calculated by comparison with an accurate mass spectrum.

4.3 Spectroscopic and Energy release experiments of GeH^+

The spectroscopic data was analysed in terms of line frequency, FWHM, and intensity. Line positions and intensities (un-normalised for laser power and ion beam current) are shown in Figure 4.3. A sample 50 cm^{-1} spectrum is shown in Figure 4.4.

- Over 160 lines were recorded between 16,300 and 18,500 cm^{-1} and are shown in Figure 4.3. The region between 17,800 and 18,050 cm^{-1} was not recorded.[2]
- The line widths were found to vary between 0.001 cm^{-1} (at the lower limit of experimental detection) and >1.5 cm^{-1}. A 'lifetime broadened' line is shown in Figure 4.5. Two of the narrowest assigned lines are given in Figures 4.6 and 4.7.
- A majority of the spectroscopic transitions of $^{74}GeH^+$ could also be found in $^{70}GeH^+$ accompanied by an isotopic shift of between -1 to -3 cm^{-1}.
- Lines can be seen to cluster around three regions 16,700, 17,650 and 18,300 cm^{-1} . See Figure 4.3
- Spectra of $^{74}GeH^+$ and $^{70}GeH^+$ are sufficiently resolved to observe narrow <0.01 cm^{-1} splittings between pairs of lines (see Figure 4.8).

[2]This is due to low laser power achievable with a 699-29 dye laser in this region. This portion of the spectrum lies between the Rhodamine 110 and Rhodamine 6G laser dyes (see Table 2.1), so a mix of dyes was necessary. After mixing various recipes of dyes, it was decided not to attempt this region, as the laser cavity was unstable with low power output and the scan time increased beyond an acceptable duration.

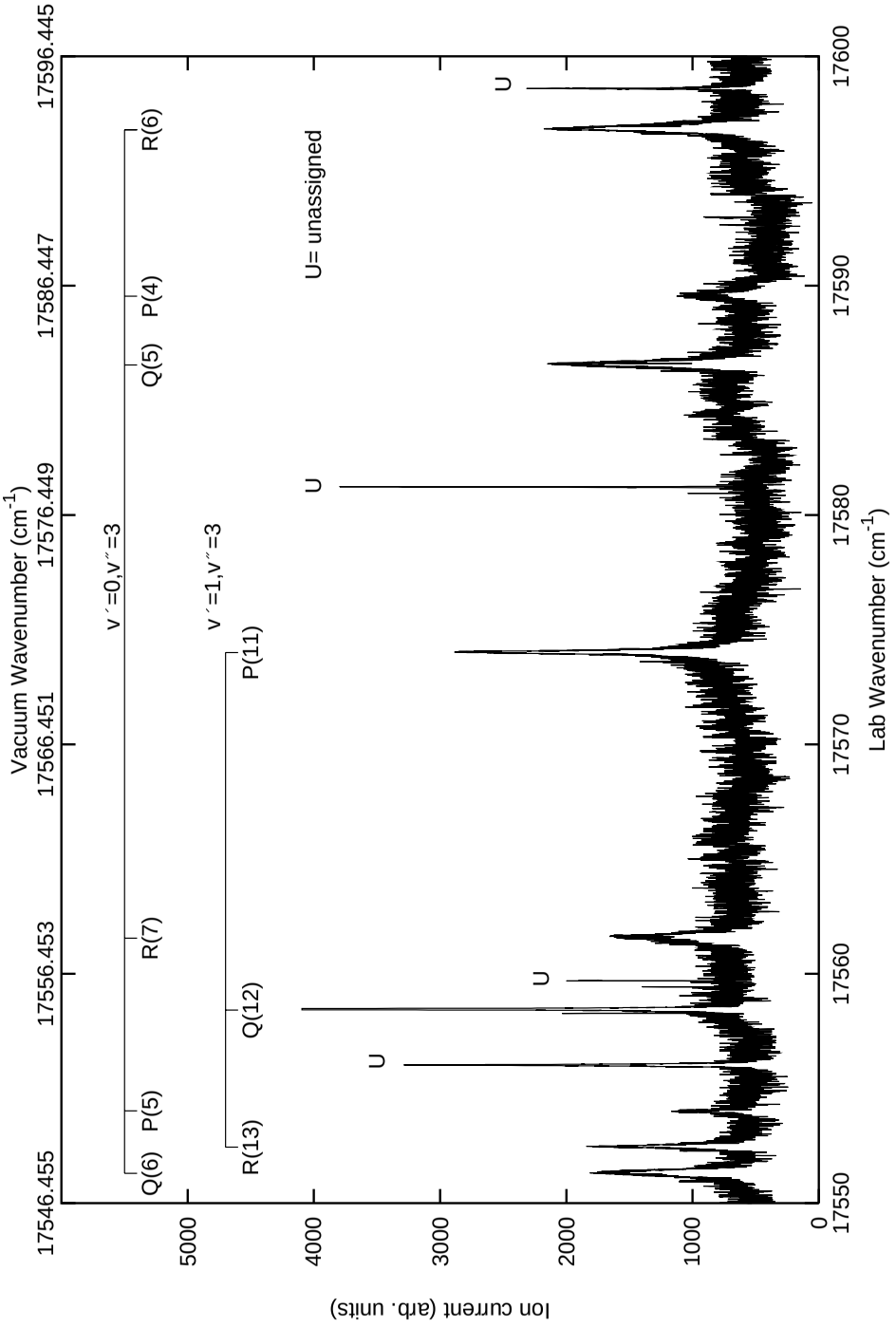

Figure 4.4 A portion of the $^{74}GeH^{+}$ spectrum recorded with 800 mW of laser power, 20 mV sensitivity, 300 ms time constant, 3×10^{-6} torr of germane and with a 30 MHz sampling rate (vacuum and lab waveno. abscissa shown). Assignments correspond to those described later in this chapter.

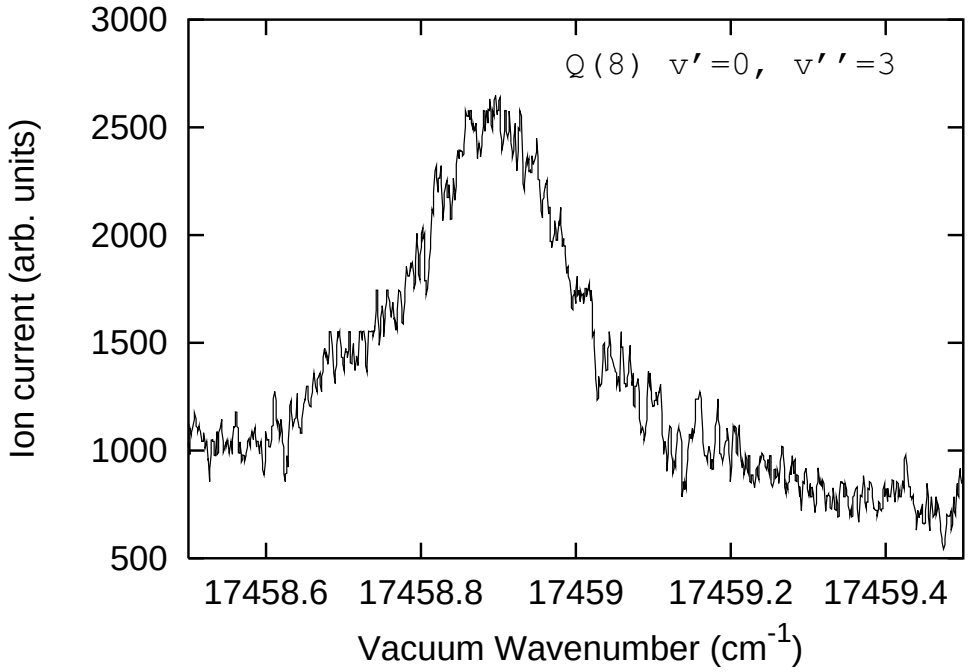

Figure 4.5 Line exhibiting large line width for low J in the v′=0 Q branch of $^{74}GeH^+$

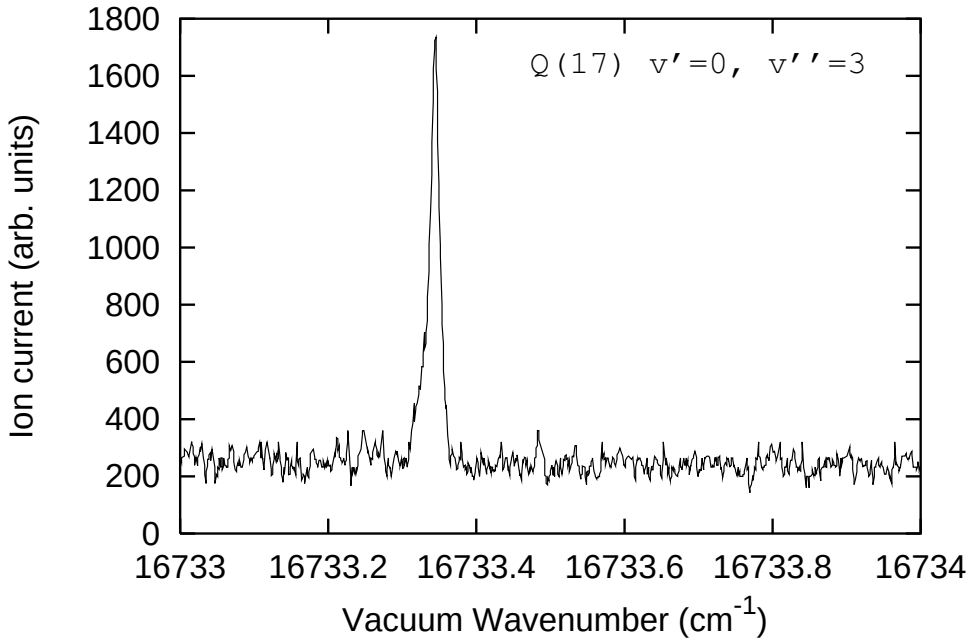

Figure 4.6 Narrow line at intermediate J in the v′=0 Q branch of $^{74}GeH^+$.

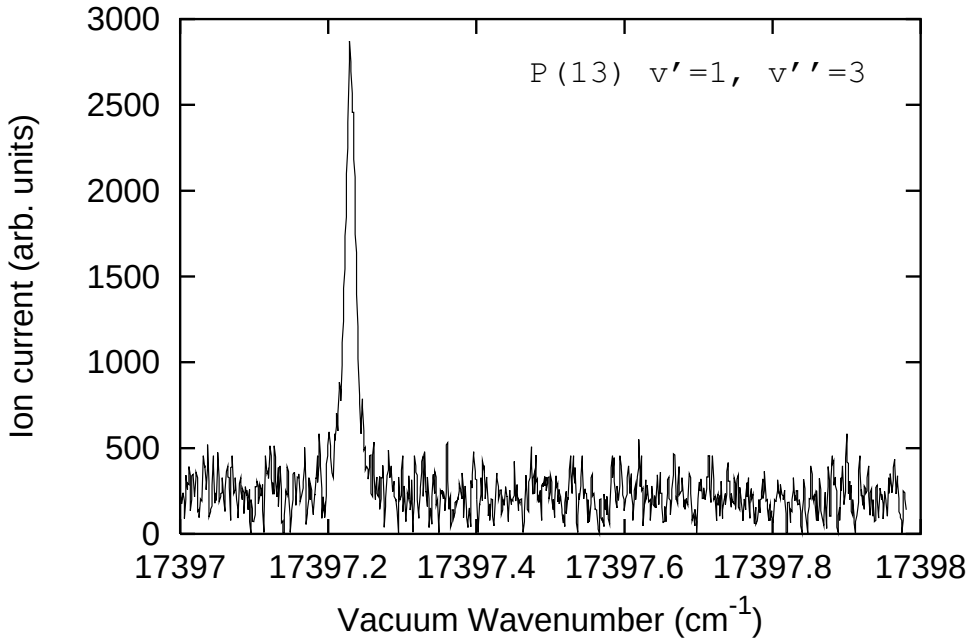

Figure 4.7 Line exhibiting 'lifetime narrowing' at intermediate J in the v′=1 state of $^{74}GeH^+$

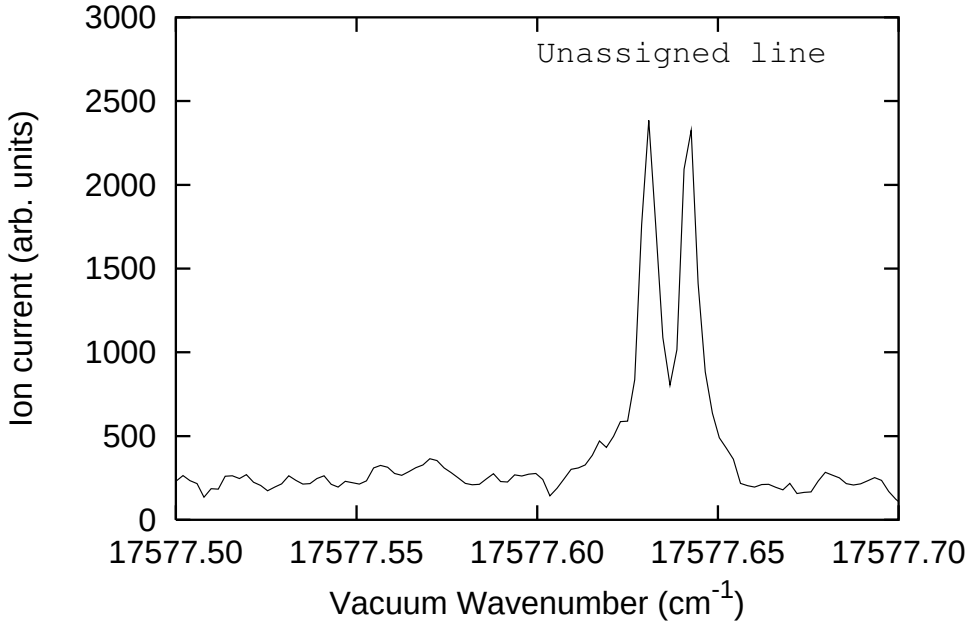

Figure 4.8 Line (unassigned) exhibiting splitting consistent with proton hyperfine splitting.

4.4 Assignment

Assignment of the laser photofragment spectrum of GeH^+ was achieved using several different methods for data extraction and analysis.:

- Experimental line frequencies
- Line signatures [line widths, hyperfine splittings and intensities]
- Ground state combination differences
- Isotope shifts
- Calculated line frequencies

4.4.1 Experimental line frequencies

The spectrum was expected to consist of transitions from the ground ($X^1\Sigma^+$) to various predissociated upper states, in particular the Π electronic states dissociating to the $^2P_{\frac{3}{2},\frac{1}{2}}$. These states are energetically accessible with the wavelength of the laser radiation used and are estimated to have reasonable Frank-Condon factors. An initial attempt was made to assign the spectrum to these electronic states. The first method used in the assignment was a search for regularities in the spectrum, i.e. comparing line positions, intensities and line width signatures. Initial attempts centred around 17,600 cm^{-1} due to the high density of lines. However, this region proved to be too congested to find regularities. Many lines in this region vary dramatically in intensity, line width and statistically significant regularities between three lines could always be found. However, none of these could be extrapolated further, making it impossible to correctly assign the spectrum using this method alone.

4.4.2 Calculation of line frequencies of transitions between electronic states

Secondly, a technique involving the creation of a full spectrum for all states using the data from the *ab-initio* and emission studies in conjunction with the programs of LeRoy [80, 90] was used. Predicted spectra could be compared directly with experimental data, allowing for small shifts due to inaccuracies in spectroscopic constants, perturbations etc. This method has an inherent disadvantage of extrapolating data from the lowest lying vibrational and rotational states (observed in the emission studies) to higher lying states. It is not possible to predict spectra accurately this way, due to uncertainties in the potential surfaces near dissociation and interactions between states. Despite these difficulties, it was hoped that an approximate spectrum could be generated. The small number of *ab-initio* parameters for the $^1\Pi$ state made the construction of a potential for this state difficult. Large uncertainties

were associated with the given parameters, adding to these difficulties.

As a first step towards assignment, simulated spectra for the $^3\Pi$-$^1\Sigma^+$ transitions were generated using parameters obtained from emission studies by Tsuji et al. on transitions between the $^3\Pi_{0^+}$, $^3\Pi_1$ and the $^1\Sigma$ states. Transitions to the $^3\Pi_2$ states are strictly forbidden due to the $\Delta\Omega = 0, \pm 1$ selection rule [74], hence can be eliminated from the possible candidates. Transitions to the $^3\Pi_1$ states will not be observed (with the exception of shape resonances) as both components correlate with the lower $(Ge^+(^2P_{\frac{1}{2}}) + H(^2S_{\frac{1}{2}}))$ asymptote.

Construction of a realistic $^1\Sigma^+$ surface was possible due to the availability of molecular parameters for the three lowest vibrational levels. A small modification to the molecular parameters from [87] was made before the behaviour of the $^1\Sigma^+$ state was considered realistic. If the parameters γ_e, B_e and α_e are used in Equation 4.1 to calculate the B values for each state with vibrational quantum number v, B_5 is seen to be larger than B_4, clearly a counter-intuitive situation, (the bond length would be expected to increase with v and therefore B decrease). Using

$$B_v = B_e - \alpha_e \left(v + \frac{1}{2}\right) + \gamma_e \left(v + \frac{1}{2}\right)^2 \tag{4.1}$$

yields,B_3=6.3275, B_4=6.2875 and B_5=6.3075, cm^{-1} when B_e=6.94, α_e=0.28 and γ_e=0.03 cm^{-1}. Due to this non-physical behaviour of B_v, a least squares fit of B_v against $(v + \frac{1}{2})$ was used to determine the value of B_e and α_e from Equation 4.2:

$$B_v = B_e - \alpha_e \left(v + \frac{1}{2}\right) \tag{4.2}$$

Fitting two parameters to three data points is not entirely satisfactory, however the resulting B_v values decrease with increasing vibrational quantum number as expected for a physical system. The values calculated for B_e and α_e are 6.90(8) and 0.19(6) cm^{-1} respectively (the numbers in brackets indicate 3σ in the last quoted digit). Potential energy curves constructed from these parameters (using the **RKR1** program [80]) were considered to be the best possible using only data from the emission studies. Any resulting predictions for higher vibrational states in the $^1\Sigma^+$ state are therefore more realistic and allow comparison with the recorded spectrum than if the unadjusted parameters were used. However, despite these efforts, no assignment could be made between the laser photofragment spectrum and the calculated spectrum for $^3\Pi$ - $^1\Sigma^+$ states.

4.4.3 Ground State Differences

Using a combination of experimental and *ab-initio* molecular parameters, it was possible to predict ground state splittings between rotational levels.

This method for assigning a spectrum is useful where the upper electronic state is strongly perturbed [52], as it relies solely on the lower state intervals between rotational levels. Two transitions labelled P(J+1) and R(J-1) will both arrive at a given J′ in the excited electronic state (P and R transitions arrive on rotational levels of the same parity) as shown in Figure 4.9. The lower state splitting is given (to first order) [91] by:

$$\Delta E = B''_v(4J + 6) \tag{4.3}$$

If the upper electronic state is strongly perturbed, the positions of the lines will move. However, the ground state splitting remains unchanged, as both the P(J+1) and R(J-1) lines will be perturbed in the same direction and by the same amount. The ground state level splittings can be used as an assignment tool provided that the states of the $^1\Sigma^+$ from which the transitions arise are sufficiently removed from the perturbing effects of the upper states. Two transitions sharing the same upper state must have identical lifetimes and hence the same line widths. A search was undertaken for all pairs of lines having the same width and which matched the predicted ground state splittings. The splittings for each vibrational state were calculated from recorded transitions of GeH^+ [92], or extrapolated from Equation 4.2

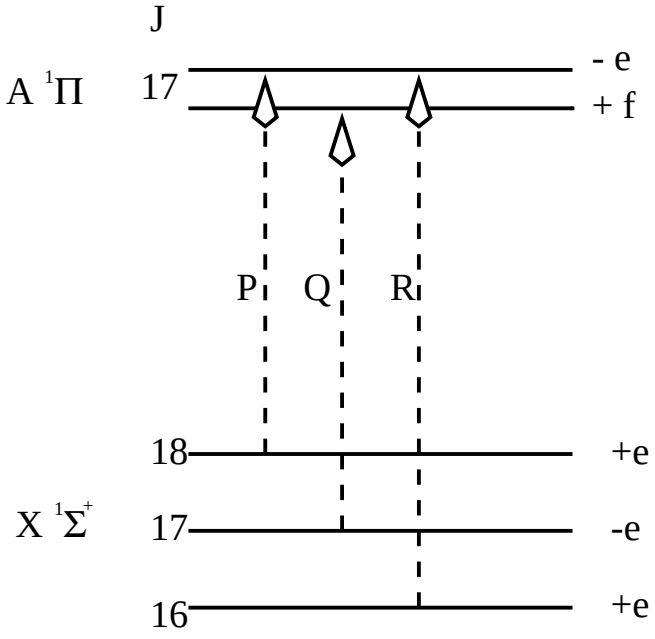

Figure 4.9 Ground state (J→J+2) differences (lambda-doubling of the $^1\Pi$ state exaggerated for clarity)

4.4.4 Isotope Shifts

The technique outlined here proved decisive in finding regularities in the spectroscopic data which lead to assignment. It is known that (to a first approximation), the isotope shift in a given vibrational band is approximately the same for all J [74]. When lines from $^{70}GeH^+$ were linked to the corresponding ones for $^{74}GeH^+$ (through matching line width, intensity and position), isotope shifts could be calculated. Lines having similar shifts could then be grouped, allowing regularities in the line positions to be found as lines for other vibrational bands were readily distinguishable.

It was found that the majority of the P-R line separations corresponded to predictions of level splittings for v''=3 of the $X^1\Sigma^+$ state. No degradation of the 'R' branch (the highest frequency lines were initially postulated as 'R' branches) was apparent. This indicated that the R branch forms a band head rapidly and hence the transitions are associated with a large change in B value. This is not observed in the emission studies (where B'=0.88 × B''), suggesting that an electronic state other than the $^3\Pi$ state was involved. The initial B' value was estimated to be 3 cm^{-1} (corresponding to an internuclear separation of 2.4 Å). This matches the predicted minimum of the $^1\Pi$ state from the *ab-initio* study by Das and Balasubramanian [89]. It should be noted that this value is too large for the upper state to be the $^3\Pi$ state. In order to quantify this B' value and other molecular parameters accurately, a least squares fitting routine was used.

4.4.5 Non-linear least squares fitting

Lines were initially assigned to vibrational and rotational states, using results from ground state level separations. Line frequencies were then used as the input into a non-linear least squares fitting routine (using the REFINE algorithm), and fitted to the following expressions:

$$\begin{aligned} A^1\Pi: \quad F_{v'}(J) = \; & B_{v'}[J(J+1)-1] - D_{v'}[J(J+1)-1]^2 \\ & + H_{v'}[J(J+1)-1]^3 \pm q_{v'}[J(J+1)] + T_{v'',v'} \end{aligned} \tag{4.4}$$

$$X^1\Sigma: \quad F_{v''}(J) = \; B_{v''}[J(J+1)] - D_{v''}[J(J+1)]^2 + H_{v''}[J(J+1)]^3 \tag{4.5}$$

Where B, D and H are the rotational parameters, q_v is the lambda doubling parameter for a particular vibrational state, (±) refers to states of e and f symmetry respectively, $T_{v',v''}$ is the separation between the vibrational states v' and v'' in the $^1\Pi$ and $^1\Sigma^+$ electronic states respectively.

One disadvantage of fitting lines using a least squares method is that a systematic error may be present in the numbering of the rotational quantum

number J. This was checked for using the method of ground state level separations outlined earlier. The Q transitions were not initially included in the fit, due to the uncertainty in the magnitude of the lambda doubling for the $^1\Pi$ state. If a large lambda doubling parameter exists for GeH^+, this would produce a significant shift in the Q branch with respect to that predicted from the P and R branches. Through trying different fits of the Q branch lines to different J quantum numbers, a definite assignment could be determined and a physically realistic q value deduced.

The assigned lines are plotted in Figure 4.10 and the line positions given in Tables A.1 and A.2. The overall standard deviation of the fits for the $^{70}GeH^+$and $^{74}GeH^+$data are 3.89×10^{-3} and 3.88×10^{-3} respectively. Molecular parameters from the least squares fitting procedure are given in Table 4.1. The magnitude of the q parameter is seen to be consistent with that found in CH^+[93] and SiH^+[94]. The lambda doubling splitting shown to be linear with J(J+1), for the low J values assigned here, suggesting that higher order terms are unnecessary. See Figure 4.11.

4.4.6 Vibrational assignment

Lower state ($^1\Sigma^+$)

The rotational constant B for the lower state of the majority of transitions (See Table 4.1) is calculated to be 6.21 cm^{-1}. This is consistent with the calculated B_3 value for this state (6.23 cm^{-1} from Equation 4.2). It is therefore proposed that the majority of transitions arise from rovibrational levels of v″=3 in the $^1\Sigma^+$ electronic state. This vibrational state is responsible for three of the observed bands, with the J = 0 level lying $\approx$ 6,650 cm^{-1} above the minimum of the $^1\Sigma^+$ electronic state. An upper estimate for the dissociation limit for GeH^+ can therefore be made. This value is calculated to be (6,650 + 17,673 =) 24,324 cm^{-1}. The $Ge^+(^2P_{\frac{1}{2}}) + H(^2S_{\frac{1}{2}})$ asymptote must lie below this value, in agreement with the *ab-initio* study, which gave this limit at 23,793 cm^{-1}.

Upper state ($^1\Pi$)

The upper state vibrational quantum number can be deduced from a consideration of the shift of the observed bands between $^{74}GeH^+$and $^{70}GeH^+$. In general, the isotope shift ($\delta\nu$) is given by

$$\delta\nu = (1-\rho)\omega_e\left(v+\frac{1}{2}\right) - \left(1-\rho^2\right)\omega_e x_e\left(v+\frac{1}{2}\right)^2 \tag{4.6}$$

where

$$\rho = \sqrt{\frac{\mu_1}{\mu_2}}. \tag{4.7}$$

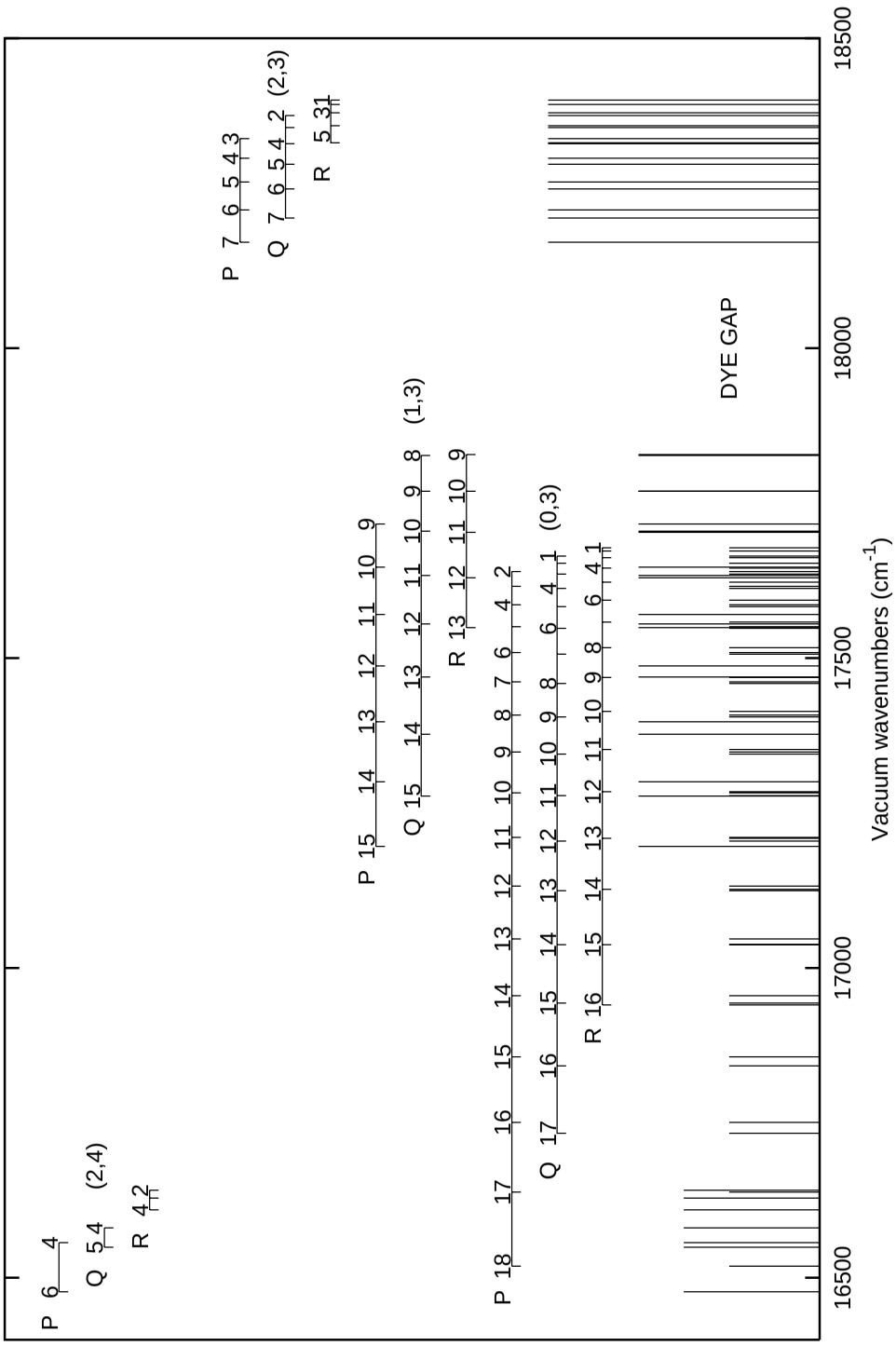

Figure 4.10 Assigned Transitions ($^1\Pi \leftarrow ^1\Sigma^+$) of GeH^+. Line intensities ar normalized to a common value for clarity.

Spectroscopic Constant	^{74}**GeH**$^+$ **(cm**$^{-1}$**)**	^{70}**GeH**$^+$ **(cm**$^{-1}$**)**
$^1\Sigma^+$ **state**		
B_3	6.2104(9)	6.2148(8)
$D_3 \times 10^4$	3.02(2)	3.02(2)
B_4	6.042(8)	-
$D_4 \times 10^4$	5(1)	-
$^1\Pi$ **state**		
B_0	3.319(1)	3.321(1)
$D_0 \times 10^4$	9.30(6)	9.26(6)
$H_0 \times 10^7$	2.5(1)	2.4(1)
$q_0 \times 10^3$	5.9(1)	5.80(8)
B_1	3.131(8)	3.110(6)
$D_1 \times 10^4$	11.4(6)	9.7(1)
$H_1 \times 10^7$	9(1)	5.1(9)
$q_1 \times 10^3$	7.2(2)	7.6(1)
B_2	3.000(3)	2.998(4)
$D_2 \times 10^4$	19.1(6)	18.1(6)
$q_2 \times 10^3$	4.9(9)	6.0(8)
$T_{0,3}$	17673.64(2)	17671.32(3)
$T_{1,3}$	18055.7(3)	18054.5(3)
$T_{2,3}$	18397.64(5)	18395.86(6)

Table 4.1 Molecular parameters from the least squares fitting to $^1\Pi$-$^1\Sigma^+$ transitions. (Bracketed values give 3σ in the last quoted value).

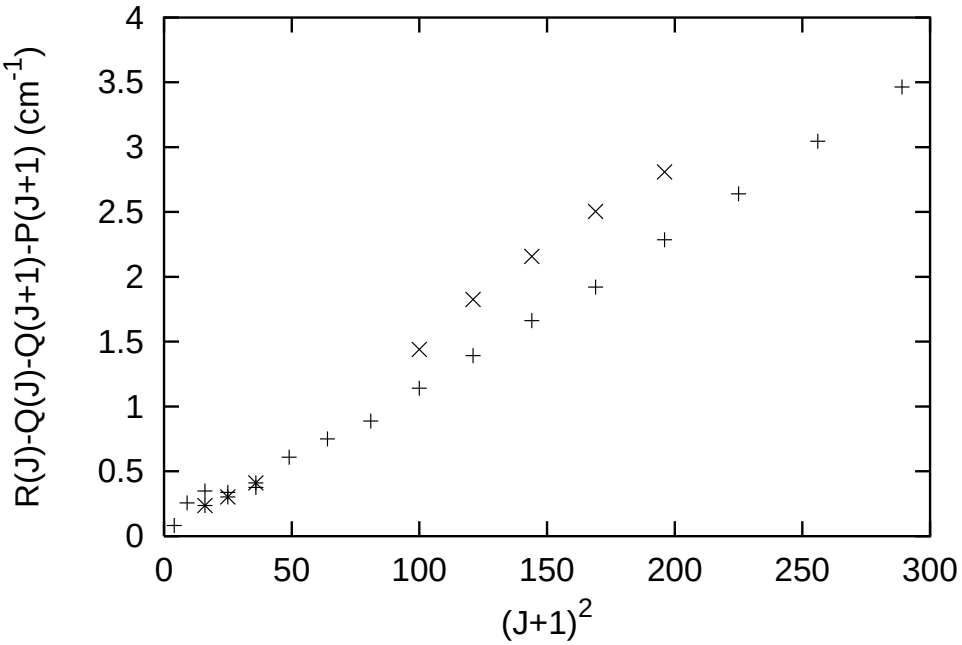

Figure 4.11 Lambda doubling in $^{74}GeH^+$. The v′=0,1 and 2 states are represented by +, × and ∗ respectively.

For this case:

$$T_n\ (^{70}GeH^+) - T_n\ (^{74}GeH^+) = \delta\nu(\text{lower}) - \delta\nu(\text{upper}) \tag{4.8}$$

$$\delta\nu\,(\text{lower}) = (1-\rho)\,\omega_e''\left(v'' + \frac{1}{2}\right) - \left(1-\rho^2\right)\omega_e x_e''\left(v'' + \frac{1}{2}\right)^2 \tag{4.9}$$

$$\delta\nu\,(\text{upper}) = (1-\rho)\,\omega_e'\left(v' + \frac{1}{2}\right) - \left(1-\rho^2\right)\omega_e x_e'\left(v' + \frac{1}{2}\right)^2 \tag{4.10}$$

The values of ω_e'' and $\omega_e x_e''$ are taken from the data of Tsuji et al. [87] and μ_1 and μ_2 are the reduced masses of $^{70}GeH^+$ and $^{74}GeH^+$ respectively.

For a transition between the lowest observed vibrational level of the $^1\Pi$ state and the v″=3 of the $^1\Sigma^+$ state, an isotope shift was calculated. Comparison was then made with the isotope shift found from Table 4.1.

The parameter $\omega_e x_e'$ is obtainable explicitly by solving three simultaneous equations for G(v). A vibrational assignment was then found by assuming the first observed vibrational state (band origin 17,674 cm^{-1}) can be assigned to i≡v′ = 0. An isotope shift and ω_e' were calculated. Comparison

was then made with the experimental data. The first observed state was then assumed to be the i≡v′=1. The isotope shift and ω_e' were recalculated. In this manner, the isotope shift was calculated assuming an assignment of the 17,674 cm^{-1} band to v′=0→4. The result of these calculations are found in Table 4.2. The best fit occurs when i=0, i.e. the lowest observed band (17,674 cm^{-1}) of the $^1\Pi$ state is the v′=0 vibrational band.

This method of vibrational assignment by isotope shift can be applied to any of the observed bands (i.e band origins at 17,674, 18,056, 18,398 cm^{-1}). However the state with a band origin at 17,674 cm^{-1} was chosen initially due to the large number of assigned lines in both isotopes and the lowest uncertainty in the location of the band origin (See Figure 4.10 and Table 4.1).

i	ω_e	**Shift assuming v′=i**
Experimental		**2.32(4)**
Calculated		
0	422.227300	2.322745
1	462.370400	2.168231
2	502.513500	2.013711
3	542.656600	1.859185
4	582.799700	1.704653

Table 4.2 Comparison between the recorded and predicted isotope shift for the band with a 17,674 cm^{-1} origin (all values given in cm^{-1})

An extensive search for transitions attributable to a supposed lower lying vibrational states of the $^1\Pi$ was undertaken using the methods outlined above. However, no lines were found which could be assigned to such states, further confirming the assignment obtained.

4.4.7 Evidence for assignments

Having assigned the lines rotationally, vibrationally and electronically, it was possible to use the fitted experimental data to improve upon the existing parameters for the $^1\Sigma^+$ state and to make comparisons between experimental and *ab-initio* parameters for both the $^1\Pi$ and $^1\Sigma^+$ states (Table 4.3). The B_e values for the two electronic states can be seen to agree reason-

ably with the predicted values from the study by Das and Balasubramanian [89]. The parameter ω_e is a factor of two greater than that predicted by the *ab-initio* calculation. This is probably due to the difference between the shallow $^1\Pi$ surface predicted and the observation that the well is at least 1,000 cm^{-1} deep (and supports at least three bound vibrational states). The value of T_e needs revising upwards compared with the ab-initio prediction as a consequence of the observed equilibrium of the $^1\Pi$ state lying 800 cm^{-1} higher than that predicted in the *ab-initio* studies [89].

Results taken from the emission [87] studies were combined with predissociation results to provide the most accurate set of rotational parameters for the $^1\Sigma^+$ state. The lower part of Table 4.3 gives these values and makes comparison to the original emission study values. The B_e value from the predissociation data is found to lie within the experimental uncertainty of the emission studies, but α_e is lower than that found in emission. This is almost certainly due to the inclusion of an (incorrect) γ_e term in Equation 4.1.

4.4.8 Internal consistency

The high precision with which line frequencies were measured allows accurate determination of the exact ground state level separations from P and R branches. If two pairs of (P,R) transitions differ only in their upper vibrational state, the line spacings between them should agree exactly (within experimental uncertainty). This is found to be the case for all lines for which this can be checked. See Table 4.5.

Parameter	^{74}**GeH$^+$** (cm^{-1})	^{70}**GeH$^+$** (cm^{-1})	**Literature** (cm^{-1})
$^1\Pi$ state			
			Ab-initio [89]
B_e	3.40(2)	3.40(2)	2.1
			3.1(8) †
α_e	0.16(1)	0.16(2)	N/A
ω_e	422(2)	425.0(8)	230
$\omega_e x_e$	20.1(9) done	20.9(6)	N/A
T_e	24115(2)	24113.8(8)	23270
$^1\Sigma^+$ state			
			Emission [87]
B_e	6.90(6)	6.90(5)	6.94(5)
α_e	0.20(2)	0.20(1)	0.28(5)

Table 4.3 Comparison of the molecular parameters (cm^{-1}) for the electronic states of GeH^+ in the fast ion work with *ab-initio* and experimental work results [89] and [87]. The B_e parameter marked † is calculated using an improved basis set.

4.4.9 Line width information

Two transitions sharing a common upper level J and symmetry have identical line widths and other signatures (e.g. hyperfine splitting, lifetime broadening). One method to check an assignment is to ensure that the transitions to the same upper state have similar line widths and profiles. This was found to be true for all assigned lines (vacuum wavenumber listings are given in A.1 and A.2). All assigned lines bar one were found to be singlet lines with no hyperfine splittings observed. The exception is transitions to the v′=2, J′=4 level. For this level, the P(5) and the R(3) lines are split by 9.98×10^{-3} and 9.99×10^{-3} (cm^{-1}) respectively [the Q(4) line is not split due to the different symmetry ('f') of the upper state]. The three observed transitions to this state are given in Figure 4.12. The R(3) line for the v′=4 state had a poorer signal-to-noise ratio than the v″=3. The P(5) line is almost certainly

v′ \ v″	0	1	2	3	4
0	23320 *23320*	21371 *21371*	19488 *19488*	**17673.62** **17671.32**	15921 *15921*
1	23702 *23703*	21753 *21754*	19870 *19872*	**18055.73** **18054.50**	16303 *16305*
2	24043 *24045*	22094 *22096*	20212 *20213*	**18397.65** **18395.86**	**16644.78** *16646*

Table 4.4 Deslandres table of the band origins (cm^{-1}) of the $^1\Pi$-$^1\Sigma^+$ system of $^{70}GeH^+$(italicised) and $^{74}GeH^+$. Assigned observed bands are shown in bold. Other bands are calculated from molecular parameters from the recalculated parameters given in Table 4.3 and the emission study [87].

embedded in the background signal. When predicted singlet lines take on triplet characteristics (such as hyperfine splittings) this can be attributed to the mixing of the wavefunction for the singlet state with that of a wavefunction of a triplet state [95]. This is clearly the case for these lines (which have 'e' symmetry, J′=4, v′=2), although the same is not true for the Q(4) lines (see Figure 4.13). All three lines almost certainly involve the same upper state, due to the relative intensities and spacing of the components and matched line widths. These spectra represent a rare example of 'multichannel character' in the spectrum of GeH^+.

The line width (and hence lifetime) of rotational levels in a vibrational band of the $^1\Pi$ state can be seen (see Figures 4.14 - 4.19) to vary over two orders of magnitude with J (and increasing energy). Lines follow the same general pattern for all three of the upper vibrational states: The lines involving lowest J in the band have widths $>0.1 cm^{-1}$; upon increasing J, a decrease in width is observed. This continues until the line width reaches a minimum value (at the limit of experimental detection), followed by rapid increase to $>0.3\ cm^{-1}$. This occurs for both the v′=1 and v′=2 levels. For the v′=0, the high J lines are too weak to detect, but higher lying rotational states almost certainly exhibit a further increase.

The line widths for all vibrational states, for the $^{74}GeH^+$ and $^{70}GeH^+$ isotopes are plotted in Figures 4.14 - 4.19 . It can be seen that the widths of low J lines (which generally have a large FWHM and small intensity) have deviations between P and R transitions arriving at the same upper state.

Gnd. State Difference	**v′=0**	**v′=1**	**v′=2**
R(1)-P(3)	62.0315	-	62.0936
R(2)-P(4)	86.8195	-	86.8191
R(3)-P(5)	111.509	-	111.5631
R(4)-P(6)	136.2025	-	136.2067
R(5)-P(7)	160.7901	-	160.7939
⋮			
R(9)-P(11)	258.0169	258.0048	-
R(10)-P(12)	281.9671	281.9786	-
R(11)-P(13)	305.7762	305.7687	-
R(12)-P(14)	329.3729	329.3865	-
R(13)-P(15)	352.8305	352.80	-

Table 4.5 Ground state level separations for the v″=3, $^1\Sigma^+$ state of $^{74}GeH^+$ determined from the (0,3), (1,3) and (2,3) bands.

This is due to the uncertainty associated in measuring the line width. Low signal-to-noise ratios (down to 1:1 in $^{70}GeH^+$) make measurement of broad lines difficult as discrimination between background fluctuations and line intensity has to be made. Many of these lines were scanned with long time constants (and correspondingly longer scan times) to overcome this problem, although this proved difficult due to fluctuations in beam strength, magnet current and laser intensity. At intermediate J values (where line width decreases and line intensity increases), all three branches have consistent line widths. The behaviour of the Q branch line widths was unexpected: Q-type resonances access levels with symmetry 'f'. The different 'parity' blocks couple to separate electronic states and have continuum wavefunctions with inherently different structures [96]. This can produce different line widths and profiles for the different 'parity' blocks (as found to a certain extent in CH^+ [97] and SiH^+ [52]. For the 'e' and 'f' symmetries of the $^1\Pi$ state, the lifetime difference is negligible and line widths are consistent within experimental uncertainties.

The variation of line width with rotational quantum number has been stud-

ied for many molecules, lifetime information about the states calculated and the dissociation mechanism deduced. In some cases the point of crossing between two curves can be calculated or other predissociating states and mechanisms inferred. For examples see: [66],[98],[99].

In the case of GeH^+ there are three possibilities for predissociation of the $^1\Pi$ state: A curve crossing, an avoided crossing or barrier, or predissociation due to the $^1\Pi$ levels lying embedded in the continuum of states correlating to a lower asymptote (Feshbach resonances). The most likely candidate for a curve crossing of the $^1\Pi$ state is the $^3\Sigma$ state. However, all components of this state correlate with the $^2P_{\frac{3}{2}}$ (upper) asymptote (for example see [96]). Predissociation for the $a^1\Pi$-$X^1\Sigma^+$ transition in GeH^+ , must occur in the 'window' that lies between the spin-orbit split atomic limits; the molecule must dissociate above the $Ge^+(^2P_{\frac{1}{2}}) + H(^2S_{\frac{1}{2}})$ limit for a fragment to be observed, and must lie below the $Ge^+(^2P_{\frac{3}{2}}) + H(^2S_{\frac{1}{2}})$ limit as predissociation must occur and therefore the upper state must be quasibound. For predissociation of many levels of the $^1\Pi$ state to occur it is essential that the crossing curve correlates to a lower asymptote, therefore predissociation *via* this route seems unlikely as both states correlate to the same lower asymptote.

However, the *ab-initio* work predicts the $^3\Sigma$ state to have a long range minimum [89] and an unknown dissociation energy. In CH^+, the $^3\Sigma$ state is found to have a minimum at 6 Å and a depth of ≈ 300 cm^{-1} [96]. If the $^3\Sigma$ surface crosses the $^1\Pi$ state in approximately this region, rapid line width variation with rotational quantum number could occur. However the $^3\Sigma$ state must then further couple with the states or a continuum of states correlating to the lower dissociation asymptote ($Ge^+(^2P_{\frac{1}{2}}) + H(^2S_{\frac{1}{2}})$) for predissociation to occur.

The second possibility is that a barrier exists on the $^1\Pi$ surface of GeH^+, and that all states observed in this experiment are quasibound with respect to the $Ge^+(^2P_{\frac{3}{2}}) + H(^2S_{\frac{1}{2}})$ asymptote. Quantum mechanical tunnelling through the barrier would then yield the observed transitions. This is directly analogous to the $^1\Pi$-$^1\Sigma^+$ system of GaH as studied in absorption by Kronek et al. [76], where all transitions to the $^1\Pi$ state were found to be diffuse, due to the short lifetimes associated with these states.

Coupling between bound levels of the $^1\Pi$ state and the continuum of states for the $^1\Sigma^+$ and triplet states (correlating to the $Ge^+(^2P_{\frac{1}{2}}) + H(^2S_{\frac{1}{2}})$) allows a molecule to dissociate along the $Ge^+(^2P_{\frac{1}{2}}) + H(^2S_{\frac{1}{2}})$ asymptote. This is known to be the principle dissociation mechanism for the isovalent SiH^+ [52] and the $A^2\Pi_{\frac{1}{2}}$ state of $HeNe^+$ [53].

To differentiate between these possibilities for the dissociation mechanism of GeH^+, energy releases were recorded for all possible assigned spectroscopic transitions. A large center-of-mass excess energy for the assigned transitions would be associated with dissociation to the lower dissociation asymptote whereas a small excess energy would indicate dissociation to the upper fine structure limit.

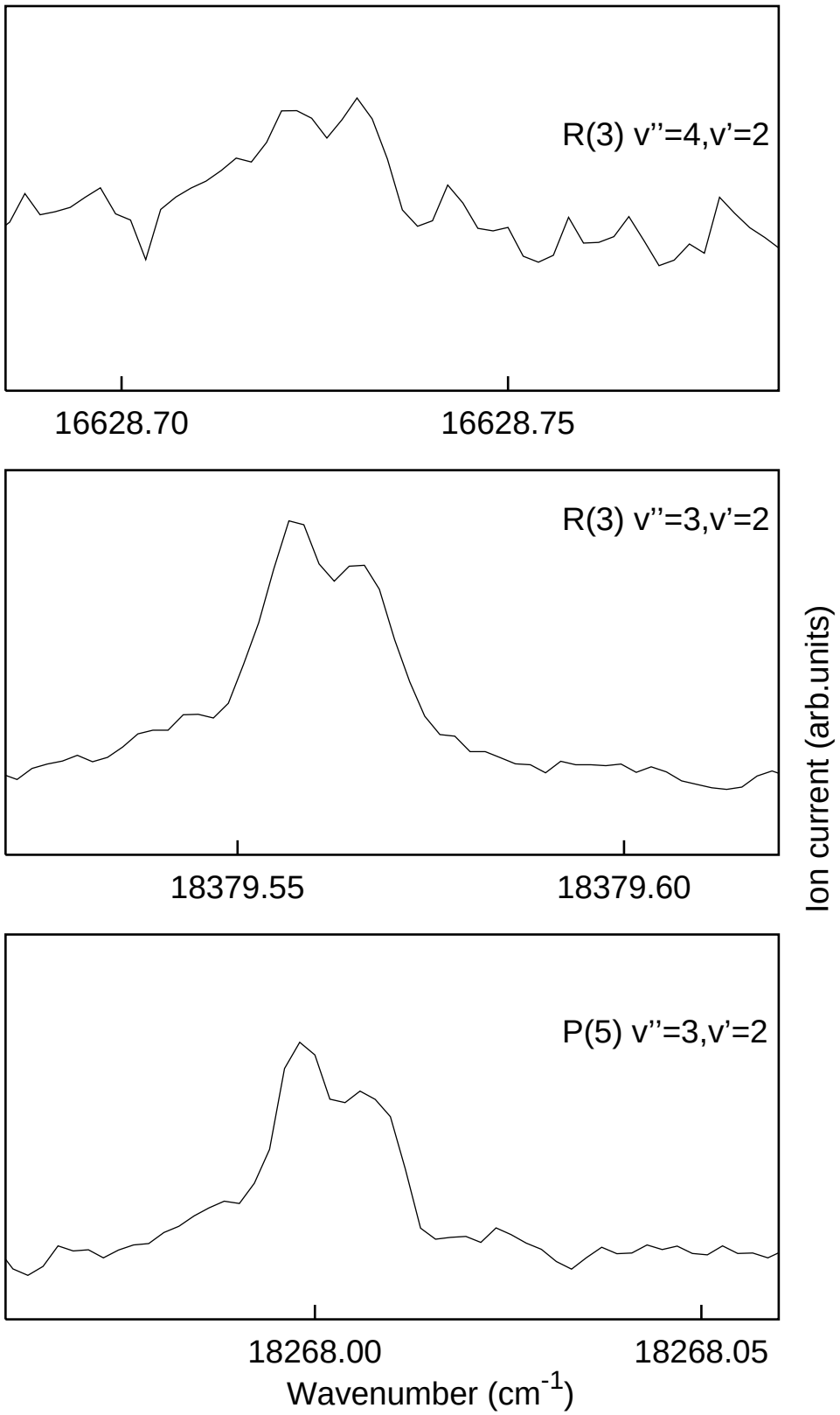

Figure 4.12 Observed lines corresponding to transitions for v′=2, J′=4 from indicated lower states. Abscissa have equal wavenumber ranges for direct comparison. The R(3) [2,4] line is included for direct comparison with R(3) [2,3].

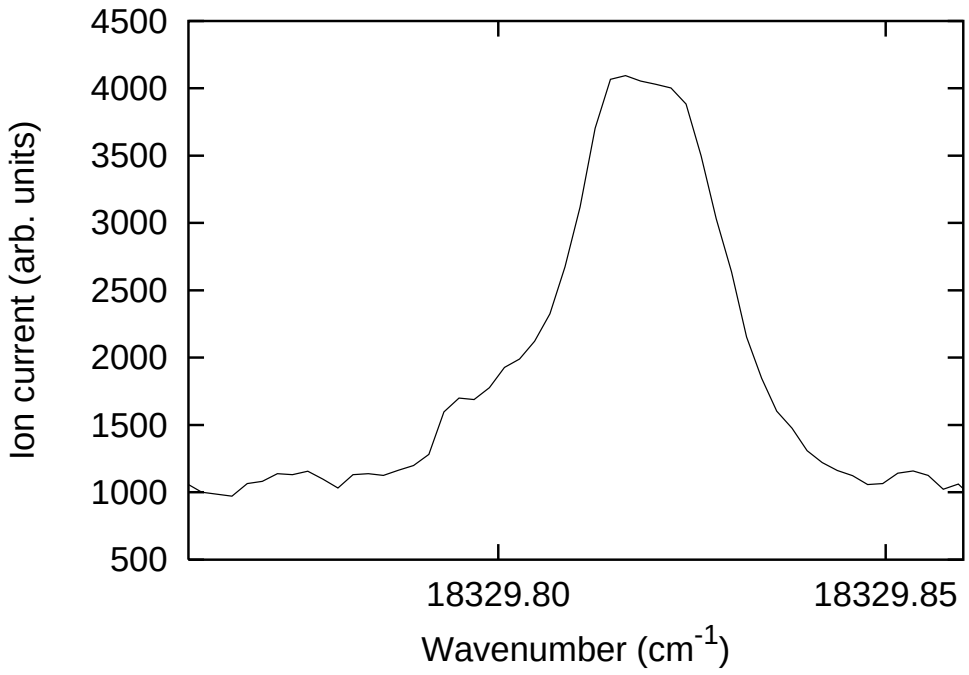

Figure 4.13 Q(4) line corresponding to transition for v′=2, J′=4 from v″=3. Abscissa has equal wavenumber range for direct comparison with Figure 4.12. No splitting is observed due to the symmetry of the upper state.

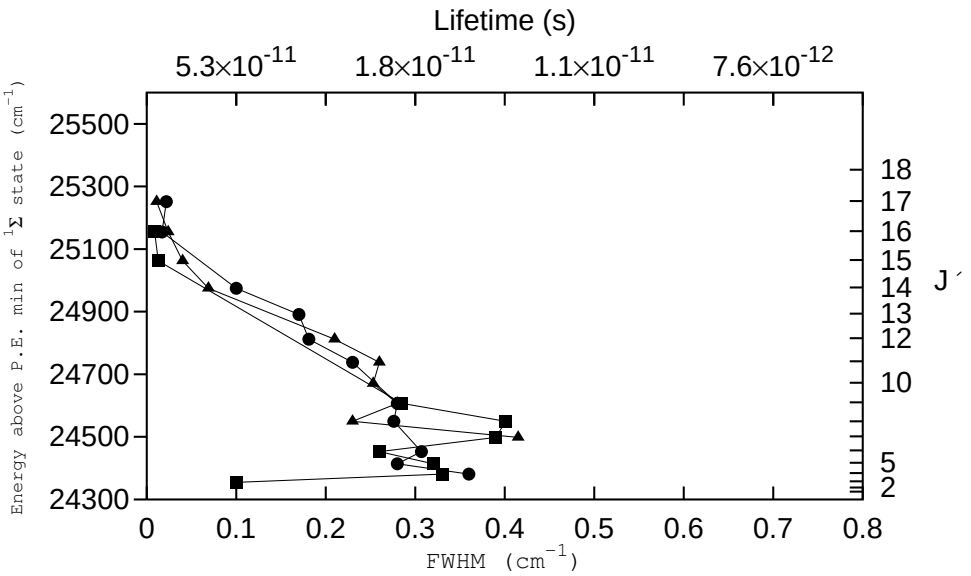

Figure 4.14 Line widths of the rotational levels of the (v=0) $A^1\Pi$ state of $^{70}GeH^+$. P, Q and R transitions are indicated with ■, ● and ▲ respectively.

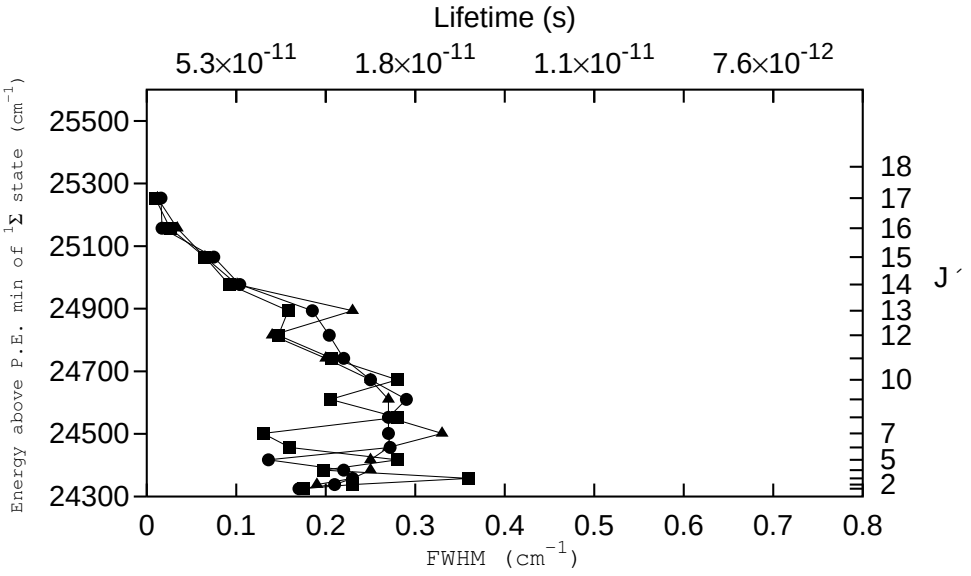

Figure 4.15 Line widths of the rotational levels of the (v=0) $A^1\Pi$ state of $^{74}GeH^+$. P, Q and R transitions are indicated with ■, ● and ▲ respectively.

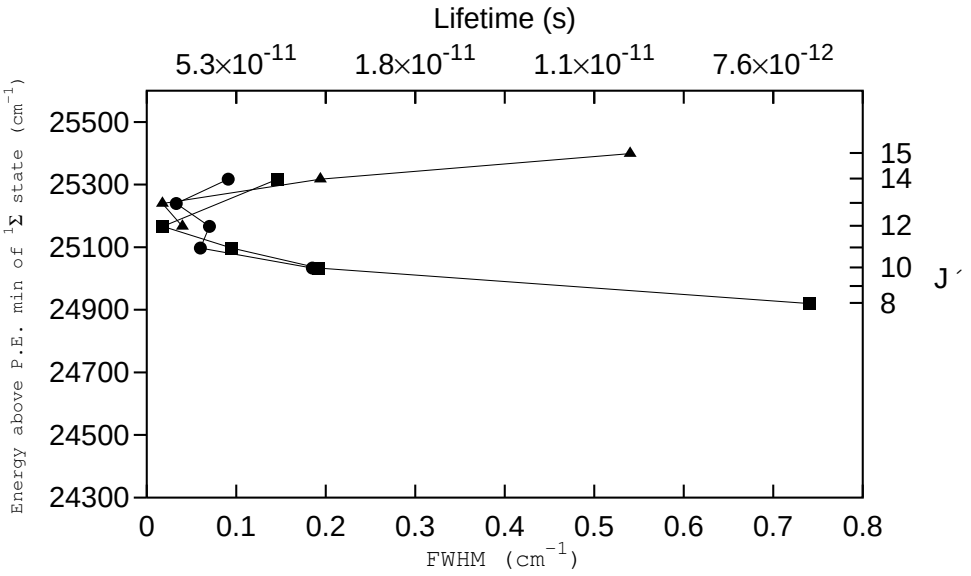

Figure 4.16 Line widths of the rotational levels of the (v=1) $A^1\Pi$ state of $^{70}GeH^+$. P, Q and R transitions are indicated with ■, ● and ▲ respectively.

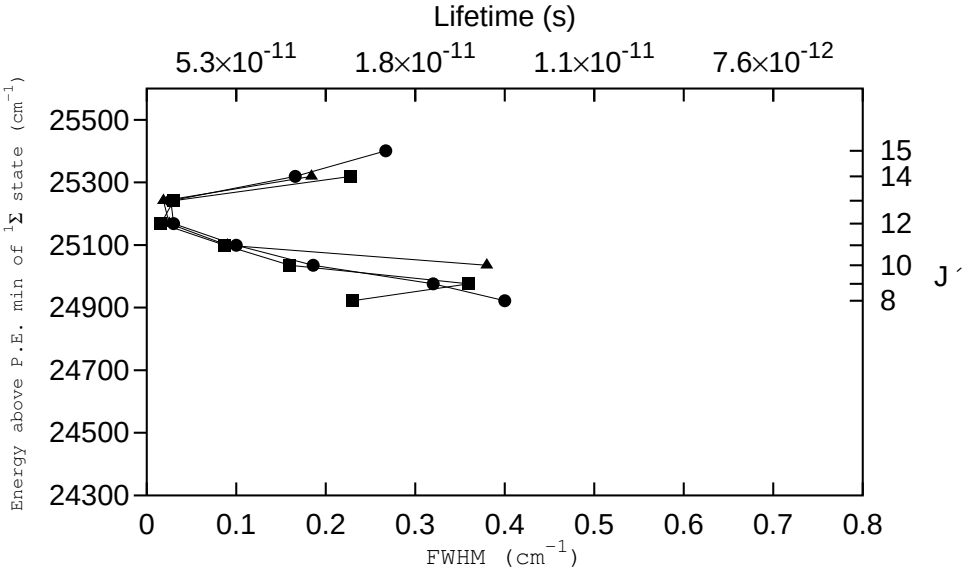

Figure 4.17 Line widths of the rotational levels of the (v=1) $A^1\Pi$ state of $^{74}GeH^+$. P, Q and R transitions are indicated with ■, ● and ▲ respectively.

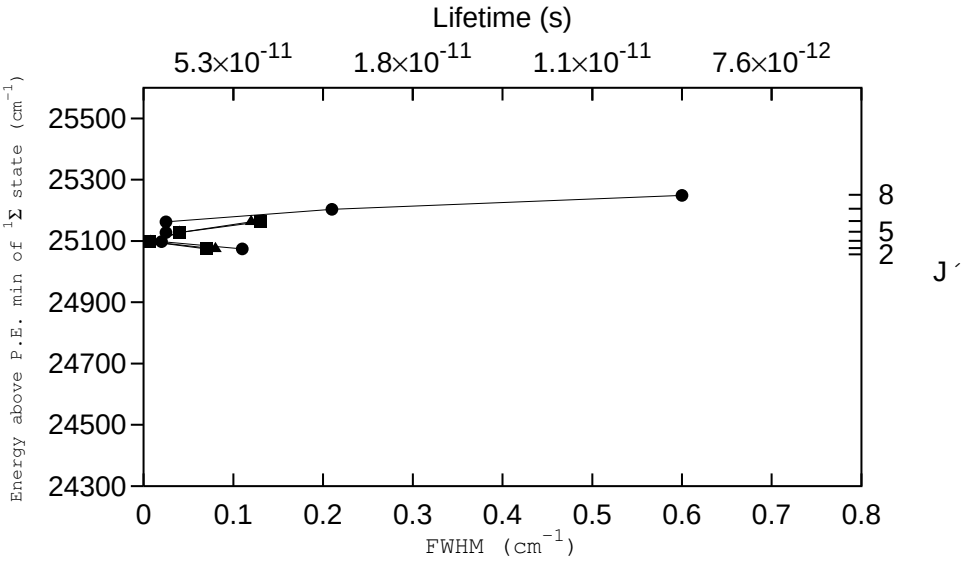

Figure 4.18 Line widths of the rotational levels of the (v=2) $A^1\Pi$ state of $^{70}GeH^+$. P, Q and R transitions are indicated with ■, ● and ▲ respectively.

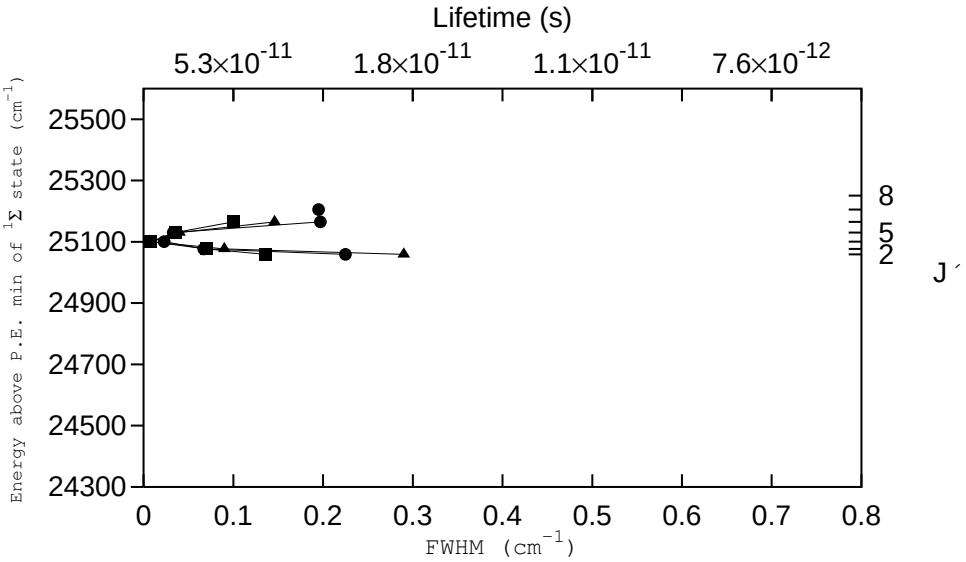

Figure 4.19 Line widths of the rotational levels of the (v=2) $A^1\Pi$ state of $^{74}GeH^+$. P, Q and R transitions are indicated with ■, ● and ▲ respectively.

4.4.10 Centre-of-mass Kinetic Energy releases

Energy releases were recorded for fourteen $^1\Pi$-$^1\Sigma^+$ transitions of $^{70}GeH^+$, as well as several intense unassigned lines, some of which exhibit splittings consistent with those found in proton hyperfine splittings. Attempts to record a greater number of lines proved fruitless due to the need for narrow slits in the second magnetic sector and the low ion current associated with the $^{70}GeH^+$ isotope (parent ion) (See Figure 4.2). Increasing the separation of the slits would have increased the number of potentially obtainable energy releases, but would have decreased the resolution of the magnetic sector to an unacceptable level.

Three examples of energy release profiles are given in Figure 4.20. All the profiles shown involve transitions to the J′=12, v′=1 state. The apparent width of the Q(12) line is greater, and the P(13) and R(11) lines have similar widths. The P(13) and R(11) lines have profiles which appear to be made up of one component, while the Q(12) lines has a local minimum in the center of the profile. The apparently greater width for a Q transition energy release has been observed in previous studies in the ion beam apparatus, [100] and is attributable to a different instrumental response between parallel and perpendicular transitions when using a vertical slit arrangement [101].

4.4.11 Modeling the Energy releases

Due to the different responses for parallel and perpendicular transitions, it was decided to model the energy releases using the equations for the laboratory frame energy release, convolute this with the instrumental profile, and convert to a momentum scale. The equation used to calculate the profiles of the energy releases uses the laboratory energy taken from the study by Huber et al. [102]:

$$E_1 = \frac{m_1 m_2}{m_1 + m_2}\left(\frac{E_0}{m_2} + 2\left(\frac{E_0 W}{m_1 m_2}\right)^{\frac{1}{2}}\cos(\phi) + \frac{W}{m_1}\right) \tag{4.11}$$

where m_1 and m_2 are the masses of the Ge^+ and H fragments respectively
E_0 is the initial kinetic energy of the parent molecule ($=qV_{accn}$)
W is the centre of mass kinetic energy release
ϕ is the angle of fragment ejection with respect to the ion beam direction.

The probability of a fragment being ejected at an angle ϕ' is given by:

$$P(\phi') = \frac{1}{4\pi}[1 + \beta P_2 \cos(\phi')] \tag{4.12}$$

where

$$P_2\cos(\phi') = \frac{1}{2}[3\cos^2(\phi') - 1] \tag{4.13}$$

β depends on the symmetry of the transition. For the case of strongly predissociated level it can be approximated to +0.5 for P and R transitions and -0.25 for a Q transition [103].

The laboratory energy releases were calculated using equations 4.11-4.13, converted to a energy release and then convolved with the intrinsic experimental profile. The instrumental profile was recorded using the ion beam apparatus to mimic the response to daughter ions. Scan conditions were set which were identical to those used in the energy release experiments, (slit width, magnet current and scan length and speed). The transmittance of a $^{70}GeH^+$ parent ion beam through the apparatus was measured at the second electron multiplier, which was approximated to the instrumental response. Estimates for β, W and E_0 were made, to give a predicted profile for comparison with the experimental profile.
A series of programs based on *amoeba* [104] were used to fit the experimental and predicted profiles. This program varied the parameters W, E_0 and (optionally) β to achieve a best fit to the experimental data. The data from fixed β fit is given in Table 4.6.

Due to the low signal-to-noise ratio for many of the energy releases, accurate modelling of the energy release was difficult, therefore β was generally fixed. However, the releases with high signal-to-noise could be modelled with β floating (see Table 4.7). The β parameter for P and R transitions of $^{70}GeH^+$with the best signal to noise ratio is between +0.5-0.57, suggesting that the P(11),P(13),R(11) and R(12) are parallel transitions. Therefore these lines are correctly assigned, suggesting that all P and R transitions are assigned correctly.

The Q transitions had generally poorer signal to noise than the P and R transitions and exhibited large variations in their β values. The fit to the Q branches was poor, with a χ^2 squared value generally an order of magnitude greater than those for the P and R transitions.

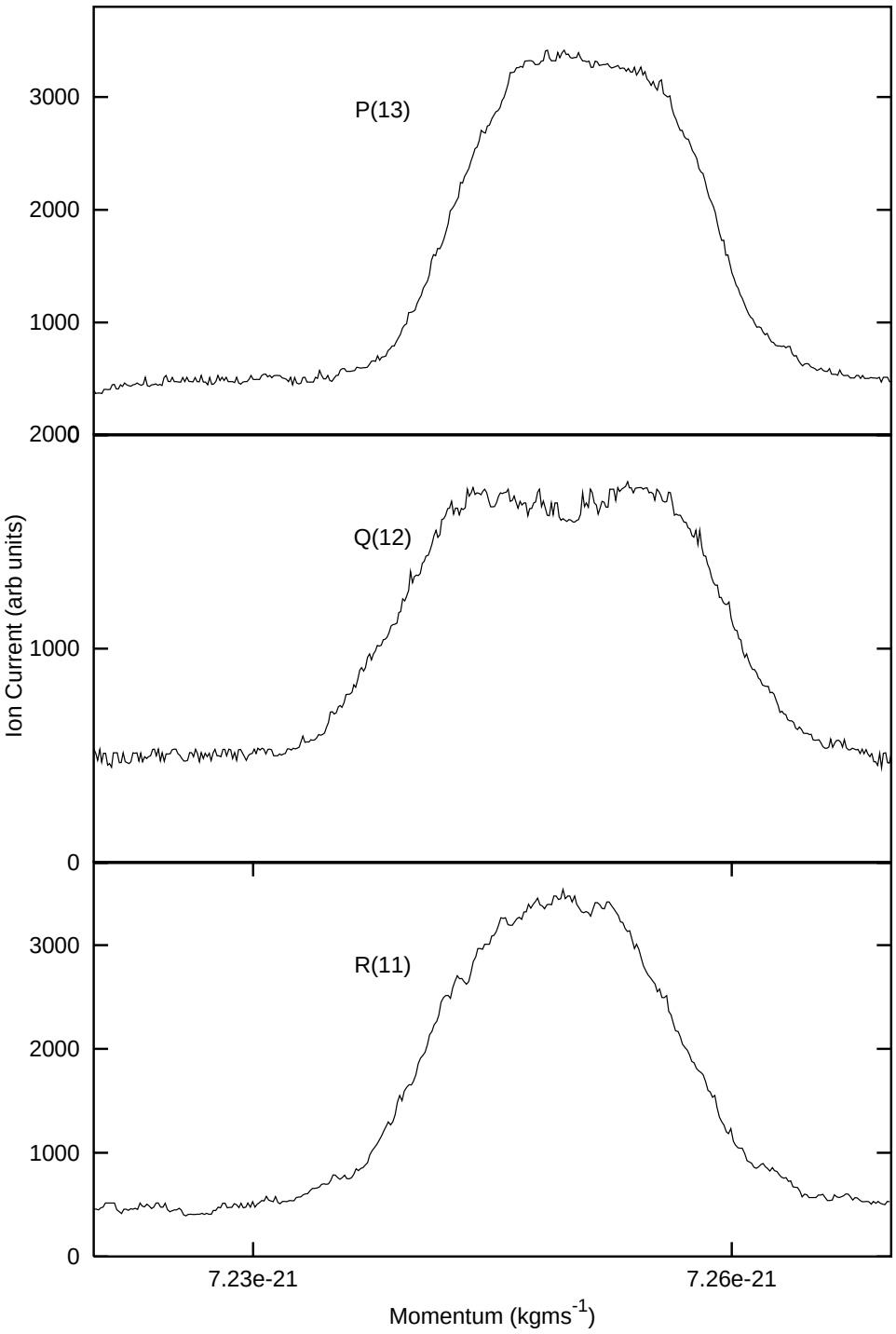

Figure 4.20 Kinetic energy releases for transitions to J′=12, v′=1 of the $^1\Pi$ state of $^{70}GeH^+$. The x abscissa is in momentum units as the scan was carried out using the second magnetic sector (momentum analyser).

$\mathbf{v'}$	$\mathbf{J'}$	Line	$\mathbf{W(cm^{-1})}$	Line	$\mathbf{W(cm^{-1})}$	Line	$\mathbf{W(cm^{-1})}$
1	10	P(11)	963				
1	11	P(12)	1061	Q(11)	1295		
1	12	P(13)	1124	Q(12)	1464	R(11)	1143
1	13			Q(13)	1369	R(12)	1117
1	14			Q(14)	949	R(13)	963
2	3			Q(3)	1071		
2	4			Q(4)	1023	R(3)	1048
2	5			Q(5)	1267	R(4)	1040

Table 4.6 Molecular frame energy releases (W) for all possible lines of $^{70}GeH^+$. Q lines were fitted with β=-0.25, P and R lines fitted with β=+0.5.

$\mathbf{v'}$	$\mathbf{J'}$	Line	β	$\mathbf{W(cm^{-1})}$	Line	β	$\mathbf{W(cm^{-1})}$
1	10	P(11)	+0.57	843			
1	12	P(13)	+0.55	1003	R(11)	+0.50	1136
1	13				R(12)	+0.57	1152

Table 4.7 Centre-of-mass energy releases (W) for $^{70}GeH^+$. β is floated as a free parameter. Only lines with a χ^2 fit of less than 40 are included.

4.4.12 Analysis of fitted releases

Comparison between experimental and calculated energy releases can be made using knowledge about the ground state dissociation energy, the photon energy and Equation 4.14. Results obtained are given in Table 4.8. All transitions to rotational levels with J up to 13, (v′=1) (of both 'e' and 'f'

type symmetries) are seen to fit to a mean dissociation energy of 24,060 ± 14 cm^{-1}.

$$D_e = h\nu + E_{v'',J''} - T \tag{4.14}$$

where D_e is the dissociation energy, $E_{v'',J''}$ is the ground state energy, $h\nu$ is the photon energy and T is the energy release. To a first approximation, the spectroscopy of GeH^+ is similar to that of SiH^+ (i.e. the predissociation spectrum is dominated by Feshbach resonances) and the overwhelming majority of transitions dissociate along the lowest dissociation asymptote. Hence a mean value of 24,060 ±14 cm^{-1} for the $Ge^+(^2P_{\frac{1}{2}}) + H(^2S_{\frac{1}{2}})$ dissociation limit is obtained. From Moore's tables [105], it is known that the $Ge^+(^2P_{\frac{3}{2}}) + H(^2S_{\frac{1}{2}})$ and the $Ge^+(^2P_{\frac{1}{2}}) + H(^2S_{\frac{1}{2}})$ are split by the atomic spin-orbit splitting of 1,767.3 cm^{-1}. The higher lying asymptote must therefore lie at 25,827 cm^{-1}.

However, the possibility exists that all transitions lead to dissociation along the upper asymptote (as in GaH [75]). It follows that the upper asymptote must lie at 24,060 ±14 cm^{-1} with respect to the potential energy minimum of the $^1\Sigma^+$ state). For this to be the case, the lower asymptote $(Ge^+(^2P_{\frac{1}{2}}) + H(^2S_{\frac{1}{2}}))$ would have to lie at 22,293 cm^{-1}. For the construction of potential energy curves for the $^1\Pi$ and $^1\Sigma^+$ states, it is necessary to consider the possibility of the transitions leading to fragmentation along different (spin-orbit split) atomic limits, as described in the following sections.

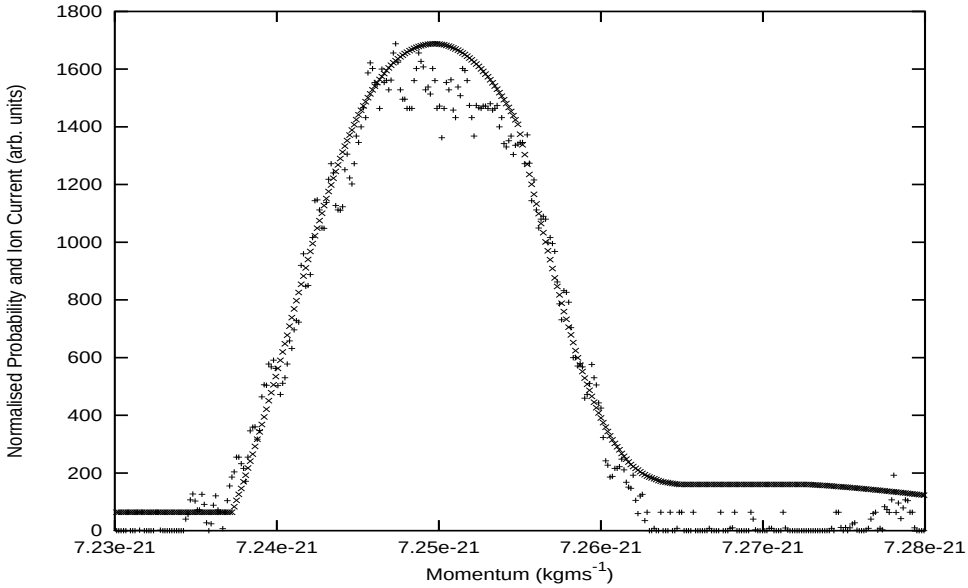

Figure 4.21 Fitted momentum release for J′=11(f), v′=1 of the $^1\Pi$ state of $^{70}GeH^+$(× and + correspond to model and recorded data respectively).

Line (cm^{-1})	**v′**	**J′(parity)**	**Expt.(cm^{-1})**	**Calc. cm^{-1}**
17567.9081	1	10(e)	963	973
17484.7117	1	11(e)	1061	1036
17630.7890	1	11(f)	1295	1036
17394.5920	1	12(e)	1124	1105
17700.6046	1	12(e)	1143	1105
17552.3319	1	12(f)	1464	1104
17627.1202	1	13(e)	1117	1179
17366.8493	1	13(f)	1369	1177
17546.4077	1	14(e)	963	1257
17374.0944	1	14(f)	949	1255
18354.0207	2	3(f)	1071	1019
18377.7180	2	4(e)	1048	1042
18327.944	2	4(f)	1023	1042
18357.1914	2	5(e)	1040	1071
18295.0117	2	5(f)	1267	1071

Table 4.8 Comparison between calculated and experimental energy releases, assuming that all assigned transitions correspond to GeH^+ dissociating along the $Ge^+(^2P_{\frac{1}{2}}) + H(^2S_{\frac{1}{2}})$ asymptote at 24060 cm^{-1}

4.5 Analysis and Discussion

4.5.1 Dissociation between the fine structure limits (Feshbach resonances)

Using the kinetic energy release data, dissociation energies of 24,060 and 25,827 ± 14 cm^{-1} have been calculated for the $^1\Sigma^+$ and $^1\Pi$ electronic states. This complements the *ab-initio* study, showing close agreement (<2%) with the previously published dissociation energy of 23,793 cm^{-1} [89]. All observed transitions had relatively large kinetic energy releases ($\approx$ 1000 cm^{-1}), suggesting that the majority of transitions predissociated along the lower $(Ge^+(^2P_{\frac{1}{2}}) + H(^2S_{\frac{1}{2}}))$ asymptote. Therefore, predissociation for these levels (in the absence of a curve crossing) may be described in scattering terminology as Feshbach resonances. This occurs when bound levels of the $^1\Pi$ state couple with the continua of states correlating to the lower asymptote, leading to dissociation of GeH^+ into $Ge^+(^2P_{\frac{1}{2}}) + H(^2S_{\frac{1}{2}})$.

The lifetime behaviour for GeH^+ is unusual, in that the spectrum appears to be well-behaved (non-perturbed), but exhibits a large variation in line width. Such lifetime behaviour is usually attributed to curve crossing of a bound state by a repulsive state, as in OH [106], OD [107] or IBr [98]. However this behaviour is normally observed simultaneously with large perturbations in line frequencies and this does not occur in GeH^+. Line width behaviour of this type has also been observed where no curve crossing takes place in one (possibly two) molecular ions:

Carrington and Softley [53] recorded and assigned a photo-predissociation spectrum of $HeNe^+$. In total 78 of the lines were assigned to electronic transitions between $(v' = 0, 1)$ $A_2\ ^2\Pi_{\frac{1}{2}} - (v'' = 7, 8)$ $X^2\Sigma$ states. The $A_2\ ^2\Pi$ state is split at long range by spin-orbit coupling, with the unobserved $A_1\ ^2\Pi_{\frac{3}{2}}$ lying between the $X^2\Sigma$ and $A_2\ ^2\Pi_{\frac{1}{2}}$ states and correlating to the same asymptote as the $X^2\Sigma$ state. Observed line widths for rotational levels of the v′=0 decreased with increasing J and then rapidly increased. For the case of the v′=1 state, the line width variation was erratic, but generally decreased with increasing J to a lower limit then increased.

No crossing (or avoiding crossing) of the A_2 state occurs, but for transitions to be observed in a photofragment spectrum levels of this state must be predissociated. The mechanism believed to be responsible is that bound levels of the A_2 state couple with the continua of the $X^2\Sigma$ and $A_1\ ^2\Pi_{\frac{3}{2}}$ states. This spectrum provided the first evidence for an electronic predissociation of a diatomic molecule in the absence of curve or avoided crossings. Energy release measurements were made for each transition, yielding results consistent with dissociation along the lower $He(^1S_0) + Ne^+(^2P_{\frac{3}{2}})$ asymptote.

Walmsley noted [100] that the predissociation of SiH^+ was analogous to that found in $HeNe^+$. Predissociated levels of SiH^+ in the fast ion beam spectra were attributed to coupling of the bound $^1\Pi$ states with the states correlating to the lower $Ge^+(^2P_{\frac{1}{2}}) + H(^2S_{\frac{1}{2}})$ dissociation asymptote [52]. Large variations in line width with rotational quantum number were observed; increases from 0.018 to 4.5 cm^{-1} were observed when J′ increases from 17 to 19.

The line width behaviour of both SiH^+ and $HeNe^+$ show remarkable similarities with the work outlined here for the $^1\Pi$ state of GeH^+.

4.5.2 Dissociation through a barrier

An alternative argument to predissociation via coupling between the bound levels of the $^1\Pi$ state with the continuum of states correlating to the $Ge^+(^2P_{\frac{1}{2}}) + H(^2S_{\frac{1}{2}})$ dissociation asymptote, is to consider that molecules in the $^1\Pi$ state can dissociate by quantum tunnelling through a barrier. For this argument to be feasible, two possibilities exist for the observed behaviour of the line width and energy releases. Firstly, a barrier arises from the introduction of a centrifugal term in the effective potential of the non-rotating molecule $U_0(R)$ to yield an effective potential, $U_{eff}(R)$ which may be written as:

$$U_{\text{eff}}(R) = U_0(R) + \left(\frac{\hbar^2}{2\mu R^2}[J[J+1] - \Omega^2]\right) \tag{4.15}$$

Solution of the Schrödinger equation for such a potential $U_{\text{eff}}(R)$, yields levels which lie above and below the dissociation limit of $U_0(R)$. Those which lie above are shape resonances. To link such a theory with the experimental results, the position of all dissociation asymptotes, with respect to the potential energy surfaces, must be considered. In the case of a barrier, all parent ions in the $^1\Pi$ state must fragment along the $Ge^+(^2P_{\frac{3}{2}}) + H(^2S_{\frac{1}{2}})$ dissociation asymptote (to which the $^1\Pi$ state correlates). Such a barrier would cause an increase in line width with every subsequent line in the rotational progression. This is clearly not the case the transitions to the $^1\Pi$ state for either isotope, as a general decrease in lifetime is observed for low J in all vibrational states.

Calculations were undertaken using the **LEVEL6.0** program to simulate such a barrier by lowering the dissociation asymptote to the value predicted assuming the energy release occurs along the $Ge^+(^2P_{\frac{3}{2}}) + H(^2S_{\frac{1}{2}})$ asymptote. It was found the v′=0, J′=1 states would be strongly bound having a lifetime of the order of 10^9 s, and therefore would not be seen in the time scale of this experiment. It seems unlikely that a rotational barrier plays a significant rôle in the dissociation of low J levels in the $^1\Pi$ state of GeH^+.

The second possibility for a barrier arises due to an avoided crossing, which is the case in the $^1\Pi$ state of the isoelectronic molecule GaH [76], where the absorption spectrum for v′=0 was observed to be diffuse due to the short lifetimes of rotational levels in the $^1\Pi$ state. No discernible rotational structure could be found in GaH, but was found for GaD. In contrast to this, the line widths observed in GeH^+ , are narrower, comparable to those found in CH^+ and SiH^+, where individual rotational lines can easily be observed, and the widths are generally <2 cm^{-1}.

Such a barrier arises from an avoided crossing between states of the same symmetry [74]. For GaH, the two lowest $^1\Pi$ states are separated by 33,000 cm^{-1} [75], whereas for GeH^+, the separation between these states is much larger (61,452 cm^{-1} [89]), which implies that a barrier due to an avoided crossing would be less likely and if present certainly lower than in GaH. This is entirely analogous to the case of the isoelectronic molecules AlH and SiH^+. AlH has a large barrier in the $^1\Pi$ state entirely due to an avoided crossing [108], it's two lowest $^1\Pi$ states separated by 32,400 cm^{-1} [105]. However, no such barrier has been detected in SiH^+, possibly because the separation of the $^1\Pi$ states is too large (50,000 cm^{-1} [109]). It seems likely, therefore, that no barrier due to an avoided crossing exists in GeH^+.

To quantify the argument of predissociation *via* tunnelling through a barrier (either centrifugal or avoided crossing), calculations using the **LEVEL6.0** program [90] were initiated, to investigate any link between energy releases and widths of the lines. The dissociation limit(s) were adjusted assuming that the parent molecule dissociates along the upper $(Ge^+(^2P_{\frac{3}{2}}) + H(^2S_{\frac{1}{2}}))$ asymptote. It was found, however, for the energy releases to be of the order 1000 cm^{-1}, all observable levels of the v′=2 state should have line widths greater than 5 cm^{-1}. This is clearly not the case for either recorded isotope (see Figures 4.19-4.18).

Due to the similarities in the line width behaviour of GeH^+ and $HeNe^+$, the lack of evidence for a barrier and the low likelihood of the $^1\Pi$ state being crossed by a repulsive state, the dissociation mechanism is almost certainly due to coupling between the bound $^1\Pi$ state and the continuum of states correlating to the lower $(Ge^+(^2P_{\frac{1}{2}}) + H(^2S_{\frac{1}{2}}))$ dissociation asymptote. Molecules existing in the $^1\Pi$ state of GeH^+ are therefore considered to dissociate to the lower $(Ge^+(^2P_{\frac{1}{2}}) + H(^2S_{\frac{1}{2}}))$ asymptote.

4.5.3 Potential curves constructed from spectroscopic data

After assigning the recorded lines to the (0,3),(1,3),(2,3) and (2,4) bands of the $^1\Pi$-$^1\Sigma^+$ transition, potential energy curves were constructed from the molecular parameters. Other parameters were calculated to include results from the *ab-initio* and emission studies for the $^1\Sigma^+$ state (see Table 4.3). A

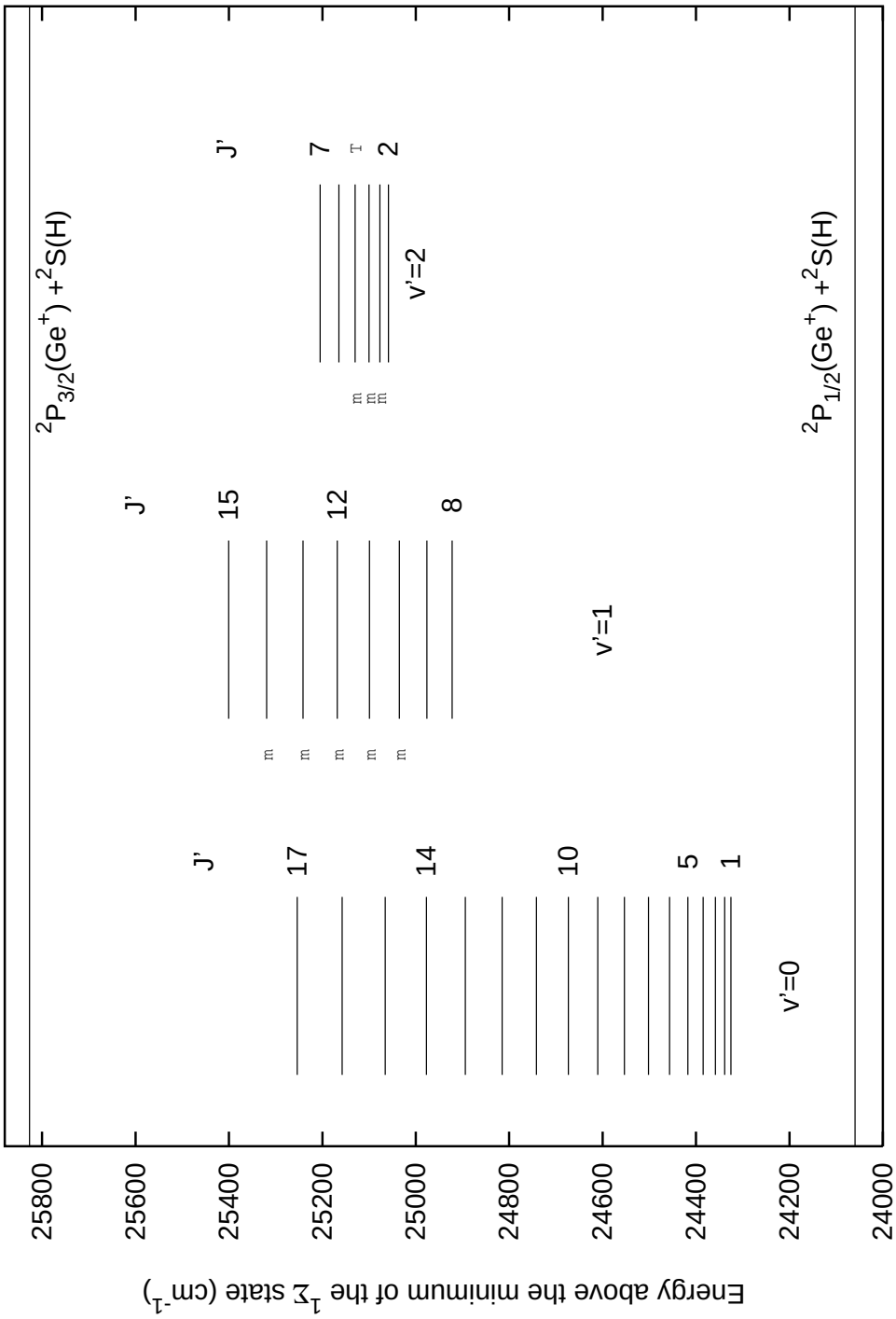

Figure 4.22 Energies of the assigned rotational states of the $^1\Pi$ state. Those lines recorded in energy release experiments are denoted by m. The $v'=2$, $J''=4$ state has been marked T as shows features consistent with proton hyperfine splitting in a triplet state.

defined $^1\Sigma^+$ state potential was constructed from the improved parameters, to provide information for further assignments and create the most accurate potential possible from all spectroscopic data. Potential energy curves for the four experimentally observed electronic states were constructed using the following methods:

- Molecular parameters from the fitting of absorption and emission spectra data were least squares fitted to yield the best values for the first two Dunham vibrational and rotational parameters for each state. The program **RKR1** [80] was used to calculate potentials from these data, together with B_v and G_v for these states.
- The Dissociation energies of the $^1\Sigma^+$ and $^3\Pi_1$ states were calculated to be 24,060 cm^{-1}, i.e. the asymptote along which the energy releases were observed to fragment. The $Ge^+(^2P_{\frac{3}{2}}) + H(^2S_{\frac{1}{2}})$ asymptote (which correlates to the $^1\Pi$ and $^3\Pi_{0^+}$ states) was calculated by adding the atomic spin-orbit splitting from Moore's tables [105].
- The separation between the $^1\Pi$-$^1\Sigma^+$ states was taken from the T_e value calculated from the predissociation data. Triplet state separations were taken from the work of Tsuji et al. [87].
- Modified potentials were constructed (See Figure 4.23) using the **LEVEL6.0** [90] program. The Schrödinger Equation was solved for the potentials giving levels for all v and J up to dissociation (and quasibound shape resonances). Transitions between the states were also calculated using **LEVEL6.0**. Frank-Condon factors and Einstein A coefficients were also obtained.

Potential energy curves generated using the above methods are displayed in Figure 4.23. Observed vibrational states from the predissociation spectrum are indicated by horizontal lines. Agreement between the four observed bands and bands predicted from the output of LeRoy's programs are reasonable. Figure 4.24 shows this comparison, the recorded line intensity is also plotted with the Einstein B coefficient, which show a relative increase in line intensities for the $v'=1$ band compared to the $v'=0$ band and a small decrease in intensity for the $v'=2$ band.

4.6 Unassigned lines

Despite the progress made in assigning a large number of lines to the $^1\Pi$-$^1\Sigma^+$ transition, there exist approximately 100 lines which remain unassigned. This section will discuss the origins and possible methods for assignment. The unassigned lines can be found in Tables D.1-D.3.

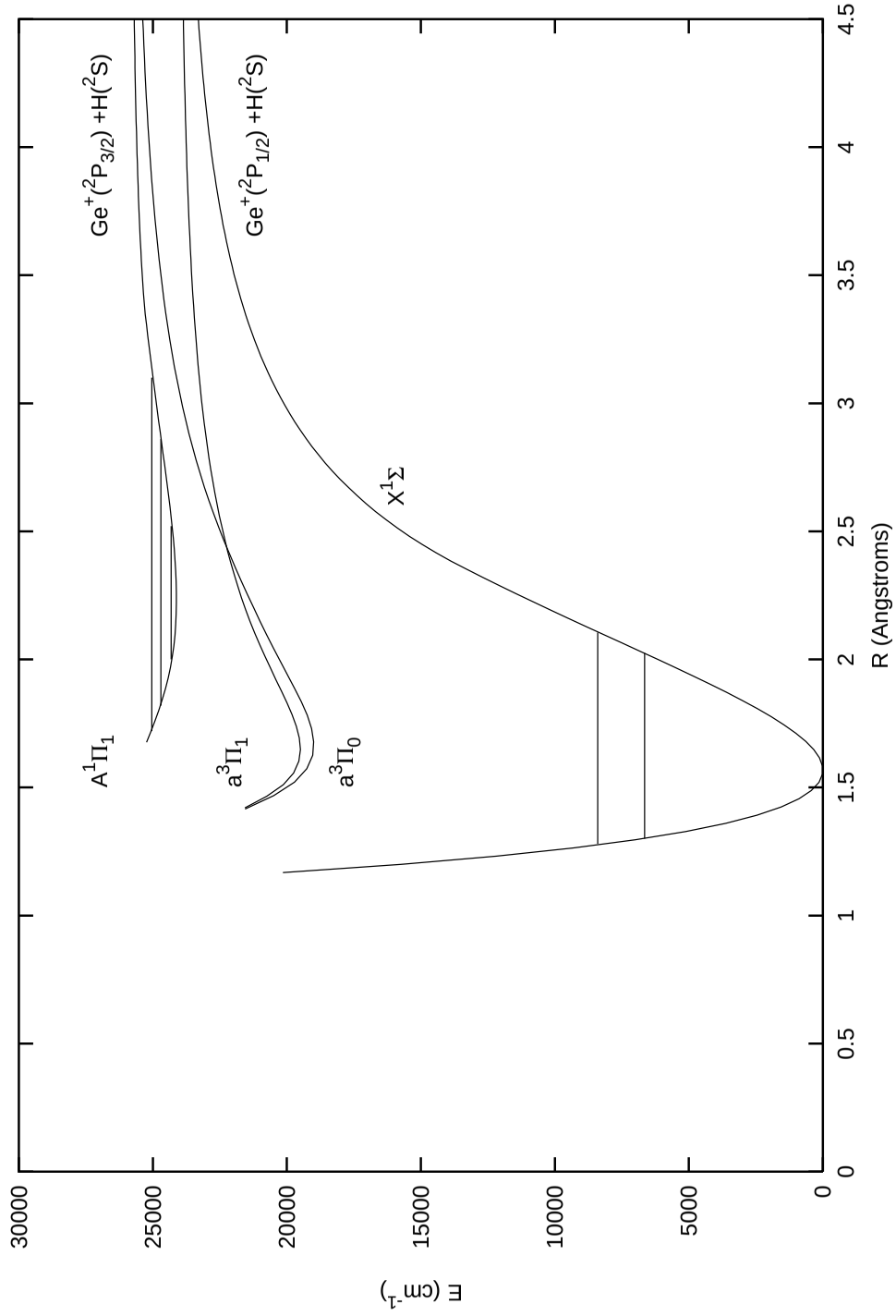

Figure 4.23 Potential energy curves of $^{70}GeH^{+}$. (Triplet states taken from study by Tsuji et. al. [87]), singlet states taken from this work.

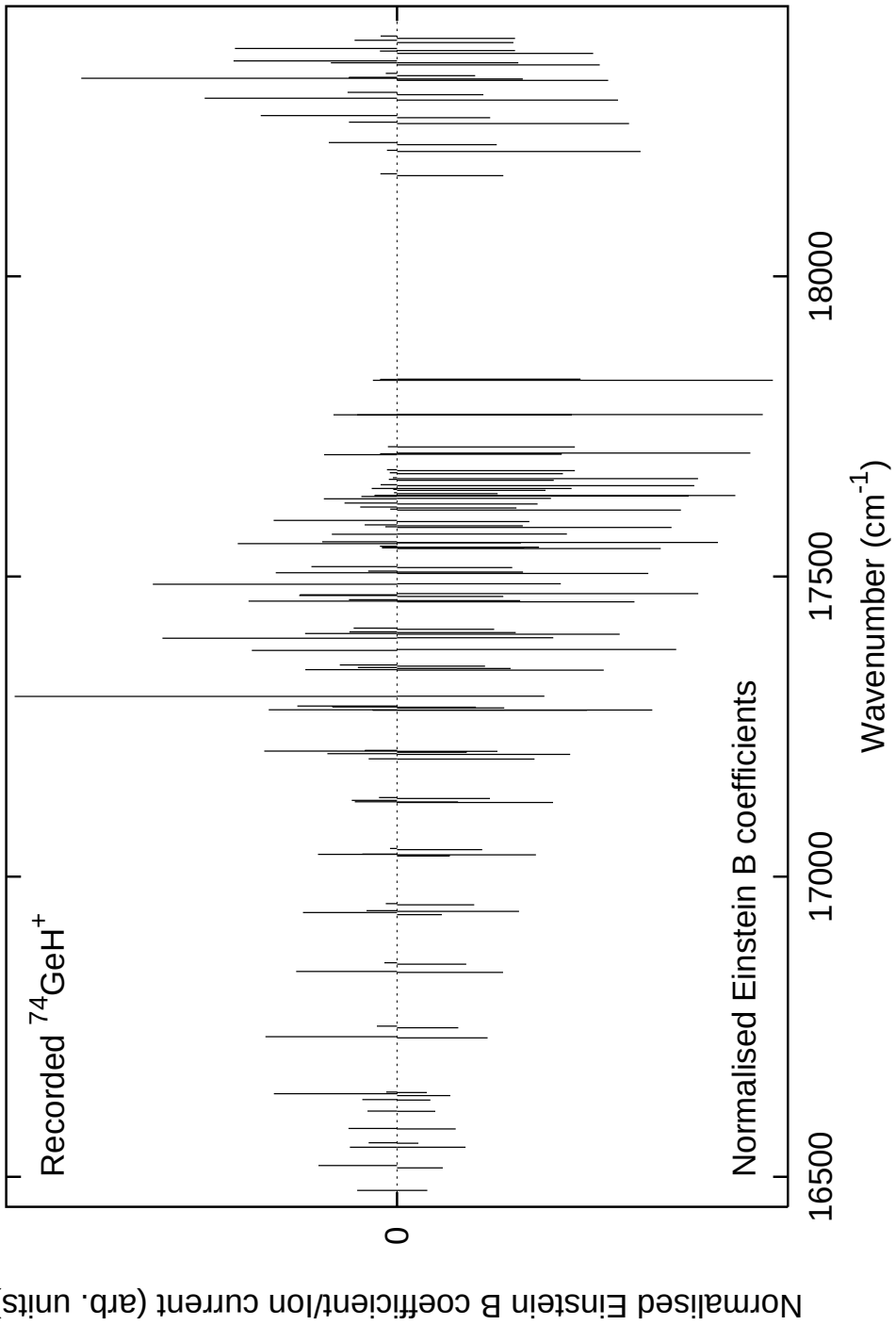

Figure 4.24 Comparison between the Einstein B coefficients (calculated from the LEVEL6.0 program by LeRoy) [plotted above the zero axis] and the assigned transitions of the predissociation spectrum [plotted below the zero axis]. Lambda doubling is neglected. No allowance is made for laser power or ion beam fluctuations.

Triplet lines

Approximately twenty of the lines exhibit splittings of < 0.01 cm^{-1} (300 MHz) which are associated with the hyperfine splitting term in the Hamiltonian:

$$H_{hf} = aI_zL_z + b_FI.S + \frac{c}{3}(3I_zS_z - I.S) - \frac{d}{2}(S_+I_+ + S_-I_-) \qquad (4.16)$$

For high J levels, the dominant term is the isotropic coupling interaction or Fermi interaction, $b_FI.S$, where the Fermi contact parameter b_F provides a measure of the electron spin density at the proton nucleus [52]. This is calculated to be 1420 MHz for an electron in a 1s orbital of a hydrogen atom. For a singlet state, such as $^1\Pi$, S=0 and hence splitting does not occur. In GeH^+, the H nucleus has a nuclear spin, I, of $\frac{1}{2}$. For a molecule in a pure $^3\Pi$ state arising from a s^1,p^1 configuration , only half of the total spin angular momentum contributes to the spin density at the proton nucleus. Thus the observed splitting should be less than 710 MHz. This is found to be the case for all observed doublets. Progressions in the hyperfine split lines could not be found, however they cluster around 16,500, at 17,600 and 18,300 cm^{-1} . They arise due to 'intensity stealing' from $^1\Pi$-$^1\Sigma^+$ transitions, verified by correlation of the strongest singlet-singlet transition frequencies with those of the hyperfine split lines.

Other lines

If a line exists in isolation a thorough search can be made for all lines which access the same upper state (using the method of ground state differences outlined earlier). However this method is only valid at low J, where the rotational energy levels are well defined by the known parameters B and D. As the assigned spectra generally lie between J=1-20, it is not possible to extrapolate to higher J.
The isotope shifts for many of the unassigned lines are irregular, and no further patterns could be found from the lines. However, the $^{70}GeH^+$ isotope was scanned in regions of interest only. A thorough investigation of $^{70}GeH^+$and possibly $^{72}GeH^+$, with continuous scanning could prove valuable in assigning the remaining transitions.

4.7 Conclusions

The first isotopically resolved spectra for GeH^+ have been recorded, with many absorption features found. Many of the recorded lines have been assigned to the allowed $^1\Pi$-$^1\Sigma^+$ transition of GeH^+, the first observation of this electronic transition in this molecule . Kinetic energy releases have verified the assignment, and provided the most accurate information to date

on the relative positions of the potential surfaces to the dissociation asymptotes. Dissociation of GeH^+ has been postulated to occur through coupling of the bound $^1\Pi$ state with the continuum of states correlating to the $Ge^+(^2P_{\frac{1}{2}}) + H(^2S_{\frac{1}{2}})$ asymptote, due to unusual lifetime behaviour and studies of energy release data. This has shown to be consistent with studies of similar molecules.

Chapter 5 Design and construction of a new ion source

5.1 Introduction

This Chapter discusses the design and implementation of a new ion source, created to study new species and to probe predissociated states of molecular ions other than those found using conventional electron impact ion sources.

A steady-state continuous cooled molecular beam is ionised, skimmed and focussed into an ion beam. A source was designed for this purpose and for ease of attachment to the existing ion-beam vacuum apparatus, with the minimum disruption or modification. The experimental principles are similar to those outlined in Chapter 2: a collimated ion beam is formed, parent species mass selected and fragmented with collinear laser radiation. Fragments are separated from the parent ions using a second electromagnet and detected at an electron multiplier.

5.2 Jet cooling of ion beams

5.2.1 Overview

Cooled molecular beams are created upon adiabatic expansion of high pressure gas through a nozzle into a low pressure background. Upon supersonic expansion, random motion of a static gas is converted into directed mass flow in the expanding jet. If the system is isentropic during expansion, then the temperature of the gas is reduced. A skimmer is positioned in front of the expansion to extract the centre of the beam (from the 'zone of silence' where the gas speed is greater than the local speed of sound) and avoid shock waves which inevitably occur during supersonic expansion.

5.2.2 Background

A given gas behind a nozzle has a relatively small velocity, called the *stagnation state* with a pressure and temperature, P_0 and T_0 respectively. The region into which the gas will expand has a pressure of P_b. The difference between the nozzle and background pressure causes gas to expand from the nozzle region. The molecules may reach speeds greater than the speed of sound in the region directly in front of the nozzle. At a given distance from the nozzle (the Mach disk), the gas will reach sub-sonic speeds and shock waves result between the supersonic and subsonic flowing gas. The distance (x_M) of the Mach disk from the nozzle aperture (of diameter D) can be

approximated by Equation 5.1.

$$\left(\frac{x_M}{D}\right) = 0.67\left(\frac{P_0}{P_b}\right)^{\frac{1}{2}} \tag{5.1}$$

To minimise collisions in the beam and avoid re-heating, the skimmer has to lie inside this disk. The temperature of the gas upon expansion is given in Equation 5.2

$$\frac{T}{T_0} = \left(1 + \left(\frac{\gamma - 1}{2}\right)M^2\right)^{-1} \tag{5.2}$$

where M is the Mach number (Equation 5.3) and γ is the ratio of the heat capacities.

$$M = \frac{\text{speed of molecules}}{\text{local speed of sound}} \tag{5.3}$$

For clustering to occur and for cooling to be observed, it is desirable to maximise the stagnation (nozzle) pressure and minimise the nozzle diameter. However, decreasing the nozzle diameter reduces the gas throughput and hence beam strength. The pumping speed of the vacuum apparatus, the nozzle diameter, the position of the Mach disk from the source, the stagnation pressure and the desired temperature are all considered before such an experiment is designed.

5.2.3 Related Literature

Molecular beams are applied in a wide variety of chemical and physical problems ranging from studies on the smallest diatomic molecule to those on large organic molecules. For reviews see [110, 111, 112]. The number of studies using cooled molecular ions are considerably fewer than those for the corresponding neutral molecules, due to the low beam strength attainable for molecular ions. This study uses the technique of ionisation directly after expansion to create molecular ions. In the design of the apparatus and the experimental techniques used to create molecular ions influences have been taken from from several earlier studies, outlined below.

Larsson et al. [113] have used a supersonic jet source in conjunction with a high frequency deflection technique [114] to make lifetime measurements on various molecular ions and neutral molecules. A molecular beam was crossed by an electron beam, skimmed and emission spectra observed for N_2^+, CO^+ and N_2. Temperatures of around 15 K were achieved, although this was less than the predicted achievable temperature. This was attributable to ambient heating of the beam during the ionisation process. The jet cooled N_2^+ $B^2\Sigma_u^+ - X^2\Sigma_g^+$ (0-0) band was shown to be significantly less congested than the corresponding room temperature spectrum. A redistribution of

state population occurred, where low lying states became more highly populated (and hence their transitions had a greater intensity).

Carrington, Shaw and Taylor [115] recorded microwave spectra of Ar_2^+ and Ne_2^+. A neutral free jet from a liquid nitrogen cooled 20 μm nozzle was crossed with an electron beam. Stagnation pressures of up to 3.5 bar were used, giving pressures of 5 $\times 10^{-5}$ mbar in the source region. In the apparatus, ions were accelerated out of the source using potentials of up to 10 kV in a direction perpendicular to the molecular beam, then mass selected, and enter a waveguide whereupon transitions are induced using microwave radiation. Daughter ions were separated from the parent beam using an electrostatic analyser and detected at a Faraday cup or an electron multiplier.

Bae et al. [116] demonstrated a cluster ion source capable of producing collimated, intense beams of positively or negatively charged clusters. Cluster ions were created using an electron gun focussed directly on the aperture of the pulsed nozzle. The ions were then skimmed and ion optics used to focus the ions, followed by mass selection. Laser radiation from a Nd-YAG system placed anti-parallel to the beam direction created photofragments which were selected using an electrostatic analyser and detected on a multichannel plate. Through the study of the mass spectra it was shown to be possible to create the nitrogen dimer cluster ions $(N_2^+)_n$ with an n value of up to 14.

Coe et al. [117] used a new technique for measuring molecular ions with sub-Doppler resolution. They used direct absorption techniques coupled with fast ion beams, to record a spectrum of HF^+. 3.5 torr of HF was expanded from a water cooled 0.5 mm diameter nozzle, and directed towards an emitting filament. A current of 1×10^{-5} A was attained at 3 kV. This is (at least) an order of magnitude larger than normal ion beam experiments. The absorption path length of the laser system was increased using two 98% reflecting mirrors. Transitions were Doppler tuned into resonance with an Infrared laser by varying the acceleration voltage. Decreases in laser power transmitted through the ion beam occurred where a transition was located. A minimum linewidth of 40 MHz was found for the source and the resolution proved to be capable of resolving hyperfine splittings in the $X^2\Pi$ state of HF^+.

Okumura, Yeh and Lee recorded vibrational spectra for $H_3^+(H_2)_n$. Molecular ions were created using a corona discharge source in which the stagnated gas was ionised before expansion using a corona discharge tip (a nickel plated sewing needle). Care was taken to ensure the purity of the hydrogen gas, and that all water vapour was eliminated. The 75 μm platinum nozzle was cooled by liquid nitrogen or Freon, decreasing the temperature of gases leaving the nozzle, thus improving clustering conditions and decreasing the number of

collisions. The ion beam was skimmed 7 mm downstream from the nozzle, and ions focussed and accelerated after skimming. Cluster ions of up to H_{15}^+ were found to be created in the source.

Bieske and Maier have recorded spectra of a wide range of molecular ions using free jet sources. An example of their work can be found in the study of the B-X transition of N_2^+..He [118]. A water cooled pulsed nozzle with a stagnation pressure of 3 bar (1:100 Nitrogen/Neon) was used as a free jet source. Ionisation takes place inside a shielding cage using a double filament arrangement (constructed from spark plugs). Ions were skimmed and ion optics focussed the beam into a quadrupole mass spectrometer. A dye laser was scanned and daughter ions were collected using a channeltron detector. The entire assembly of the ion source (skimmer, filament and shielding cage) was sprayed with graphite in order to reduce the accumulation of surface charges and stray electric fields which accelerate and warm the ions. To reduce the warming, which had a visible effect on the spectrum, a re-coating was required every few days. The photofragment spectra corresponded to transitions in the N_2^+ chromophore suggesting that the molecule behaves as a free internal rotor. This same apparatus has been used successfully for a number of jet cooled molecular ions including $N_2^+ - Ne_n$ $(1 \leq n \leq 8)$ [119][120], $N_2^+ - He_n$ $(1 \leq n \leq 3)$ [121] and $H_2 - HN_2^+$ [122]

5.3 Experimental

5.3.1 Vacuum Apparatus

The description of the apparatus can be broken down into three areas: Ion source, laser and detection systems. The laser and detection apparatus are those outlined in Chapter 2. The jet source consists of two differentially pumped chambers, one chamber housing the nozzle and skimmer and the second containing ion optics and a flight region. The source and flight chambers are pumped by Edwards EO6K and Balzers BG540 diffusion pumps respectively, which are backed by an Edwards EM18 rotary pump. The source chamber is separated from the diffusion pump by an Edwards butterfly valve, allowing the source to be removed without the need for the diffusion pump to be cold. The flight chamber has an solenoid controlled pneumatic baffle valve (to isolate the diffusion pump), controlled by in-house electronics, a nitrogen cylinder providing the constant gas supply to the valve. A gas line connected to the flight chamber is used to 'rough' both chambers through the rotary pump. This line is sealed when not in use using a VG isolation gate valve. Each diffusion pump can be individually sealed from the backing line using Speedivac valves. Pressure in the backing lines and in the jet region are measured by a VG Pirani gauge (VGPV1) and a ZWW16 ion gauge respectively. Both gauges are controlled and displayed using a VG IGPA3 ion gauge control unit. A second ion gauge (Kratos Analytical) is mounted in the flight region, the pressure reading displayed on a Kratos Vacuum

Controller. The diffusion pumps, ion gauge controllers, rotary pump and electric/gas baffle are all powered through an in-house device, which cuts power to the diffusion pumps in the event of a power cut or loss of vacuum in either chamber.

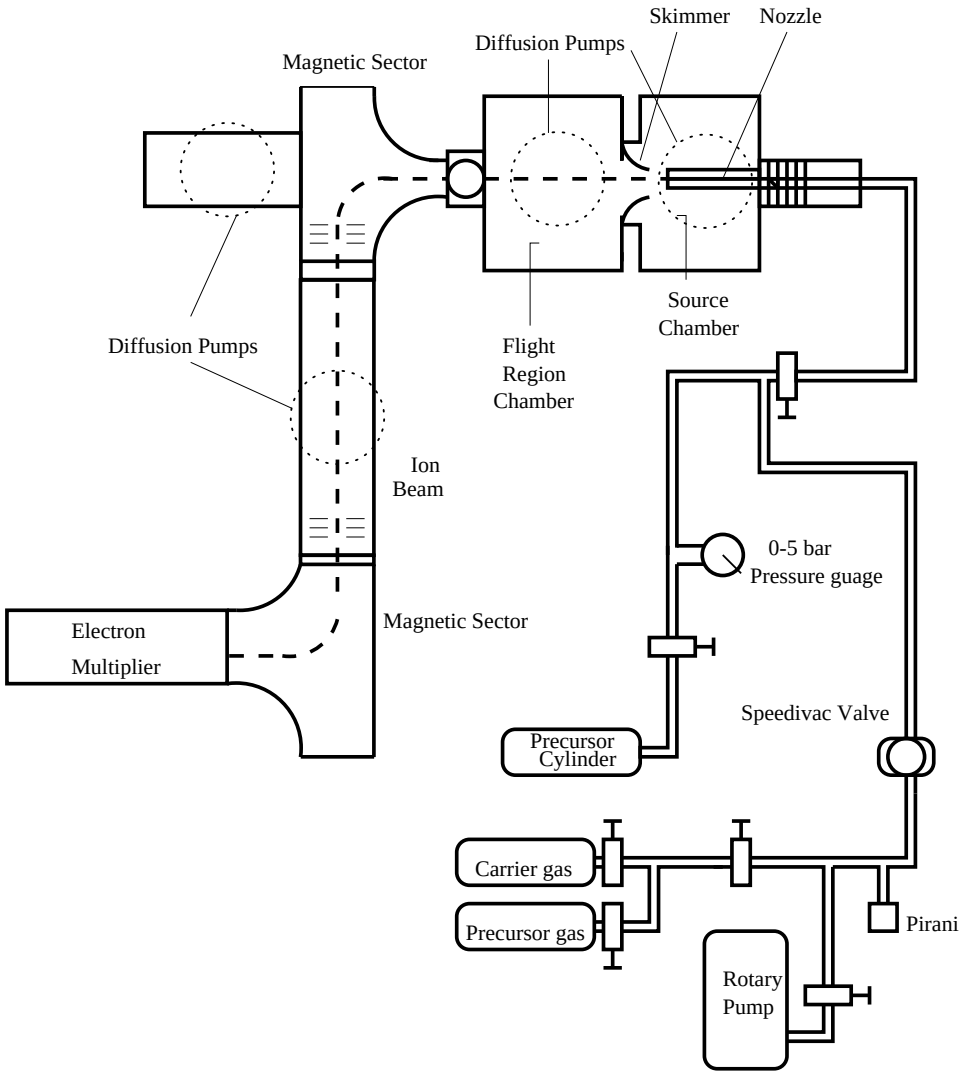

Figure 5.1 Construction of the premixture apparatus.

5.3.2 Ion source

The ion source is mounted in a stainless steel chamber above the Edwards E06K diffusion pump. The jet nozzle is mounted at the end of a stainless steel tube, which in turn is mounted on bellows to allow axial translation of the jet assembly. Horizontal and vertical translation of the nozzle can be obtained by the adjustment of six translational screws. The gas line passes through an O-ring seal and an electrically isolated Teflon Swagelok

seal and enters the nozzle region. A pinhole (Ealing [diameter 12.5-75 μm]) is mounted inside a threaded holder, screwed to end of the gas line. An O-ring seal prevents gas from escaping at the gas line/nozzle holder interface.

A Micromass MM6 filament and trap are mounted on either side of the nozzle, the normal orientation being with the filament mounted vertically above the nozzle, the trap diametrically opposite. A copper cage surrounds the ion source to prevent penetration of stray fields into this region. The ion source can be translated with respect to the nozzle so that the distance between filament and nozzle can be adjusted. Typical filament/nozzle horizontal separations are between 2 mm and 10 mm. The filament is regulated in Electron Impact (EI) mode i.e. the electron current arriving at the trap was held constant by varying the current through the filament. It was found that the jet source could maintain emission currents of 1000 μA for several weeks, in comparison to the conventional ion source which can maintain currents of this order for a few days only. This is due to the open design of the nozzle: the flowing gas is ionised in an open space, as opposed to the normal EI source (which confines gas in a source block). The electron beam passes unhindered through to the trap in the jet source, whereas in a standard EI source it has to pass through an entrance hole and an exit slit in a source block. Filaments are usually destroyed when too large a filament current (typically above 4 amps) is needed to keep a constant emission current. In the jet source, the filament is under less strain due to the lower current (typically 2 Amps) needed to obtain the same emission current. This open design of ion source allows filament changes and source cleaning to be carried out quickly and simply due to the ease of access. Magnets mounted above the filament and below the trap cause the electrons to spiral, increasing their flight path as occurs in a conventional ion source. The source and copper cage, filament and trap are connected to a high voltage programmed power supply (VG M18A) using Teflon coated copper wires connected via electrical feedthroughs. Trap and filament currents are read/regulated using an emission control and source control VG M93 and M71 respectively. The emission control unit has a small modification which allows the trap current (normally held at +50 V), to be varied between 24 and 55 V.
A high vacuum viewport (68 mm diameter) is mounted at the side of the chamber, centred on the nozzle/skimmer region, allowing visual nozzle adjustments to be made without danger of touching the skimmer.

5.3.3 Skimmer and ion optics

A skimmer (Beam Dynamics nickel type 1, orifice diameter 0.4-0.8 mm) is mounted on a partition wall of the source chamber. The mounting design is such that the skimmer can be mounted and removed quickly and easily, without damage to the thin nickel walls: it is placed into a recess (2.3 cm with a 1 cm hole through the center) of a stainless plate, over which a mount-

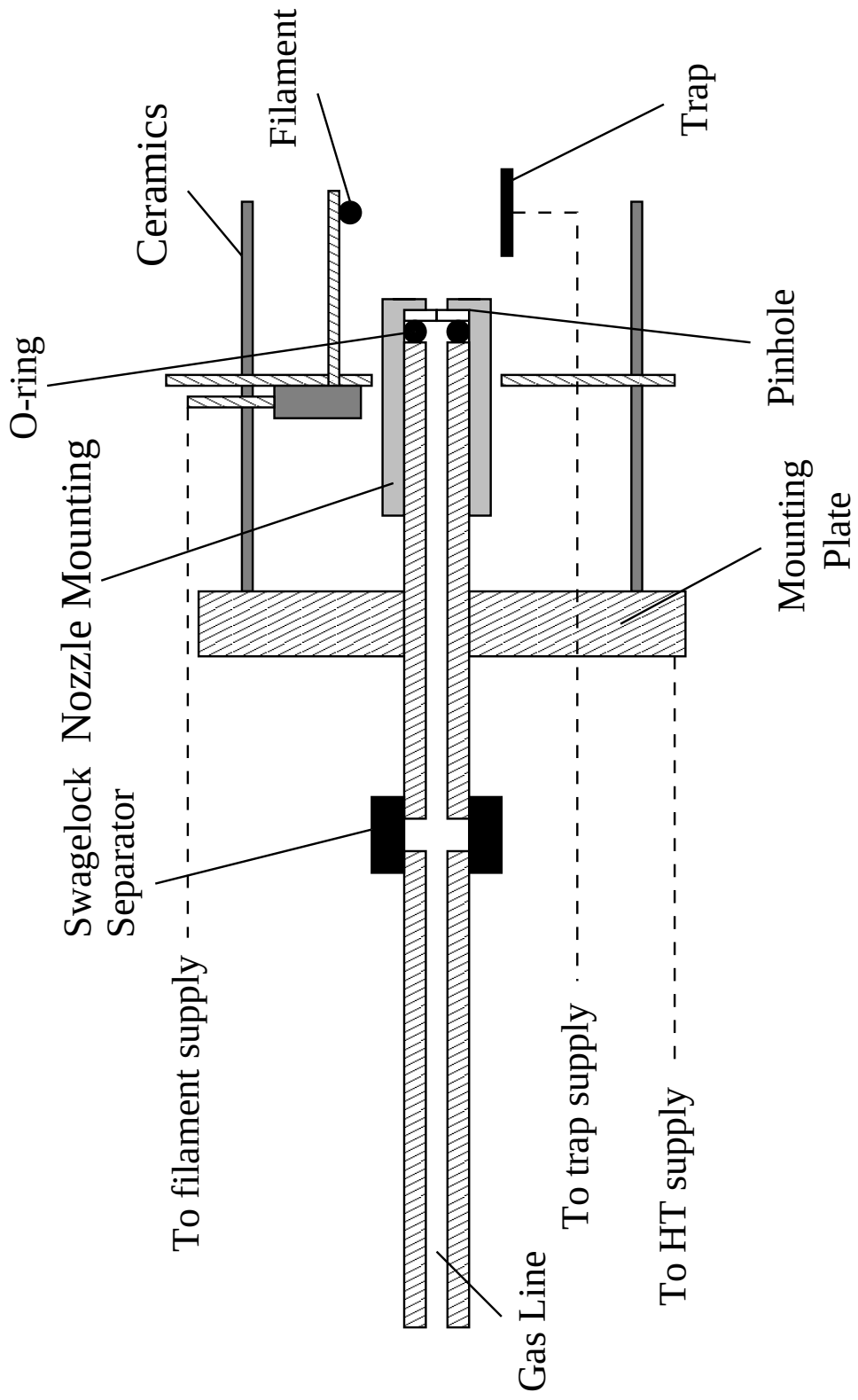

Figure 5.2 Nozzle design

ing ring is then placed and held securely by three stainless steel screws. A Teflon coated copper wire is screwed onto the plate, passing through the feedthroughs, and is connected to the high voltage supply (see Figure 5.3). The plate is placed inside the vacuum chamber and screwed into place using six mounting bolts. Teflon isolates the plate from the chamber partition, to allow the application of voltages to the skimmer. Typically voltages for the skimmer can vary up to ± 50 V from the source voltage, controlled and read by a VG M71 source control unit.

Ion optics are mounted on the partition wall protruding into the flight region chamber, positioned axially to the nozzle and skimmer. These consist of several earthed plates and two plates in the Y plane and two in the Z plane. As the plates are earthed individually, a TIM signal can be measured after skimming the ion beam. The lens stack design is similar to the stack at the first magnetic sector; however, it is possible to vary the voltages over a greater range than for the conventional lens stacks using a separate ion optics control box (in-house device). Typical ranges for these lenses are 0-10 % of the acceleration voltage, applied to the ion optic stack via a feedthrough port mounted vertically in the flight chamber. Teflon coated copper wires connect the lens stack plates to this feedthrough plate.

5.3.4 Alignment of the nozzle to the skimmer

For the creation of cold molecular ions, it is essential that the nozzle and skimmer are aligned axially. To achieve such an alignment, two techniques were used: a coarse alignment procedure was undertaken with the source and flight region chambers at atmospheric pressure and separated from each other and fine alignment achieved with the apparatus under vacuum.

A helium-neon laser was mounted on a 30×30 cm optical bench consisting of two steering mirrors facing in perpendicular directions. The optics were adjusted to steer laser radiation through the gas line and exit from the nozzle. With the two chambers separated, the nozzle was aligned to the skimmer using the nozzle translational controls. When the laser spot could be observed passing cleanly through the skimmer, the nozzle and skimmer were aligned. The chambers were then reconnected and pumped down to vacuum.

Gas was then passed through the nozzle and fine adjustments made using the translational screws. Flight region pressure was then monitored, if the nozzle/skimmer alignment improved, the flight region pressure increased. If the alignment was poorer, the pressure fell. In this manner, the nozzle was correctly aligned to the skimmer, until a maximum was reached for all translations of the nozzle.

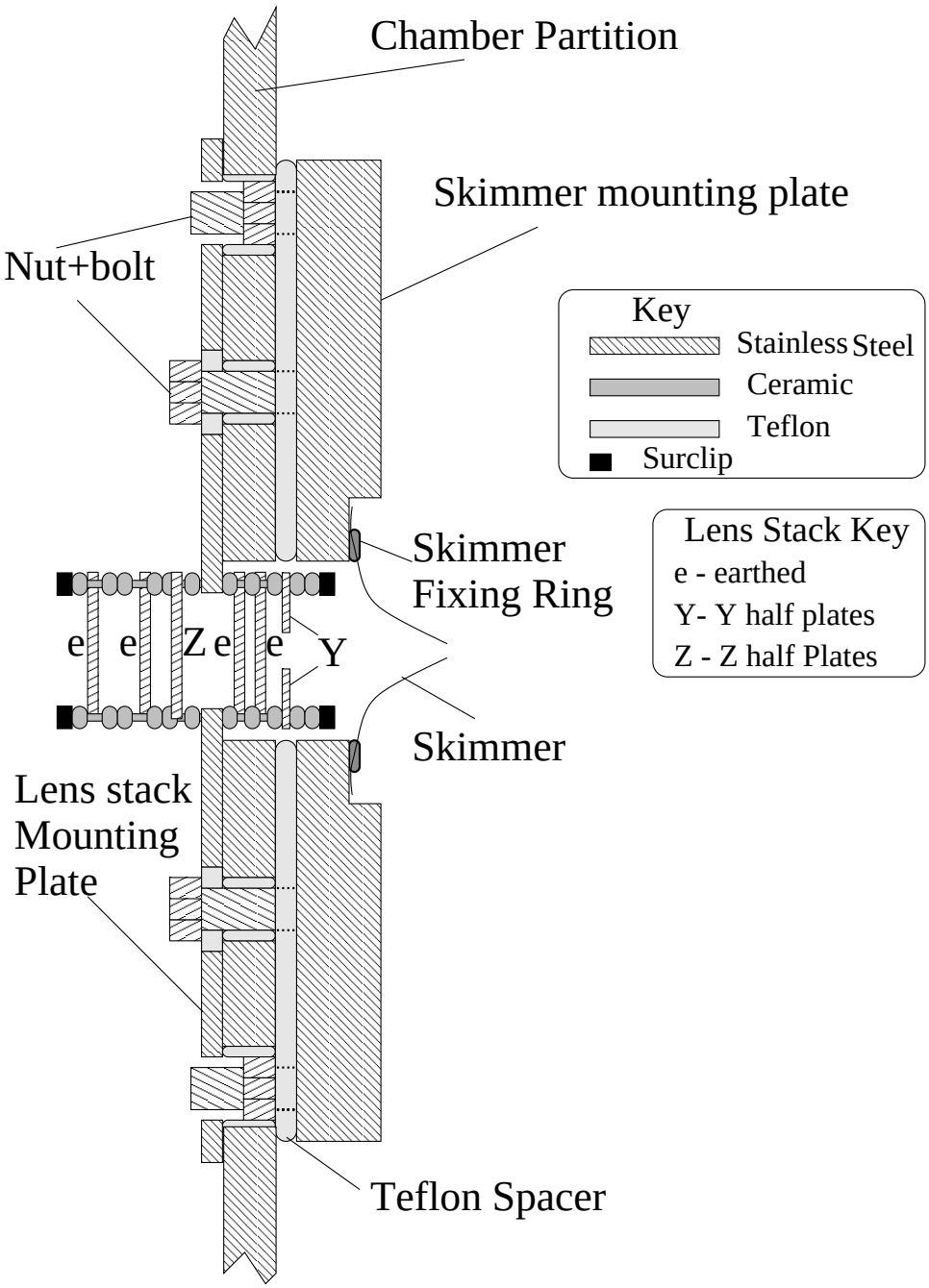

Figure 5.3 Illustration of the nickel skimmer mounting and the lens stack construction inside the flight region chamber.

5.3.5 Mixtures of Gases

A mixture of precursor and carrier gases were used to create colder molecular ions than could be achieved without a buffer. For jet sources, normal carrier gases are argon or helium. An apparatus was constructed which enabled two gases to be mixed in a third cylinder, which could be fully evacuated (via an independent rotary pump), to allow the use of spontaneously flammable gases. A 0-5 bar pressure gauge monitored the filling and nozzle pressures (see Figure 5.1). Gas flow into the mixing cylinder could be carefully controlled through the use of a VGMD7R leak valve. Typical carrier gas to precursor gas ratios were 5:1, 10:1 and 20:1, and a typical nozzle (stagnation) pressure was 3 bar.

5.4 Review of O_2^+

5.4.1 Introduction

In this section series of experiments are discussed which recorded a spectrum of O_2^+ using the new ion source. There are several advantages of using O_2^+ to characterise the apparatus: large ion currents are achievable, the precursor gas O_2 is available at relatively low cost and high purity and the ion has a well understood photofragment spectrum. The aim of this series of experiments was to prove that the apparatus could be seriously considered as an alternative to the EI source, offer advantages in terms of rotational cooling of any spectra and generate cluster ions.

5.4.2 States and Spectroscopy of O_2^+

The spectroscopy of O_2^+ is well understood and has been studied at high resolution using laser photofragment apparatus [39, 40, 4, 116, 123, 124, 125, 126, 127]. It is therefore considered to be a 'benchmark molecule', from which experimental parameters can be deduced. A recent paper by Ashman et al. [128] to characterise an ion cyclotron trap (ICR) apparatus used O_2^+ as the molecular ion of choice to characterise the temperature of the molecule inside the trap from the predissociation spectroscopy.

The electronic transition of interest for these experiments is the $b^4\Sigma_g^- \leftarrow a^4\Pi_u$. All electronic transitions thus far observed in photofragment spectroscopy result in transitions to form $O(^3P_2) + O^+(^4S^0)$. Rotational levels of the lower electronic state are split into four fine structure components through the spin-orbit interaction, these are $^4\Pi_{\frac{5}{2},\frac{3}{2},\frac{1}{2},-\frac{1}{2}}$, and are labelled F_1, F_2, F_3 and F_4 respectively. Each rotational component of the ground state is split by lambda doubling, with only negative parity levels present in the homonuclear $^{16}O_2^+$. Each component is separated by approximately 50 cm^{-1} from the others (the exact value depending upon the vibrational and rotational

states involved). The upper ($b^4\Sigma_g^-$) electronic state has four spin components, labelled:
F_1' ($J' = N' + \frac{3}{2}$), F_2' ($J' = N' + \frac{1}{2}$), F_3' ($J' = N' - \frac{1}{2}$) and F_4' ($J' = N' - \frac{3}{2}$). Due to the zero spin of oxygen nuclei and nuclear spin statistics, only odd valued N' are present. Transitions between the two electronic states are labelled using the following nomenclature: $N'\Delta J_{Fn'Fm''}(J'')$ Where ΔJ is P, Q or R for values of -1, 0, and +1 respectively. The majority of lines observed in the visible region predissociation spectra of O_2^+ are due to to transitions from v''=3, 4 and 5 to v'=3, 4 and 5.

5.4.3 Experimental Setup

The chamber was connected to the ion beam apparatus using a gate valve. The first magnetic sector was rotated through 90° and the current polarity reversed. Three sets of ion optics were used: immediately after the skimmer, after the first magnetic sector and before the second magnetic sector. Ion currents could be monitored at these positions using T.I.M. plates. Voltages for the ion optics mounted at the magnetic sectors are controlled by the high voltage supply for the conventional EI source. The supply was set to 2 kV, which applied voltages of 200 V to the ion optics. However, this value could be adjusted to optimise the ion beam strength from the jet source. In practice, for a jet source voltage of 2 kV, the EI high voltage supply was set to 1.8 kV (for O_2^+). Individual plate voltages were set using the ion optics control unit. Gas enters the jet source through a stainless steel gas line, regulated by a needle valve. The gases in the following experiments were oxygen or oxygen mixed with helium or argon.

Nozzle pressures of 2-3 bar were used, resulting in a pressure of 10^{-6} and 10^{-7} torr in the source and flight regions respectively. Electrical breakdown occurred in the source chamber at approximately 200 V. Experiments showed that this problem was due to the Swagelok fitting, however this breakdown could be avoided when 2-3 bar of gas flowed through the nozzle, allowing voltages >2.5 kV to be achieved (for oxygen).

The emission current of the filament was set to 1000 μA for the majority of experiments and the jet source programmed power supply was set to 2 kV. Optimal ion current arriving at the first magnetic sector was achieved when a small negative voltage was applied to the skimmer (typically -12 V). As mentioned previously, the trap potential could be varied between 55 and 24 V. This voltage was optimised so as to maximise ion current. Laser radiation from the CR 699-29 tunable dye laser entered the vacuum apparatus through the Brewster window mounted on the cross piece at the first magnetic sector. Due to the photofragmentation process ($O_2^+ \rightarrow O^+ + O$), O^+ ions could be directed towards an electron multiplier when the laser radiation was collinear with the ion beam.

After optimisation of ion optics, the laser was scanned and an O_2^+ spectrum recorded. The following parameters were used: 30 MHz sampling rate, 40 s/10 GHz segment, lock-in time constant 1 s, 500-10000 μV sensitivity (depending on signal to noise, ion current and laser power) and 1000 μA emission current.

The laser was scanned across regions between 17200 and 17300 cm^{-1} to find the strongest lines of the (4-4) band of the $b^4\Sigma_g^- \leftarrow a^4\Pi_u$ transition. These regions have line positions recorded to a precision greater than 0.003 cm^{-1}, and have large densities of lines [125]. A recording taken using a conventional EI source is shown in Figure 5.4. This spectrum has a dominant transition at 17261.3 cm^{-1} made up of three components, a shoulder at 17261.338cm^{-1} 9 P_{31} (9.5) and a larger peak, at 17261.387cm^{-1} . This peak is a blend of two lines, the dominant 9 Q_{21}(9.5) and the much weaker 17 Q_{11}(18.5). This line has been deconvoluted into individual contributions using an energy analyser [125] which samples different ranges of rotational levels above the dissociation limit. Several other transitions are found in this region, including two transitions involving the same spin states [the 17 P_{21}(18.5) and the 9 Q_{21}(9.5) transitions].

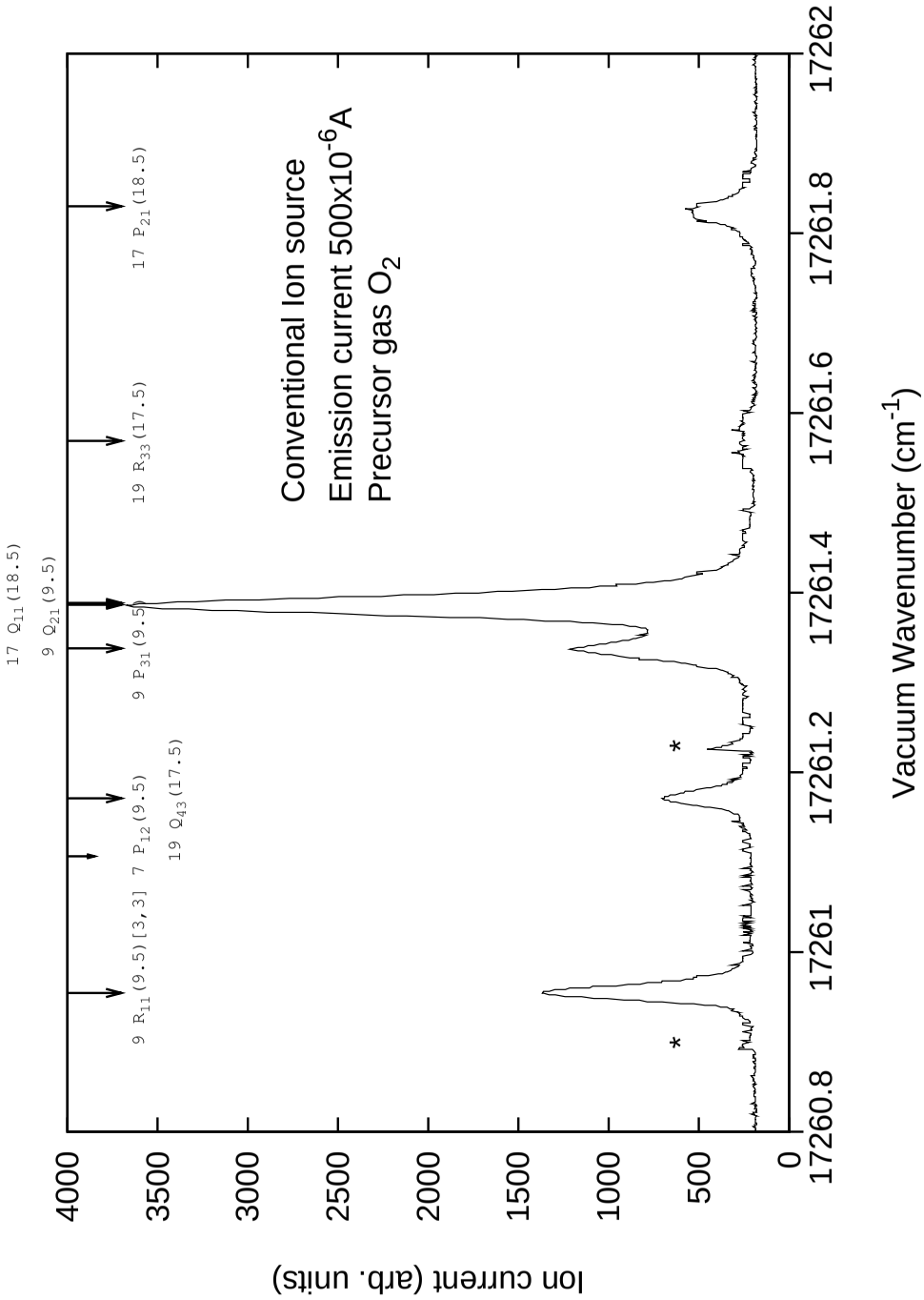

Figure 5.4 O_2^+ spectrum recorded in a conventional ion source. Labelled transitions taken from the study by Cosby et al. [125]. Laser mode hops are indicated by *.

5.5 Results

5.5.1 Jet apparatus results

The initial results from the jet apparatus were comparable to those found from a conventional ion source. A spectrum of O_2^+ was recorded with a satisfactory signal to noise ratio, with only a small decrease in ion current of one order of magnitude (the jet source achieved 1×10^{-8} A at the first magnetic sector lens stack TIM). The distance between the source and magnetic sector is significantly larger ($\approx$ 65 cm) compared to the conventional ion source ($\approx$ 15 cm), and hence a decrease in ion current was expected due to collisional and unimolecular decomposition of the molecular ions in the beam. Extra pumping capacity in the jet source compensates for flight region losses, as higher source pressures can be used. The pressure in the source chamber can reach 1×10^{-4} torr without damage to the diffusion pump or filament. This pressure is two orders of magnitude greater than that of a conventional ion source. An initial spectrum of O_2^+ is shown in Figure 5.5. Linewidths in this region are approximately 500 MHz, identical to those found in a conventional EI source with an acceleration voltage of 2 kV. Both these values are higher than those reported by Cosby et al. where all transitions have widths between 275 and 450 MHz [125]. This is probably due to the low acceleration potential, in comparison to that used by Cosby et al. (3.6 kV). The signal to noise ratio is poorer in comparison to the conventional ion source spectrum, probably due to the lower beam currents from the jet source.
Comparison between intensities of 9 $Q_{21}(9.5)$ and 17 $P_{21}(18.5)$ in Figures 5.4 and 5.5 show that virtually no intensity redistribution occurs between the jet source and conventional source with a 25 μm nozzle and no carrier gas.

5.5.2 Estimation of temperature

The temperature of the ion beam can be estimated through comparison of the spectroscopic lines of O_2^+. The following assumptions were made to quantify the jet source temperatures:

- A conventional EI source creates (O_2^+) molecular ions at a temperature of 500 K [129, 130].
- Populations of rotational levels in the jet source can be modelled using a single Boltzmann distribution and temperature. This can be generally accepted as the case for molecular beam studies despite the non-equilibrium conditions which exist within a supersonic jet.

A redistribution of rotational populations results in an increase for low lying rotational states and a corresponding decrease in high lying states. Assuming that the temperature of the conventional ion source and jet source can be

modelled by a Boltzmann distribution, it can be shown that the intensity of a given transition to N″ can be estimated from [113]:

$$I_{N',N''} \ \alpha \ \ S_{N',N''} exp\left(\frac{-B''}{kT}(N''(N''+1)\right) \tag{5.4}$$

Where $I_{N',N''}$ is the intensity of a transition, $S_{N',N''}$ is the Honl-London factor for that transition, N″ is the total angular momentum excluding nuclear spin, T is the temperature and k is the Boltzmann constant.

For this work, a spectrum was recorded in the normal ion source and the intensity ratio of two lines in the same spin states was determined. The same spectrum was then recorded at a lower temperature, and the ratio of the two lines again taken, the ratio *of the ratios* of the intensities are used to determine a temperature for the cooler spectrum, assuming that the temperature of an EI source is 500 K. As the ratio of the two Honl-London factors remains constant with temperature, this assumption is valid.

Over 50 scans were recorded, using different source conditions and the following subsections outline these different series of experiments used to characterise and optimise the jet source.

Nozzle Diameters

Spectra for O_2^+ were obtained using two different nozzle diameters, made from 25 μm and 12.5 μm pinholes (Ealing). No discernible loss of ion current occurred with the smaller nozzle, as the stagnation pressure was increased to compensate for reduced throughput (see Figure 5.6). Analysis of the recorded spectra using several different mixes of precursor gases show that a significant change in the temperature occurs when the smaller nozzle is used. The intensity ratio between the 9 $Q_{21}(9.5)$ and 17 $P_{21}(18.5)$ transitions recorded using the conventional ion source and for the two different nozzle diameters are measured and temperatures deduced (see Table 5.1). A significant decrease in intensity of the 17 $P_{21}(18.5)$ line relative to the 9 $Q_{21}(9.5)$ line is found to occur with the smaller nozzle, corresponding to a significant decrease in the temperature of the ion beam. The temperature of the ion beam is found to be $\approx$ 125 K, a reduction of approximately 400 K from a conventional EI source. This experiment demonstrates that the ion source can create a significantly rotationally cooler molecular ion beam, with a reasonable ion current and without loss in signal to noise ratios or the linewidth.

Gas mixtures

To increase the cooling of the molecular beam from the jet source, the precursor gas was mixed with various ratios of argon and helium buffer gases. Results using oxygen and argon mixtures on the spectrum of O_2^+ are shown in Figure 5.7. A marked effect on the spectrum is observed, in that the 19

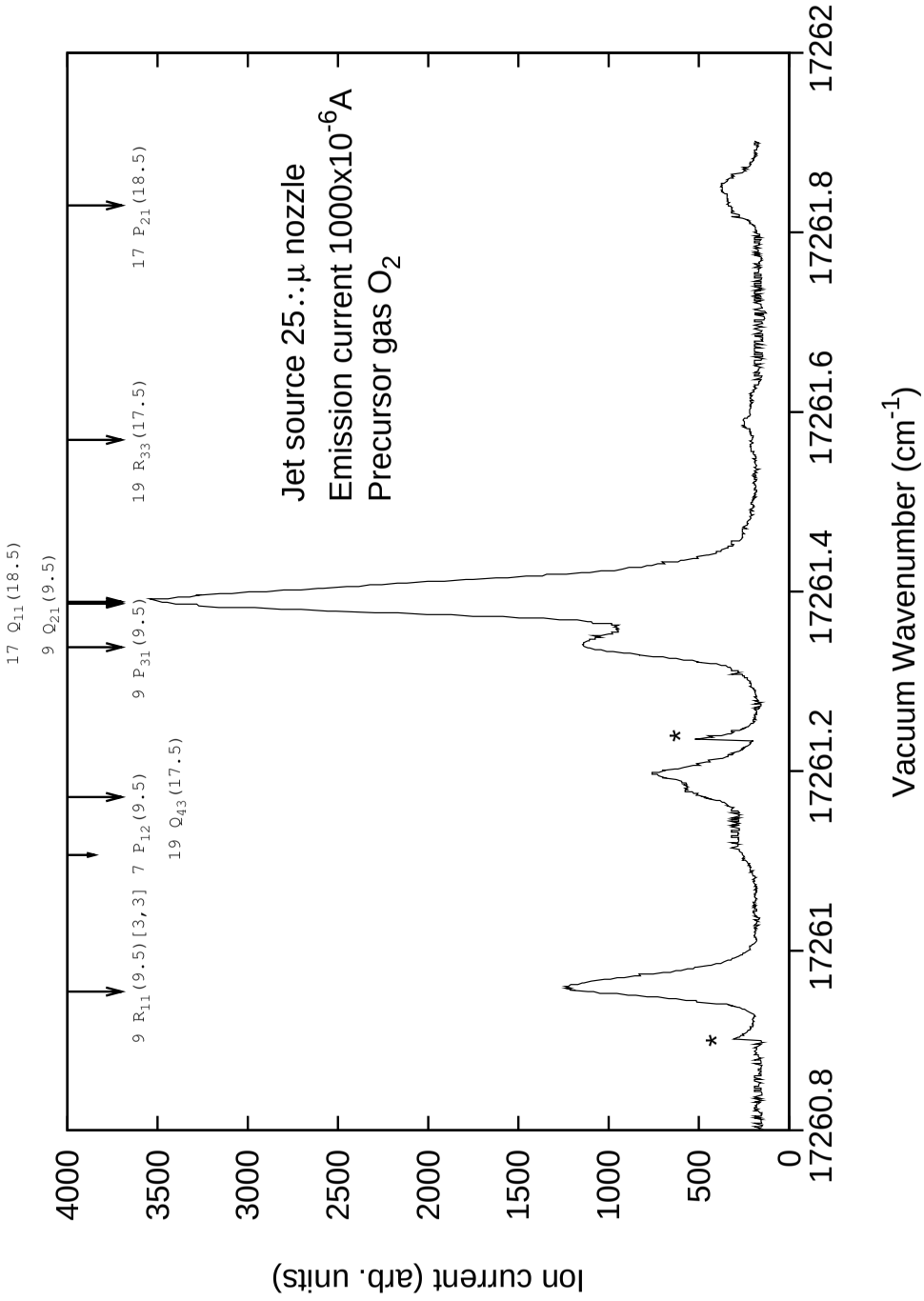

Figure 5.5 O_2^+ spectrum using Jet source. Labelled transitions taken from study of Cosby et al. [125]. Laser mode hops are indicated by *

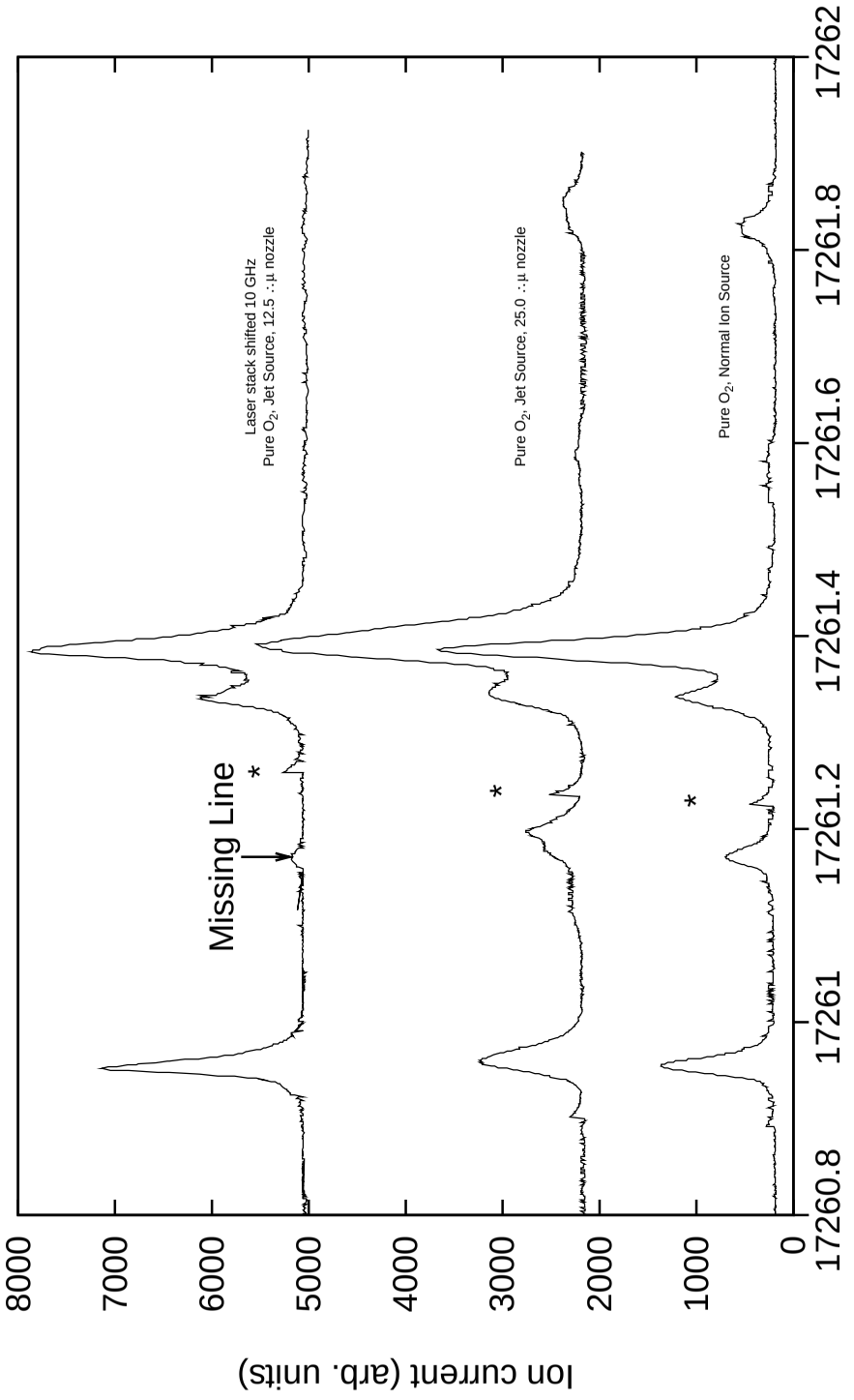

Figure 5.6 Comparisons of O_2^+ spectra with nozzle diameter. The lowest trace shows normal ion source spectrum. Middle trace shows the jet source spectrum with a 25 μm nozzle. The upper trace shows the spectrum with a 12.5 μm nozzle. Mode hops are indicated by *. N.B. The positions of the mode hop changes with the change in laser scan segment length (extended by 10 GHz).

Nozzle diameter	**Intensity ratio**	**Temp (K)**
N/A (Electron Impact source)	9.41	500 (assumed)
25μm	17.51	264
12.5μm	75.06	126

Table 5.1 Comparison of the intensities of the 9 $Q_{21}(9.5)$ and 17 $P_{21}(18.5)$ transitions for different nozzle sizes. Pure O_2^+ is the precursor gas.

$Q_{43}(17.5)$ and the 17 P_{21} (18.5) are observed to decrease to the extent where they are virtually indiscernible from the background signal. A similar but greater effect occurs when helium is used as the buffer gas, however, the signal to noise ratios remain unaffected using this gas. The helium seeded beam has a greater ion current than that obtained using pure oxygen alone, and yields signal to noise ratios comparable to those found in a normal ion source. See Table 5.2 for comparison between the different precursor gas ratios. Helium is shown to reduce the rotational temperature to a greater extent than for argon, and has the added benefits of increased ion currents and better signal to noise ratio. Helium mixed with oxygen in the ratio of 5:1, gave an estimated temperature of 85 K. This temperature could be decreased further with an increase of pressure and/or a higher ratio mixture, but is still significantly higher than the value calculated from equations Equation 5.2 and [131], which yield 7 K. This is probably due to heating from the environment due to the proximity of the filament.

Precursor gas (ratio)	**Intensity ratio**	**Temp (K)**	**Relative beam strength**
O_2 (N/A)	75	125	77.3
Ar (5:1) O_2	83	121	5.7
Ar (10:1) O_2	87	119	21.6
He (5:1) O_2	289	85	100

Table 5.2 Comparison of the intensities of the 9 $Q_{21}(9.5)$ and 17 $P_{21}(18.5)$ transitions for different ratios of carrier gas mixtures/precursor mixtures. Normalised daughter ion current for each precursor is also shown.

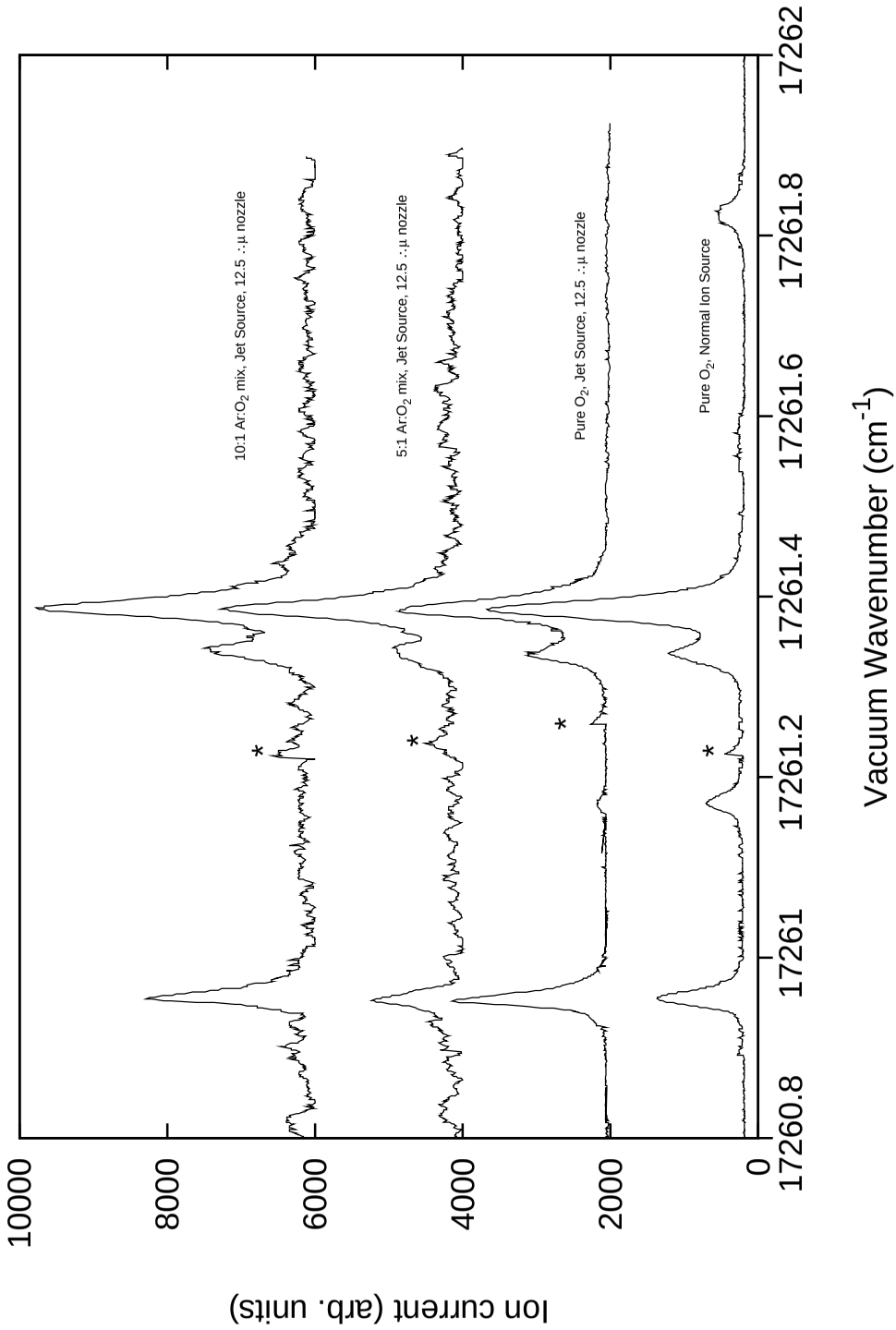

Figure 5.7 Effect of a using argon as a carrier gas. Notice reduction in intensity of the N =19 and 17 transitions relative to those of smaller N. With a 10:1 mixture, these transition are impossible to distinguish from the background signal. Laser mode hops are indicated by *.

Shielding the source

To examine the effect of the source region having an open plan design, a series of experiments were undertaken using a modified ion source. This involved electrically 'shielding' the region directly in front of the jet expansion. The filament is floated at approximately -70 V, the trap at +55 V, making it possible for the ion source to deflect the ions towards the filament upon creation. It was reasoned that this would apply an artificial electric field gradient, deflecting the ions upon their creation, possibly leading to heating and lower beam strengths.

A small U shaped stainless steel plate was constructed, with holes on either side to allow the electron beam to pass cleanly in front of the nozzle and arrive at the trap. The U shaped 'shield' was welded onto the nozzle mounting plate and floated at the same voltage as the source.

An ion beam was created and spectra recorded for comparison. These are shown in Figure 5.8. A small heating effect occurs in these spectra, corresponding to an increase in the intensity of transitions for high N, relative to those for low N. Typical temperature increases are of the order of 50 K, possibly due to heating of the shield by the filament, where the heat is then being conducted to the region close to the nozzle. Table 5.3 lists the temperatures found for pure O_2, Ar and O_2 and He and O_2. A greater recorded ion current is found in all the experiments when the shield is used, whilst the signal to noise ratio is seen to remain approximately constant. This increase of ion current is up to 5 orders of magnitude greater than that found without the shield in position.

The reason for this apparent increase of ion current, and apparent increase in temperature is uncertain. It is suggested that more ions are indeed now arriving at the skimmer, and not deflected by an electric field gradient due to the filament/trap arrangement. However, a warming effect occurs due to the extra nozzle heating, which is a distinct disadvantage if a colder beam is required.

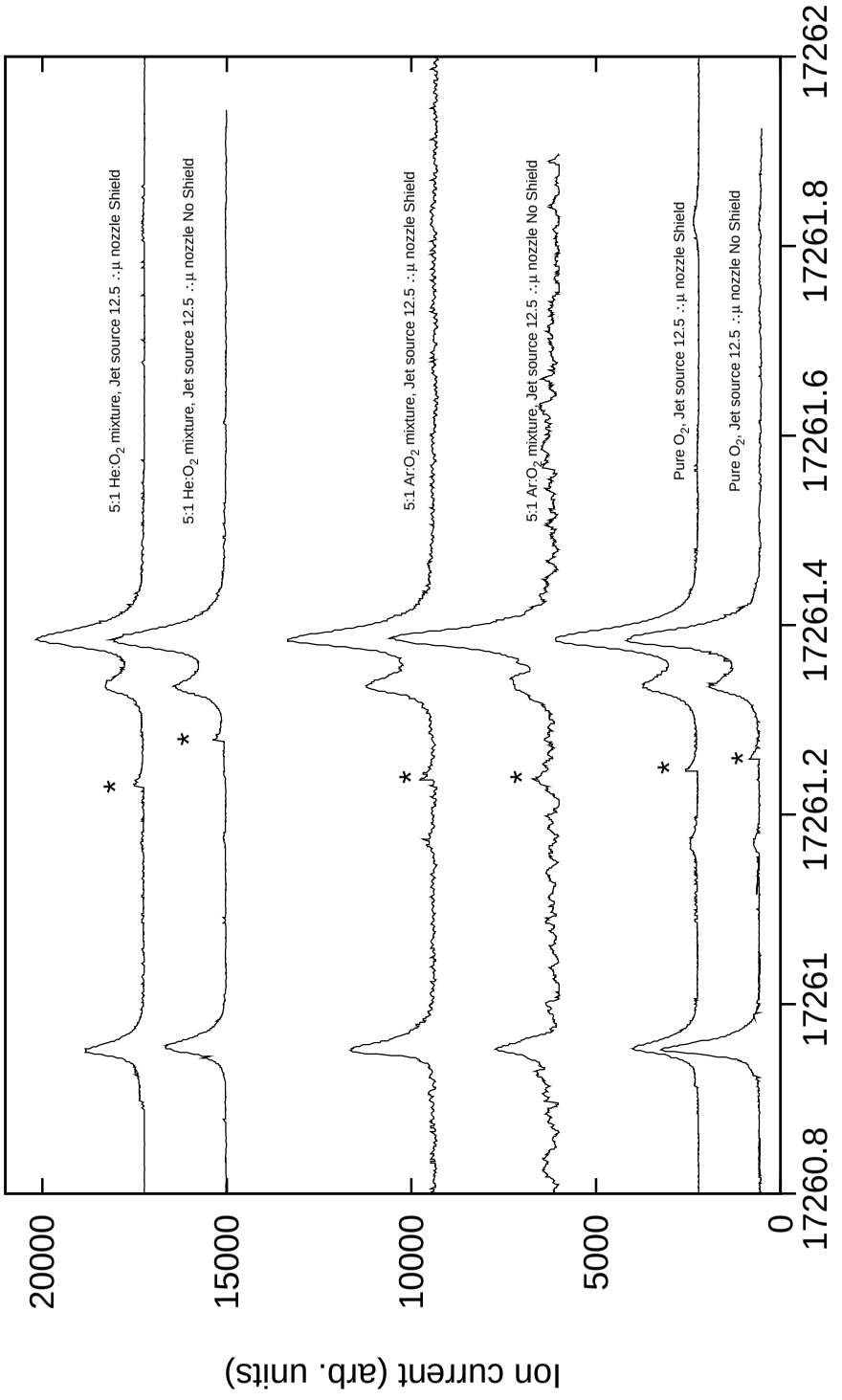

Figure 5.8 Effect of a using a shield. Note the increase in the intensity of the high N transitions with the shield, than with the shield not in place. This occurs similarly for a pure oxygen precursor and a buffer/oxygen precursor.

Precursor gas (ratio)	**Intensity ratio**	**Temp (K)**	**Relative beam Strength**
O_2 (N/A)	33	178	474
Ar (5:1) O_2	53	144	31.4
He (5:1) O_2	68	130	471

Table 5.3 Comparison of the intensities of the 9 $Q_{21}(9.5)$ and 17 $P_{21}(18.5)$ transitions using the shield and different ratios of carrier gas mixtures/precursor mixtures. Relative beam strengths are normalised for direct comparison with Table 5.2

Other experimental considerations

Several other experimental considerations concerning the construction of a jet source ion beam, are summarised below:

- A negative skimmer voltage of 11.5 V with respect to the source is essential to create ion beams of a reasonable strength.
- No heating effect occurs when the emission current of the filament is raised from 1000 to 2000 μA. No extra cooling is observed with the emission current at 500 μA.
- Changes in the trap voltage had no observable heating effect, but greater currents were achieved with the trap kept at low voltage ($\approx$25 V)
- Nozzle-filament distances of approximately 6 mm yield the strongest ion beams.
- The distance between the nozzle and skimmer is also critical. For a 12.5 μm nozzle it is difficult to detect any photofragmentation of O_2^+ at 10 mm. 5 mm gave reasonable ion currents and the maximum rotational cooling.

An increase in ion beam current and cooling could be obtained if the nozzle pressure was increased to pressures greater than 3 bar. The diffusion pump in the source region showed no signs of stalling when operating with Helium at 3 bar, (the backing line pressure was 0.05 torr, well below the maximum

allowed value of 0.5 torr). However, any effect of higher pressures on the pinhole surface needs to be considered, although little damage to the nozzle was observed during the experiments documented in the previous sections.

An alternative method for increasing the beam current would be increasing the high voltage applied to the source region. However, this probably involves a re-design of the nozzle/gas line assembly, to prevent electrical breakdown, which inevitably occurs above 2.5 kV. Finally, water (see Bieske et al. [119]) or liquid nitrogen (see Carrington et al. [115]) cooling of the nozzle may yield further reduction in the beam temperature with only minor modifications to the existing apparatus.

5.6 Conclusions

It has been demonstrated that a CW jet-cold fast ion beam source can be constructed, capable of creating molecular ions with temperatures typically around 100 K. It has been shown that a continuous jet can be formed, ionised immediately after supersonic expansion, skimmed and a photofragment spectrum recorded. The spectroscopic linewidths and signal to noise ratios are seen to be comparable to those obtained using a conventional EI source.

Appendix A Assigned line positions

v′	v″	J″	P(ΔJ=-1)	Q(ΔJ=0)	R(ΔJ=+1)
0	3	4	17583.611	17609.863	
		5	17547.959	17580.606	
		6	17506.442	17545.327	17590.865
		7	17458.959		17555.634
		8	17405.452	17456.421	17514.043
		9	17345.798	17402.569	17466.030
		10	17279.980		17411.400
		11		17275.538	17350.046
		12		17202.096	
		13		17121.861	17206.583
		14		17034.653	17124.215
		15		16940.498	17034.548
		16	16747.947	16838.002	16937.576
		17	16635.263	16730.359	
1	3	9	17713.967		
		10		17702.230	
		11	17567.908	17630.789	17700.605
		12	17484.712	17552.332	17627.120
		13	17394.592	17466.849	17546.408
		14		17374.094	17458.374
		15	17193.366		
2	3	2			18391.372
		3		18354.021	18377.718
		4	18304.463	18327.944	18357.191
		5	18266.071	18295.012	18329.643
		6	18220.878	18255.116	18294.964

Table A.1 Assigned transitions of $^{70}GeH^{+}$(vacuum cm^{-1})

v′	v″	J″	P(ΔJ=-1)	Q(ΔJ=0)	R(ΔJ=+1)
0	3	1		17664.468	17677.841
		2	17639.673	17652.963	17672.836
		3	17615.809	17635.424	17661.979
		4	17586.017	17612.222	17645.076
		5	17550.470	17582.987	17622.237
		6	17508.873	17547.748	17593.297
		7	17461.447	17506.387	17558.075
		8	17407.947	17458.885	17516.494
		9	17348.377	17405.097	17468.494
		10	17282.605	17344.861	17413.912
		11	17210.477	17278.136	17352.597
		12	17131.945	17204.746	17284.412
		13	17046.821	17124.566	17209.250
		14	16955.039	17037.437	17126.919
		15	16856.420	16943.262	17037.322
		16	16750.900	16841.914	16940.409
		17	16638.313	16733.343	
		18	16518.629		
1	3	8		17826.758	
		9	17716.356	17769.122	17828.460
		10	17646.746	17704.643	17769.274
		11	17570.455	17633.256	17702.999
		12	17487.295	17554.875	17629.564
		13	17397.230	17469.415	17548.893
		14	17300.178	17376.847	
		15	17196.093	17277.226	
2	3	1			18400.165
		2		18375.292	18393.223
		3	18338.072	18355.913	18379.561
		4	18306.408	18329.819	18359.002
		5	18267.998	18296.877	18331.487
		6	18222.795	18256.994	
		7	18170.693	18209.949	
2	4	2			16641.331
		3			16628.722
		4	16556.902	16580.443	16609.629
		5		16549.321	
		6	16477.423		

Table A.2 Assigned transitions of $^{74}GeH^{+}$(vacuum cm^{-1})

Appendix B Non linear least squares fit residuals

Transition	Expt. value	Calc. value	Diff.
(0,3) Band			
P(2)	17639.673	17639.709	0.036
P(3)	17615.809	17615.745	-0.064
P(4)	17586.017	17585.982	-0.034
P(5)	17550.470	17550.383	-0.087
P(6)	17508.873	17508.897	0.024
P(7)	17461.447	17461.459	0.012
P(8)	17407.947	17407.992	0.045
P(9)	17348.377	17348.408	0.031
P(10)	17282.605	17282.609	0.004
P(11)	17210.477	17210.487	0.010
P(12)	17131.945	17131.929	-0.016
P(13)	17046.821	17046.815	-0.006
P(14)	16955.039	16955.022	-0.017
P(15)	16856.420	16856.426	0.006
P(16)	16750.900	16750.904	0.004
P(17)	16638.313	16638.337	0.024
P(18)	16518.629	16518.611	-0.018

Table B.1 Non-linear least squares fits results for the P branch of the (0,3) band of the $^{1}\Pi$-$^{1}\Sigma^{+}$ transition of $^{74}GeH^{+}$.

Transition	Expt. value	Calc. value	Diff.
(0,3) Band			
Q(1)	17664.468	17664.529	0.061
Q(2)	17652.963	17652.940	-0.023
Q(3)	17635.424	17635.517	0.093
Q(4)	17612.222	17612.218	-0.004
Q(5)	17582.987	17582.984	-0.003
Q(6)	17547.748	17547.743	-0.005
Q(7)	17506.387	17506.410	0.023
Q(8)	17458.885	17458.891	0.006
Q(9)	17405.097	17405.079	-0.018
Q(10)	17344.861	17344.861	0.000
Q(11)	17278.135	17278.115	-0.020
Q(12)	17204.746	17204.714	-0.032
Q(13)	17124.565	17124.528	-0.037
Q(14)	17037.437	17037.427	-0.010
Q(15)	16943.262	16943.279	0.017
Q(16)	16841.914	16841.958	0.044
Q(17)	16733.343	16733.343	0.000

Table B.2 Non-linear least squares fits results for the Q branch of the (0,3) band of the $^{1}\Pi$-$^{1}\Sigma^{+}$ transition of $^{74}GeH^{+}$.

Transition	Expt. value	Calc. value	Diff.
(0,3) Band			
R(1)	17677.841	17677.807	-0.034
R(2)	17672.836	17672.818	-0.018
R(3)	17661.979	17661.942	-0.037
R(4)	17645.076	17645.114	0.038
R(5)	17622.237	17622.254	0.017
R(6)	17593.297	17593.271	-0.026
R(7)	17558.075	17558.063	-0.012
R(8)	17516.494	17516.516	0.022
R(9)	17468.494	17468.509	0.015
R(10)	17413.912	17413.914	0.002
R(11)	17352.597	17352.596	-0.001
R(12)	17284.412	17284.418	0.006
R(13)	17209.250	17209.242	-0.008
R(14)	17126.919	17126.929	0.010
R(15)	17037.322	17037.347	0.025
R(16)	16940.409	16940.367	-0.042

Table B.3 Non-linear least squares fits results for the R branch of the (0,3) band of the $^{1}\Pi$-$^{1}\Sigma^{+}$ transition of $^{74}GeH^{+}$.

Transition	Expt. value	Calc. value	Diff.
(1,3) Band			
P(9)	17716.356	17716.339	-0.017
P(10)	17646.746	17646.782	0.036
P(11)	17570.455	17570.460	0.005
P(12)	17487.295	17487.288	-0.007
P(13)	17397.230	17397.199	-0.031
P(14)	17300.178	17300.148	-0.030
P(15)	17196.093	17196.120	0.027
Q(8)	17826.758	17826.729	-0.029
Q(9)	17769.122	17769.136	0.014
Q(10)	17704.643	17704.692	0.049
Q(11)	17633.260	17633.304	0.044
Q(12)	17554.875	17554.897	0.022
Q(13)	17469.415	17469.419	0.004
Q(14)	17376.847	17376.849	0.002
Q(15)	17277.226	17277.206	-0.020
R(9)	17828.460	17828.482	0.022
R(10)	17769.274	17769.273	-0.001
R(11)	17702.999	17702.980	-0.019
R(12)	17629.564	17629.544	-0.020
R(13)	17548.893	17548.935	0.042

Table B.4 Non-linear least squares fits results for the (1,3) band of the $^1\Pi$-$^1\Sigma^+$ transition of $^{74}GeH^+$.

Transition	Expt. value	Calc. value	Diff.
(2,3) Band			
P(3)	18338.072	18338.120	0.048
P(4)	18306.408	18306.348	-0.060
P(5)	18267.999	18267.960	-0.039
P(6)	18222.795	18222.808	0.013
P(7)	18170.693	18170.707	0.014
Q(2)	18375.292	18375.320	0.028
Q(3)	18355.913	18355.895	-0.018
Q(4)	18329.819	18329.815	-0.004
Q(5)	18296.877	18296.925	0.048
Q(6)	18256.994	18257.033	0.039
Q(7)	18209.949	18209.907	-0.042
R(1)	18400.165	18400.181	0.016
R(2)	18393.223	18393.184	-0.039
R(3)	18379.561	18379.518	-0.043
R(4)	18359.002	18359.025	0.023
R(5)	18331.487	18331.502	0.015

Table B.5 Non-linear least squares fits results for the (2,3) band of the $^1\Pi$-$^1\Sigma^+$ transition of $^{74}GeH^+$.

Transition	Expt. value	Calc. value	Diff.
(2,4) Band			
P(4)	16556.902	16556.946	0.044
P(6)	16477.423	16477.421	-0.002
Q(4)	16580.443	16580.413	-0.030
Q(5)	16549.321	16549.322	0.001
R(2)	16641.331	16641.338	0.007
R(3)	16628.722	16628.709	-0.013
R(4)	16609.629	16609.623	-0.006

Table B.6 Non-linear least squares fits results for the (2,4) band of the $^1\Pi$-$^1\Sigma^+$ transition of $^{74}GeH^+$.

Transition	Expt. value	Calc. value	Diff.
(0,3) Band			
P(4)	17583.611	17583.594	-0.017
P(5)	17547.959	17547.967	0.008
P(6)	17506.442	17506.447	0.005
P(7)	17458.959	17458.972	0.013
P(8)	17405.452	17405.464	0.012
P(9)	17345.798	17345.837	0.039
P(10)	17279.980	17279.991	0.011
P(16)	16747.947	16747.926	-0.021
P(17)	16635.263	16635.273	0.010
Q(4)	17609.863	17609.848	-0.015
Q(5)	17580.606	17580.590	-0.016
Q(6)	17545.327	17545.321	-0.006
Q(8)	17456.421	17456.406	-0.015
Q(9)	17402.569	17402.559	-0.010
Q(11)	17275.538	17275.513	-0.025
Q(12)	17202.096	17202.066	-0.030
Q(13)	17121.861	17121.831	-0.030
Q(14)	17034.653	17034.674	0.021
Q(15)	16940.498	16940.463	-0.035
Q(16)	16839.002	16839.069	0.067
Q(17)	16730.359	16730.367	0.008
R(6)	17590.865	17590.877	0.012
R(7)	17555.634	17555.642	0.008
R(8)	17514.043	17514.067	0.024
R(9)	17466.030	17466.028	-0.002
R(10)	17411.400	17411.398	-0.002
R(11)	17350.046	17350.041	-0.005
R(13)	17206.583	17206.595	0.012
R(14)	17124.215	17124.227	0.012
R(15)	17034.548	17034.577	0.029
R(16)	16937.576	16937.516	-0.060

Table B.7 Non-linear least squares fits results for the (0,3) band of the $^{1}\Pi$-$^{1}\Sigma^{+}$ transition of $^{70}GeH^{+}$.

Transition	Expt. value	Calc. value	Diff.
(1,3) Band			
P(9)	17713.967	17713.970	0.003
P(11)	17567.908	17567.921	0.013
P(12)	17484.712	17484.714	0.002
P(13)	17394.592	17394.599	0.007
P(15)	17193.366	17193.338	-0.028
Q(10)	17702.230	17702.208	-0.022
Q(11)	17630.789	17630.784	-0.005
Q(12)	17552.332	17552.351	0.019
Q(13)	17466.849	17466.821	-0.028
Q(14)	17374.094	17374.119	0.025
R(11)	17700.605	17700.602	-0.003
R(12)	17627.120	17627.132	0.012
R(13)	17546.408	17546.412	0.004
R(14)	17458.374	17458.375	0.001

Table B.8 Non-linear least squares fits results for the (1,3) band of the $^1\Pi$-$^1\Sigma^+$ transition of $^{70}GeH^+$.

Transition	Expt. value	Calc. value	Diff.
(2,3) Band			
P(4)	18304.463	18304.475	0.012
P(5)	18266.071	18266.052	-0.019
P(6)	18220.878	18220.877	-0.001
Q(3)	18354.021	18354.044	0.023
Q(4)	18327.944	18327.929	-0.015
Q(5)	18295.012	18295.013	0.001
Q(6)	18255.116	18255.115	-0.001
R(2)	18391.372	18391.372	0.000
R(3)	18377.718	18377.691	-0.027
R(4)	18357.191	18357.191	0.000
R(5)	18329.643	18329.685	0.042
R(6)	18294.964	18294.947	-0.017

Table B.9 Non-linear least squares fits results for the (2,3) band of the $^1\Pi$-$^1\Sigma^+$ transition of $^{70}GeH^+$.

Appendix C Calculated potentials for the $X^1\Sigma^+$ and $A^1\Pi$ states.

R(Å)	E(cm^{-1})	R(Å)	E(cm^{-1})
1.4331345	1980.776499	1.4520716	1914.576499
1.4738876	1837.926499	1.4985355	1750.826499
1.5259630	1653.276499	1.5561128	1545.276499
1.5889229	1426.826499	1.6243270	1297.926499
1.6622552	1158.576499	1.7027885	1008.776499
1.7470872	848.526499	1.7971271	677.826499
1.8563814	496.676499	1.9324218	305.076499
2.2342686	0.000000	2.6448062	305.076499
2.7980630	496.676499	2.9384752	677.826499
3.0741107	848.526499	3.2090402	1008.776499
3.3459684	1158.576499	3.4872243	1297.926499
3.6357532	1426.826499	3.7946072	1545.276499
3.9671129	1653.276499	4.1572077	1750.826499
4.3698869	1837.926499	4.6118964	1914.576499
4.8929368	1980.776499	5.2279791	2036.526499

Table C.1 Calculated $^1\Pi$ potential for $^{70}GeH^+$

R(Å)	E(cm^{-1})	R(Å)	E(cm^{-1})
1.3858502	2181.870922	1.3969752	2143.035076
1.4121682	2089.747714	1.4313626	2022.008836
1.4544758	1939.818442	1.4814101	1843.176532
1.5120536	1732.083106	1.5462826	1606.538164
1.5839622	1466.541706	1.6249486	1312.093732
1.6690905	1143.194242	1.7172143	959.843236
1.7717390	762.040714	1.8369558	549.786676
1.9226183	323.081122	2.2334283	0.000000
2.6618510	323.081122	2.8418902	549.786676
3.0071620	762.040714	3.1682691	959.843236
3.3305602	1143.194242	3.4977959	1312.093732
3.6741060	1466.541706	3.8644064	1606.538164
4.0741288	1732.083106	4.3099707	1843.176532

Table C.2 Calculated $^1\Pi$ potential for $^{74}GeH^+$

R(Å)	E(cm^{-1})	R(Å)	E(cm^{-1})
1.2879883	7532.751723	1.2945300	7093.082973
1.3014380	6649.276723	1.3087539	6201.332973
1.3165272	5749.251723	1.3248184	5293.032973
1.3337022	4832.676723	1.3432729	4368.182973
1.3536520	3899.551723	1.3650010	3426.782973
1.3775424	2949.876723	1.3915972	2468.832973
1.4076597	1983.651723	1.4265639	1494.332973
1.4499408	1000.876723	1.5677751	0.000000
1.7114735	1000.876723	1.7479105	1494.332973
1.7799757	1983.651723	1.8093016	2468.832973
1.8367241	2949.876723	1.8627393	3426.782973
1.8876699	3899.551723	1.9117404	4368.182973
1.9351142	4832.676723	1.9579148	5293.032973
1.9802385	5749.251723	2.0021622	6201.332973
2.0237483	6649.276723	2.0450488	7093.082973
2.0661074	7532.751723		

Table C.3 Calculated $^1\Sigma^+$ potential for $^{70}GeH^+$

R(Å)	E(cm^{-1})	R(Å)	E(cm^{-1})
1.2880053	7532.747650	1.2945461	7093.078900
1.3014530	6649.272650	1.3087676	6201.328900
1.3165394	5749.247650	1.3248290	5293.028900
1.3337109	4832.672650	1.3432793	4368.178900
1.3536559	3899.547650	1.3650020	3426.778900
1.3775400	2949.872650	1.3915908	2468.828900
1.4076485	1983.647650	1.4265469	1494.328900
1.4499162	1000.872650	1.5677078	0.000000
1.7113479	1000.872650	1.7477696	1494.328900
1.7798211	1983.647650	1.8091344	2468.828900
1.8365450	2949.872650	1.8625487	3426.778900
1.8874684	3899.547650	1.9115282	4368.178900
1.9348915	4832.672650	1.9576819	5293.028900
1.9799956	5749.247650	2.0019092	6201.328900
2.0234856	6649.272650	2.0447764	7093.078900
2.0658253	7532.747650		

Table C.4 Calculated $^1\Sigma^+$ potential for $^{74}GeH^+$

Appendix D Unassigned line positions

$^{74}GeH^+$ Line	Int.	FWHM	$^{70}GeH^+$ Line	Int.	FWHM
16506.984	1082	0.016			
16558.011	703	0.052			
16600.706	691	0.003			
16600.715	855	0.003			
16617.671	215	0.334			
16627.979	541	0.004			
16628.509	502	0.020			
16635.708	1173	0.003			
16635.728	1106	0.003			
16638.477	927	0.019	16636.045	281	0.010
16642.896	1234	0.020			
16644.896	514	0.010			
16774.710	260	0.240			
16782.198	1200	0.005	16779.515	690	0.009
16845.135	460	0.048			
16847.105	550	0.009			
16914.002	1202	0.006			
16914.011	1376	0.006	16912.087	918	0.020
16914.472	360	0.326			
17116.740	347	0.722			
17121.140	419	0.033			
17125.068	374	0.014	17123.143	250	0.005
17176.769	656	0.019			
17190.725	927	0.007	17187.930	545	0.006
17228.829	931	0.006	17226.022	534	0.008
17233.588	316	0.615			
17257.093	758	0.015			
17306.913	351	0.134			
17314.421	380	0.356	17312.205	663	0.840
17323.169	1125	0.008	17321.002	697	0.004
17338.127	263	0.386			

Table D.1 Unassigned transitions in GeH^+(vacuum cm^{-1}except Int. [arb units])

$^{74}GeH^+$ Line	Int.	FWHM	$^{70}GeH^+$ Line	Int.	FWHM
17414.830	387	0.414			
17426.158	434	0.704			
17453.342	2663	0.013	17451.516	3000	0.020
17473.937	745	0.028	17472.172	268	0.030
17523.878	300	0.347			
17538.376	314	0.061			
17540.506	1133	0.230			
17552.472	2575	0.068	17550.444	1414	0.069
17554.732	680	0.004	17552.364	834	0.020
17556.141	1273	0.011	17554.565	406	0.009
17577.627	6000	0.005	17576.009	3453	0.005
17577.637	6000	0.003	17576.019	3429	0.003
17595.044	1536	0.045	17593.166	298	0.036
17669.718	1025	0.008	17668.131	1528	0.014
17669.740	2842	0.005			
17669.740	3078	0.005			
17677.812	155	0.285			
17689.585	2315	0.009			
17689.595	2092	0.003	17688.127	1760	0.017
17704.748	1478	0.120	17702.823	873	0.016
17819.700	472	0.003			
Dye Gap	-	-	-	-	-
18098.198	225	0.210			
18117.991	195	0.276			
18118.008	170	0.011			
18155.835	200	0.600			
18171.027	175	0.010			
18182.025	225	0.300			
18222.808	900	0.020	18220.903	170	0.007
18245.408	676	2.610			
18264.754	142	0.121			
			18266.063	838	0.004
			18266.083	223	0.005

Table D.2 Unassigned transitions in GeH^+(vacuum cm^{-1}except Int. [arb units])

$^{74}GeH^+$ line	Int.	FWHM	$^{70}GeH^+$ line	Int.	FWHM
18275.701	1600	0.014	18273.124	1873	0.013
18282.639	400	0.170			
18300.481	5841	0.022	18298.963	4401	0.026
			18304.440	417	0.027
18314.808	1312	0.035	18312.755	832	0.059
18317.577	168	1.300			
18321.317	106	0.486			
18326.236	244	0.563			
18371.797	130	0.630			
18374.697	297	0.132			
			18377.718	480	0.005
18398.172	248	0.480			
18401.844	1576	0.023	18399.358	1266	0.029
18404.370	735	0.013			
18404.380	2499	0.003	18403.232	2967	0.003
18404.390	2824	0.003	18403.238	2453	0.003
18404.810	544	0.262			
18416.688	953	0.058	18415.294	434	0.046
18439.383	3249	0.010	18437.940	2140	0.006
18439.404	5231	0.004	18437.952	2335	0.006
18443.753	2046	0.009	18442.638	488	0.005
18455.233	424	0.001			
18455.239	414	0.006	18453.940	312	0.014
18455.395	263	0.002	18454.028	392	0.027
18462.978	2548	0.003	18461.296	606	0.003
18462.984	2890	0.004	18461.302	763	0.007
18493.171	400	0.003			
18493.175	352	0.003			
18496.858	2014	0.007	18494.448	2241	0.014
18520.511	180	0.057			
18534.618	204	0.001			
18534.637	559	0.002			
18534.649	736	0.003			
18546.445	224	0.013			
18546.463	852	0.003			
18546.469	1224	0.009			

Table D.3 Unassigned transitions in GeH^+(vacuum cm^{-1}except Int. [arb units])

Bibliography

[1] J.P. Maier. *Chemistry in Britain*, pages 437–440, May 1992.

[2] G. Herzberg. *Rev. Chem. Soc.*, 25:201–222, 1971.

[3] R.J. Saykally and R.C. Woods. *Ann. Rev. Chem.*, 32:403–431, 1981.

[4] J.T. Moseley. *Photodissociation and Photoionization*, chapter Ion Photofragment Spectroscopy, pages 245–298. J. Wiley and Sons Ltd., 1985.

[5] J.P. Maier. *J. Electron Spectrosc. Relat. Phenom.*, 66:15–24, 1993.

[6] I. Dabrowski and G. Herzberg. *J. Mol. Spec.*, 78:183–214, 1978.

[7] A. Carrington and D.A. Ramsay. *Physica Scripta*, 25:272–274, 1982.

[8] M. Tsuji, M. Tanaka, and Y. Nishimura. *J. Chem. Phys.*, 107(13):4852–4863, 1997.

[9] M. Tsuji, M. Matsuo, and Y. Nishimura. *International Journal of Mass Spectrometry and Ion Physics*, 34:273–286, 1980.

[10] C-Y. Kung, T.A. Miller, and R.A. Kennedy. *Phil. Trans. R. Soc. Lond.*, A324:223–232, 1988.

[11] J. Xie and R.N. Zare. *Chem. Phys. Lett*, 159(5,6):399–405, 1989.

[12] K. Boudjarane, M. Carre, and M. Larzillière. *Chem. Phys. Lett.*, 243:571–578, 1995.

[13] K. Boudjarane, J. Lacoursière, and M. Larzillière. *J. Chem. Phys.*, 101(12):10274–10282, 1994.

[14] R. Cameron, T.J. Scholl, L. Zhang, R.A. Hold, and S.D. Rosner. *J. Mol. Spec.*, 169:352–363, 1995.

[15] R.A. Holt, T.J.Scholl, and S.D. Rosner. *Can. J. Phys.*, 75:721–732, 1997.

[16] F.G. Celii and J.P. Maier. *J. Opt. Soc. Am. B*, 7(9):1944–1949, 1990.

[17] F.G. Celii, J.P. Maier, and M. Ochsner. *J. Chem. Phys.*, 85(10):6230–6231, 1986.

[18] C.S. Gudeman, M.H. Begemann, J. Pfaff, and R.J. Saykally. *Phys. Rev. Lett*, 50:727–731, 1983.

[19] P.B. Davies and P.M. Martineau. *J. Chem. Phys.*, pages 485–486, 1988.

[20] K. Harada, T. Wada, and T. Tanaka. *J. Mol. Spec.*, 163:436–442, 1994.

[21] D. Collet, J.-L. Destombes, I.H. Bachir, and T.R. Huet. *Chem. Phys. Lett.*, 286:311–316, 1998.

[22] Z. Liu and P.B. Davies. *Phys. Rev. Lett.*, 79(15):2779–2782, 1997.

[23] S.C. Foster, A.R. McKellar, and T.J. Sears. *J. Chem. Phys.*, 81(1):578–579, 1984.

[24] T. Ruchti, T. Speck, J.P. Connelly, E.J. Bieske, H. Linnartz, and J.P. Maier. *J. Chem. Phys.*, 105(7):2591–2593, 1996.

[25] K. Kawaguchi, C. Yamada, S. Saito, and E. Hirota. *J. Chem. Phys.*, 82(4):1750–1755, 1985.

[26] T.A. Dixon and R.C. Woods. *Phys. Rev. Lett.*, 34:61–63, 1975.

[27] Y. Ohshima and Y. Endo. *Chem. Phys. Lett.*, 256:635–640, 1996.

[28] R.J. Saykally and K.M. Evenson. *Phys. Rev. Lett.*, 43(7):515–518, 1979.

[29] T.D. Varberg and K.M. Evenson. *J. Chem. Phys.*, 100(4):2487–2491, 1994.

[30] R.J. Saykally. *Chemistry in Britain*, February:159–161, 1985.

[31] C. Focsa, B. Pinchemel, D. Collet, and T.R. Huet. *J. Mol. Spec.*, 189:254–263, 1998.

[32] A.O. Keefe and D. Deacon. *Rev. Sci. Instrum.*, 59:2544–2551, 1988.

[33] M. Kotterer, J. Conceicao, and J.P. Maier. *Chem. Phys. Lett.*, 259:233–236, 1996.

[34] F. von Busch and G.H. Dunn. *Phys. Rev. A*, 5(4):1726–1743, 1972.

[35] J.B. Ozenne, D. Pham, and J. Durup. *Chem. Phys. Lett.*, 17:422–424, 1972.

[36] N.P.F.B. van. Asselt, J.G. Maas, and J. Los. *Chem. Phys. Lett*, 24:555–558, 1974.

[37] W.J. Wing, G.A. Ruff, W.E. Lamb, and J.J. Spezeski. *Phys. Rev. Lett*, 25:1488–1491, 1976.

[38] J.T. Moseley, M. Tadjeddine, J. Durup, J.-B. Ozenne, C. Pernot, and A. Tabché-Fouhailleé. *Phys. Rev. Lett.*, 37(14):891–895, 1976.

[39] A. Carrington, P.G. Roberts, and P.J. Sarre. *Mol. Phys.*, 6:1523–1535, 1978.

[40] M. Tadjeddine, R. Abouaf, P.C. Cosby, B.A. Huber, and J.T. Moseley. *J. Chem. Phys*, 69(2):710–719, 1978.

[41] J. Moseley and J. Durup. *Ann. Rev. Phys. Chem.*, 32:53–76, 1981.

[42] J Moseley and J. Durup. *Journal de chimie physique*, 77(7/8):673–688, 1980.

[43] A. Carrington, J. Buttenshaw, R.A. Kennedy, and T.P. Softley. *Mol. Phys.*, 45(3):747–752, 1982.

[44] A. Carrington and T.P. Softley. *Chem. Phys.*, 106:315–338, 1986.

[45] A. Carrington, R.A. Kennedy, T.P. Softley, P.G. Fournier, and E.G. Richard. *Chem. Phys.*, 81(3):251–261, 1983.

[46] A. Carrington, I.R. McNab, and A. Montgomerie. *Chem. Phys. Lett.*, 149(3):326–329, 1988.

[47] A. Carrington, I.R. McNab, and C.A. Montgomerie. *Mol. Phys.*, 65(3):751–755, 1988.

[48] H. Helm, P.C. Cosby, M.M. Graff, and J.T. Moseley. *Phys. Rev. A*, 25(1):304–321, 1982.

[49] P.J. Sarre, J.M. Walmsley, and C.J. Whitham. *J. Chem. Soc. Farad. Trans. 2*, 82:1243–1255, 1986.

[50] P.J. Sarre and C.J. Whitham. *Mol. Phys.*, 62(6):1505–1508, 1987.

[51] M.M. Graff, J.T. Moseley, and E. Roueff. *The Astrophysical Journal*, 269:796–802, 1983.

[52] P.J. Sarre, J.M. Walmsley, and C.J. Whitham. *Phil. Trans. R. Soc. Lond. A*, 324:233–246, 1988.

[53] A. Carrington and T. Softley. *Chem. Phys.*, 92:199–219, 1985.

[54] C.P. Edwards, P.J. Sarre, and D.J. Milton. *Mol. Phys.*, 58(1):53–63, 1986.

[55] C.P. Edwards, C.S. Maclean, and P.J. Sarre. *Mol. Phys.*, 52:1453–1466, 1984.

[56] C.P. Edwards, C.S. Maclean, and P.J. Sarre. *J. Chem. Phys.*, 76(7):3829–3831, 1982.

[57] D.J. Rodgers and P.J. Sarre. *Chem. Phys. Lett.*, 143(3):235–239, 1988.

[58] A.P. Levick, T.E. Masters, D.J. Rodgers, P.J. Sarre, and Q.-S. Zhu. *Phys. Rev. Lett.*, 63(20):2216–2219, 1989.

[59] P.C. Cosby and H. Helm. *J. Chem. Phys.*, 75(8):3882–3893, 1981.

[60] T.E. Masters and P.J. Sarre. *J. Chem. Soc. Faraday Trans.*, 86(11):2005–2008, 1990.

[61] P.C. Cosby and H. Helm. *J. Chem. Phys.*, 94(1):92–104, 1991.

[62] U. Hechtfischer, Z. Amitay, P. Forck, M. Lange, J. Linkemann, M. Schmitt, U. Schramm, D. Schwalm, R. Wester, D. Zajfman, and A. Wolf. *Phys. Rev. Lett.*, 80(13):2809–2812, 1998.

[63] U. Hechtfischer. Personal communication.

[64] D. Zajfman, O. Heber, L. Vejby-Christensen, I. Ben-Ttzhak, M. Rappaport, R. Fishman, and M. Dahan. *Phys. Rev. A*, 55(3):R1577–R1580, 1997.

[65] M. Dahan, R. Fishman, O. Heber, M. Rappaport, N. Altstein, D. Zajfman, and W.J. van der Zande. *Rev. Sci. Instrum*, 69(1):76–83, 1998.

[66] H. Léfèbvre-Brion and R.W. Field. *Pertubations in the Spectra of Diatomic Molecules*. Academic Press, 1986.

[67] *Coherent Service Manual 699-29*, 00 8/80 edition.

[68] Cw dye laser fact sheet. Technical report, Coherent Laser Division, 1983.

[69] R.G. Cooks, J.H. Beynon, R.M. Caprioli, and G.R. Lester. chapter Metastable ions. Elsevier, Amsterdam, 1973.

[70] L. Veseth. *J. Phys. B: Atom. Molec. Phys.*, 6:1473–1483, 1973.

[71] L. Veseth. *J. Phys. B: Atom. Molec. Phys.*, 6:1484–1496, 1973.

[72] J.M. Brown, J.T. Hougen, K.-P. Huber, J.W.C. Johns, I. Kopp, H. Lefebvre-Brion, A.J. Merer, D.A. Ramsay, J. Rostas, and R.N. Zare. *J. Mol. Spec.*, 55:500–503, 1975.

[73] J.T. Moseley. *J. Phys. Chem.*, 86:3282–3288, 1982.

[74] G. Herzberg. *Spectra of Diatomic Molecules*. Van Nostrand Reinhold Ltd., 1950.

[75] G-B. Kim and K. Balasubramanian. *J. Mol. Spec.*, 134:412–420, 1989.

[76] M. Kronekvist, A. Lagerqvist, and H. Neuhaus. *J. Mol. Spec.*, 39:516–518, 1971.

[77] R.J. LeRoy and R.B. Bernstein. *J. Chem. Phys.*, 54(12):5114–5126, 1971.

[78] T. Uzer and A. Dalgarno. *Chem. Phys. Lett.*, 63(1):22–24, 1979.

[79] M.M. Graff and J.T. Moseley. *Chem. Phys. Lett.*, 83(1):97–100, 1981.

[80] *University of Waterloo Chemical Physics Research Report CP-425*, 1992.

[81] R.N. Zare and J.K. Cashion. Ucrl-10881. Technical report, University of California Lawrence Radiation Laboratory, 1963.

[82] R.J. LeRoy and W-K. Liu. *J. Chem. Phys.*, 69(8):3622–3631, 1978.

[83] M. Tsuji, S. Shimada, and Y. Nishimura. *Chem. Phys. Lett.*, 89(1):75–78, 1982.

[84] S. Yamaguchi, M. Tsuji, H. Obase, H. Sekiya, and Y. Nishimura. *J. Chem. Phys*, 86(9):4952–4956, 1987.

[85] J.M. Hollas. *High Resolution Spectroscopy*. Butterworths, 1982.

[86] M. Tsuji, S. Shimada, and Y. Nishimura. *J. Mol. Spec.*, 103:501–502, 1984.

[87] S. Yamaguchi, M. Tsuji, and Y. Nishimura. *Can. J. Phys.*, 64:1374–1378, 1986.

[88] R.C. Binning Jr and L.A. Curtis. *J. Chem. Phys.*, 92(6):3688–3692, 1990.

[89] K.D. Kalyan and K. Balasubramanian. *J. Mol. Spec.*, 143:195–202, 1990.

[90] *University of Waterloo Chemical Physics Research Report CP-555*, 1995.

[91] P.F. Bernath. *Spectra of Atoms and Molecules*. OUP, 1995.

[92] Y. Nishimura. Personal Communication.

[93] A. Carrington and D.A. Ramsay. *Physica Scripta*, 25:272–274, 1982.

[94] A.E. Douglas and B.L. Lutz. *Can. J. Phys.*, 48:247–253, 1970.

[95] C.J. Whitham. *Laser Photofragment Spectroscopy of CH^+ and SiH_2^+*. PhD thesis, The University of Nottingham, 1987.

[96] C. Williams and K.F. Freed. *J. Chem. Phys.*, 85(5):2699–2717, 1986.

[97] P.J. Sarre, C.J. Whitham, and M.M. Graff. *J. Chem. Phys.*, 90(11):6061–6069, 1989.

[98] M.S. Child. *Molecular Physics*, 32(6):1495–1510, 1976.

[99] M.S. Child and R. Lefebvre. *Chem. Phys. Lett.*, 55(2):213–216, 1978.

[100] J.M. Walmsley. *High Resolution Laser Photofragment Spectroscopy of Diatomic Molecular Ions*. PhD thesis, The University of Nottingham, 1988.

[101] P.J. Sarre. Personal Communication.

[102] B.A. Huber, T.M. Miller, P.C. Cosby, H.D. Zeman, and J.T. Moseleyand J.R. Peterson. *Rev. Sci. Instrum.*, 48:1306–1313, 1977.

[103] Ivan Powis. Personal Communication, 1998.

[104] *Numerical Recipes in Fortran: The Art of Scientific Computing*. Cambridge University Press, 2nd edition.

[105] C.E. Moore. *Ionisation Potentials and Ionisation Limits Derived from the Analysis of Optical Spectra: Natl. Stand. Ref. Data Ser., Natl. Bur. Stand. (U.S.) Circ. No. 34*. U.S. GPO Washington D.C., 1967.

[106] M. Lyyra J. Brzozowski, P. Erman. *Physica Scripta*, 4:507–511, 1978.

[107] J. Czarny, P. Felenbok, and H. Levebrvre-Brion. *J. Phys. B: Atom. Molec. Phys.*, 4:124–132, 1971.

[108] J. Mauricio, O. Matos, Per-Åke Malmqvist, and Björn O. Roos. *J. Chem. Phys.*, 85(9):5032–5042, 1987.

[109] A.B. Sannigrahi, R.J. Buenker, G. Hirsch, and J. Gu. *Chem. Phys. Lett.*, 237:204–211, 1995.

[110] G. Scoles, editor. *Atomic and Molecular Beam Methods Vol I.* OUP, 1988.

[111] G. Scoles, editor. *Atomic and Molecular Beam Methods Vol II.* OUP, 1992.

[112] E.J. Bieske and J.P. Maier. *Chem. Rev.*, 93:2603–2621, 1993.

[113] P. Erman, O. Gustafsson, and M. Larsson. *Physica Scripta*, 27:192–200, 1983.

[114] P. Erman. *Physica Scripta*, 11:65–78, 1975.

[115] A. Carrington, A.M. Shaw, and S.M. Taylor. *Chem. Phys. Lett.*, 241:611–617, 1995.

[116] Y.K. Bae, P.C. Cosby, M. Nicholson, and W. Olson. *Rev. Sci. Instrum.*, 62(5):1157–1162, 1991.

[117] J.V. Coe, J.C. Owrutsky, E.R. Keim, E.V. Agman, D.C. Hovde, and R.J. Saykally. *J. Chem. Phys.*, 90:3893–3902, 1989.

[118] E.J. Bieske, A. Soliva, M.A. Welker, and J.P. Maier. *J. Chem. Phys.*, 93(6):4477–4479, 1990.

[119] J.P. Maier E.J. Bieske, A. Soliva. *J. Chem. Phys.*, 94:4749–4755, 1991.

[120] E.J. Bieske, A.M. Soliva, A. Friedmann, and J.P. Maier. *J. Chem. Phys.*, 100(6):4156–4164, 1994.

[121] E.J. Bieske, A.M. Soliva, A. Friedmann, and J.P. Maier. *J. Chem. Phys*, 96(1):28–34, 1992.

[122] E.J. Bieske, S.A. Nizkorodov, F.R. Bennett, and J.P. Maier. *International Journal of Mass Spectrometry and Ion Processes*, 149/150:167–177, 1995.

[123] J.C. Hansen, M.M. Graff, J.T. Moseley, and P.C.Cosby. *J. Chem. Phys.*, 74(4):2195–2200, 1981.

[124] J.C. Hansen, J.T. Moseley, A.L. Roche, and P.C. Cosby. *J. Chem. Phys.*, 77(3):1206–1213, 1982.

[125] P.C. Cosby, J.-B. Ozenne, J.T. Moseley, and D.L. Albritton. *J. Mol. Spec.*, 79:203–235, 1980.

[126] J.C. Hansen, J.T. Moseley, and P.C. Cosby. *J. Mol. Spec.*, 98:48–63, 1983.

[127] J.T. Moseley, P.C. Cosby, J.-B. Ozenne, and J. Durup. *J. Chem. Phys.*, 70(3):1474–1481, 1979.

[128] A.S. Ashman, L.J. Fransinski, and M.H. Tinker. *International Journal of Mass Spectrometry and Ion Processes*, 116:37–51, 1992.

[129] A. Carrington, I.R. McNab, and C.A. Montgomerie. *J. Phys. B. At. Mol. Opt. Phys.*, 22:3551–3586, 1989.

[130] P.J. Sarre. Personal Communication.

[131] G. Scoles, editor. *Atomic and Molecular Beam Methods*, chapter Free Jet Sources. OUP, 1988.